Narrow-Linewidth Phase Locking of Diode Lasers for Raman Transitions and Set-up of Sum-Frequency Generation Beamlines

Master Thesis

Tom Schatteburg, D-CHAB, *stom@student.ethz.ch*

Supervisors:
Tobias Sägesser
Dr. Daniel Kienzler

Group leader:
Prof. Dr. Jonathan P. Home
TIQI group
ETH Zürich

Zürich, September 2019

Abstract

Quantum information processing in arrays of micro-fabricated Penning traps appears to be a promising alternative to the more commonly used Paul traps. In this thesis, part of the experimental work on the laser setup for this future experiment is described. First, the narrow-linewidth stabilization of two Raman lasers with respect to each other in an optical phase-locked loop was modeled, implemented and optimized. The maximum achieved loop bandwidths were found to be about 2.1 MHz with fiber-optical connections, and up to 2.7 MHz with a free space setup used to test the influence of signal propagation delay. The HWHM of the beat note between both locked lasers was around 9 Hz, indicating high phase stability. As second part of this thesis, two sum-frequency generation stages between 1050 nm and 1550 nm were set up and optimized. The measured efficiencies agree well with previously achieved results. Finally, the beat note between frequency-converted light from the locked lasers was observed at 626 nm, showing the effect of the sum-frequency generation stages and a not optimized laboratory environment on phase-stability.

Acknowledgements

I would like to thank a great number of people for their support over the course of this master thesis. I thank

> Tobias Sägesser and Dr. Daniel Kienzler for being the best supervisors that I could have wished for. Tobias is a great labmate and his cheerful attitude made the time in the lab more enjoyable. His motivation and guidance lead to a better work and thesis. His support had a major impact on this whole work and more. For this I am wholeheartedly grateful. Daniel supervised my master project from the beginning and without him, I would have made an uncountable number of mistakes. His experience prevented me from making excessively many, most of which I probably do not know about. It was invaluable to be able to always come to his office, interrupt him and ask for explanations and advice. For being so patient, even in some of our long discussions, I am also very thankful.
>
> Prof. Dr. Jonathan Home for giving me the opportunity to work in such a friendly and thriving research group. In addition, his knowledge of every topic that was brought up in discussions was always very helpful. Finally, it was a wonderful experience to attend a family-like conference, and I am thankful that I was welcome.
>
> The whole TIQI group for creating a supportive and pleasant working environment. In particular,
>
> Robin Oswald for explaining control theory to me, showing me how to model an OPLL and proof-reading the respective chapters of my thesis.
>
> Matteo Marinelli for tips and advice concerning all kinds of optics-related questions.
>
> Chi Zhang for going through my thesis talk on a Friday evening.
>
> Dr. Christopher Axline for explanations on how to use an electrical spectrum analyzer, and for being an excellent driver.
>
> Shreyans Jain for explaining to me some details of Penning traps and for feedback on the introduction.
>
> Finally, I thank Lisa and my family for supporting me unconditionally.

Contents

Chapter 1

Introduction

Quantum computation promises a significant speedup for tasks such as integer factorization [1], search algorithms [2] and quantum simulation [3, 4], possibly impacting the fields of cryptography, chemistry and nanotechnology. Arguably the two most prominent platforms for implementation of quantum computation are superconducting circuits [5] and trapped ions [6]. In trapped ions, a quasi two-level system in the ion's internal states is used as qubit, which is coupled via a coherent laser field to the ion's motion, acting as harmonic oscillator. Information can then be exchanged between multiple ions via their mutual Coulomb interaction [6, 7]. This allows the implementation of a universal gate set required for quantum computation with high fidelities [8, 9]. Imperfect operations however reveal the need for error correcting schemes, such as Shor's 9-qubit code [10] or surface codes [11], which require an increased number of qubits. Quantum simulation with a chain of over 50 ions [12], as well as stabilization of qubit states with repeated readout and feedback [13] has been demonstrated. As an alternative to quantum error correction with multiple physical qubits, a logical qubit can also be encoded in the continuous variables of an harmonic oscillator, such as the ion's motion [14, 15]. Still, the main challenge in trapped-ion quantum computation is its scalability, together with being able to address single ions individually [16].

To trap ions, Earnshaw's theorem [17] has to be taken into account, which states that a charged particle cannot be held in stable equilibrium by only static electric fields. In the commonly employed Paul traps [18], additional oscillating electric fields create a harmonic pseudopotential which confines the ion. However, if the average ion position does not exactly coincide with the minimum of this pseudopotential, these radio frequency (RF) fields also cause the ion to move at their exact frequency, which is called micromotion. This poses experimental difficulties like second-order Doppler shifts and changing spectral line shapes [19]. Also due to this single optimal ion position along the radial direction, scaling up the number of qubits is in practice limited to linear chains of ions, except if traps with segmented electrodes are used. Then, shuttling of ions between different zones on a surface trap chip [20] would facilitate targeted interactions between only pairs of ions [21]. Another issue with trapped ions for quantum computing is the so-called anomalous heating rate, which so far lacks a detailed explanation [22, 23].

Penning traps are an alternative to Paul traps, where a strong magnetic field instead of RF fields provides radial confinement [24]. With this, a quantum simulator with more than 200 ions has been demonstrated [25], but there, the ions form a crystal with fixed lattice type which also rotates continuously. The idea of the experiment, to which the work described in this thesis contributes, is to create arrays of microscopic Penning traps [26]. This is achieved by arranging the electrodes in such way that they generate static electric quadrupoles in a plane above the trap surface. Together with the Lorentz forces due to the magnetic field, this provides stable ion confinement. One application of this layout is to perform quantum simulations of spin-spin interactions in variable lattices. The Penning trap approach may have several advantages over using a Paul trap architecture, the first being higher ion densities for similar trapping parameters [27]. Due to the lack of RF fields, ions in Penning traps also do not exhibit micromotion, which is a source of the aforementioned experimental difficulties in Paul traps [19]. The presence of only static electric fields may also allow to gain some insight into the physical mechanism behind anomalous heating, by conducting heating rate measurements at varying distance of the ion to the trap surface without the need for a specialised trap geometry [23].

To achieve higher trap frequencies, the initial plan is to trap $^{9}Be^{+}$ instead of $^{4}0Ca^{+}$ ions. All of its relevant atomic transitions are around 313 nm, so 4 different colors at this wavelength are needed for stimulated Raman transitions, repumping and cooling/detection. Due to the demand for high power in the Raman beams, the UV light is generated via sum-frequency generation of 1050 nm and 1550 nm light, followed by cavity-enhanced second-harmonic generation of the resulting 626 nm light [28, 29]. Since the Zeeman splitting of the qubit states due to the strong magnetic field of the Penning trap is too large to be bridged by acousto-optic modulators [30], a different scheme to derive two phase-stable Raman beams has to be devised. One possibility for this is to use two separate laser sources and stabilize their phases with respect to each other. In the first part of this thesis, phase-stabilization of the two seed lasers for the Raman beamlines was implemented in a heterodyne optical phase-locked loop [31]. In the second part of this thesis, two of the sum-frequency generation beamlines were set up and optimized, and one of them was characterized.

This thesis is outlined as follows:

- **Chapter 2** introduces the Beryllium level structure and the corresponding laser setup. This also serves as more detailed motivation for the work performed in this thesis.
- **Chapter 3** introduces classical control theory as means to describe the optical phase-locked loop in an abstract way.
- **Chapter 4** then describes the phase-locking in detail, identifying its limitations and how to exhaust the system's possibilities. The experimental setup and its results are presented and possible adverse effects of the phase-locked loop in a trapped ion quantum information processing experiment are pointed out.
- **Chapter 5** describes the theory behind the sum-frequency generation beamlines, as well as the experimental work that has been performed and the results which were obtained.
- **Chapter 6** then concludes the thesis and provides an outlook over the immediate and further work.

Chapter 2

Background material

2.1 The Beryllium ion in a strong magnetic field

The ion that is planned to be used in this experiment is ^{9}Be$^+$. Due to its low mass, higher trap frequencies compared with other ion species can be achieved, which allows for easier sideband resolution, facilitating ion cooling. ^{9}Be$^+$ ions are produced from the neutral species by photo-ionization with a laser beam at 235 nm. The neutral Beryllium atoms are emitted from an atomic oven close to the trapping site, so that once they are ionized, the electromagnetic interactions with the trap electrodes and the strong magnetic field of the Penning trap allows them to be captured.

The level structure of ^{9}Be$^+$ in a magnetic field of $\sim$3 T as adapted from Biercuk *et al.* [32] is shown in figure 2.1. The levels of interest are in the manifolds of the ^{2}S$_{1/2}$ ground state and the ^{2}P$_{3/2}$ second excited state, which are separated by 313 nm. Since ^{9}Be has a nuclear spin of $I = 3/2$, the states are split into multiple hyperfine levels with different total angular momentum quantum numbers $F = I + J$. The hyperfine levels of the excited state are not drawn. The different hyperfine levels are further divided up into Zeeman sublevels due to the external magnetic field. For low magnetic fields, (F, m_F) are good quantum numbers. Then, the ground state hyperfine levels $F = 1$ and $F = 2$ give rise to 3 and 5 Zeeman sublevels, respectively, which is indicated by dashed lines. However since the planned magnetic field of $\sim$3 T is much higher than what is usually used in trapped-ion experiments with Paul traps [33], and (F, m_F) are only good quantum numbers for weak magnetic fields, the level structure is better described by (m_I, m_J). This means the hyperfine splitting is treated as perturbation to the Zeeman splitting, which together yields two sets of four Zeeman sublevels for the ground state, which are separated by $\sim$100 GHz. This is drawn schematically in figure 2.1. The qubit transition as indicated in red is between the $|\uparrow\rangle = |m_I = 3/2, m_J = 1/2\rangle$ and $|\downarrow\rangle = |m_I = 3/2, m_J = -1/2\rangle$ states, corresponding to an electron-spin-flip. This transition is advantageous to the nuclear-spin-flip transitions where $\Delta m_I = \pm 1$, since the electron flip couples much stronger to electric fields and thus its transition can be driven faster [32]. At magnetic fields of 4.5 T, the qubit transition frequency varies with 28 GHz/T [32], so also for $\sim$3 T, care has to be taken to minimize magnetic field fluctuations in order to increase qubit coherence times [33].

One could employ microwave fields to drive the qubit transition, however this would make it difficult to address single ions individually. Also, the long wavelength of microwave fields implies a low photon momentum, which makes it unfeasible to couple to the ion's motion. Instead, it is planned to use stimulated Raman transitions, indicated with green arrows, via a virtual sublevel in the ^{2}P$_{3/2}$ manifold. The position of this sublevel is determined by the detuning of the Raman

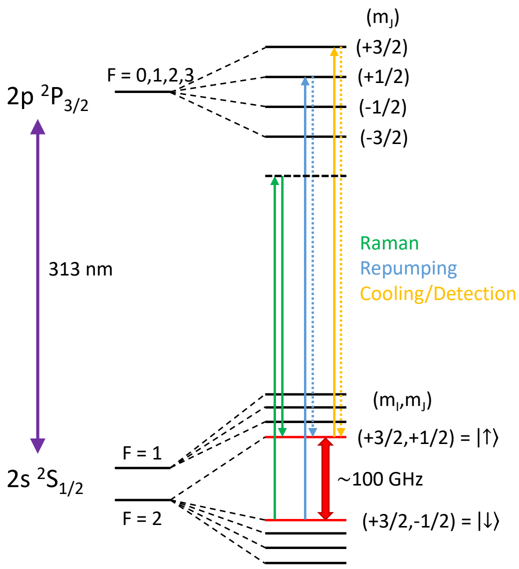

Figure 2.1: Level scheme of $^9\mathrm{Be}^+$ in a magnetic field of $\sim$3 T. The qubit transition is indicated in red.

beams. Here the virtual level is drawn with lower energy than the Zeeman sublevels, but in principle it can be located in between any one of them.

In order to initially turn a mixture between the qubit states into a pure state, a repumping beam from the lower qubit state $|\downarrow\rangle$ to the $m_J = 1/2$ manifold of the excited state is used. Since the excited state is short-lived, it will eventually decay into the upper qubit state $|\uparrow\rangle$, as indicated by a blue dashed arrow.

For Doppler cooling of the ion, and similar for detection of the qubit state, a closed cycling transition is needed. This is a transition where when the ion is excited, it can only decay into a single ground state level. Then, driving a laser on this transition leads to a constant cycle of absorption and spontaneous emission at this wavelength. The qubit state can be detected if one of the qubit levels is part of said closed cycling transition. Alternatively, deterministic pumping from one of the qubit states to the detection transition can also be employed. In our case, the closed cycling transition is between the states $|\uparrow\rangle = \left|{}^2\mathrm{S}_{1/2}, m_I = 3/2, m_J = 1/2\right\rangle$ and $\left|{}^2\mathrm{P}_{3/2}, m_I = 3/2, m_J = 3/2\right\rangle$, indicated by yellow arrows.

Together, four colors of laser light around 313 nm are needed: two Raman beams, the repumping beam and the beam for cooling and detection. Usually in trapped ion experiments with $^9\mathrm{Be}^+$, the two Raman beams are obtained from a single source, where the second beam is shifted in frequency using acousto-optic modulators (AOMs) [30]. However, the qubit splitting of $\sim$100 GHz in this experiment is too large to be feasibly bridged by AOMs, which is why separate sources have to be employed. The generation of these four beams is discussed in the following section.

2.2 Laser setup

As introduced in the previous section, four colors of laser light at 313 nm are necessary in order to perform quantum information processing experiments with $^9Be^+$. Especially, in order to avoid scattering photons during the Raman transitions, these beams should be far-detuned from any excited state. However, the effective Rabi frequency of stimulated Raman transitions scales with $\frac{g_1 g_2}{\Delta}$, where g_1 and g_2 are the coupling strengths of the initial and final levels to the virtual sublevel, which scale with electric field amplitude, and Δ is the detuning of the virtual sublevel to the next excited state. This means to still achieve a high effective Rabi frequency, the laser fields driving the Raman transition have to be strong, which shows the need for strong laser sources. Since there are no suitable laser sources at 313 nm, nonlinear optical processes have to be employed to generate light at this wavelength. One approach is to generate light at 626 nm and obtain 313 nm by second-harmonic generation (SHG). However, there are no high power laser sources at 626 nm. To obtain lower power, one can use a diode laser which would produce 635 nm light and cool it down such that its wavelength shifts to 626 nm. With this approach, 5-7 mW of UV light can be obtained with 130 mW at 626 nm [34]. Another possibility is to use the fact that 313 nm is the fifth harmonic of 1565 nm, which is in the infrared C-band, and accessible with Erbium-doped fiber amplifiers. With this approach, 100 mW of 313 nm light can be obtained with 15 W of 1565 nm input power [35].

The setup which is planned for this experiment is based on an even different approach: 313 nm is still obtained by SHG of 626 nm light, but instead of using a cooled diode laser, it is generated by sum-frequency generation of 1050 nm and 1550 nm light [28], which are both readily available by Ytterbium and Erbium-doped fiber amplifiers. This approach has also been implemented in the TIQI group before [29], showing the capability of generating several Watts of 313 nm power. A scheme of generating four colors of 313 nm light from five seed lasers at 1050 or 1550 nm is shown in figure 2.2. The 626 nm beams for repumping and cooling/detection will be frequency-locked to reference cavities using the Pound-Drever-Hall (PDH) locking scheme [36]. The need for the heterodyne optical-phase-locked loop (OPLL) between both Raman 1550 nm seed lasers is discussed in the following subsection. The red ellipses indicate the parts of the experiment which were set up for this thesis.

2.2.1 Phase stability requirement

As mentioned in section 2.1, the large qubit splitting of $\sim$100 GHz due to the strong magnetic field requires two separate laser sources for the Raman beams, different from the setups of Wilson *et al.* and Lo *et al.* [28, 29]. However, in order to drive stimulated Raman transitions coherently, both Raman beams have to be phase-stable with respect to each other, which is why for low-magnetic field experiments, it is advantageous to use a single source [30]. Different to transitions driven by only one laser beam where absolute frequency stability is required, both Raman beams only have to be stable with respect to each other. Absolute frequency fluctuations are negligible as long as they are much smaller than the detuning of the virtual sublevel, via which the transition is driven, from the next excited state [37]. Applying this to the scheme presented in figure 2.2 means that the frequency fluctuations of the 1050 nm seed laser for the Raman beamlines can be neglected, and only the two involved 1550 nm lasers have to be stabilized with respect to each other. This is implemented with a heterodyne OPLL, which will be explained in detail in chapter 4. Some extensions and alternatives to an OPLL are introduced in subsection 2.3.2.

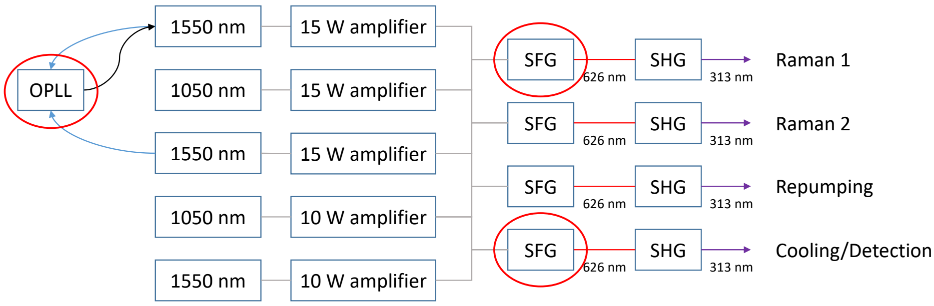

Figure 2.2: Overview scheme of the planned laser setup for the Penning experiment. Sum-frequency generation (SFG) of infrared photons at 1050 nm and 1550 nm creates red light at 626 nm, which is subsequently frequency-doubled in a cavity-enhanced second-harmonic generation (SHG) step to yield the desired 313 nm beams. The ∼100 GHz splitting of the qubit is not feasible to achieve with one laser source and acousto-optical modulators. Instead, we use two separate sources for the Raman beams, stabilized with respect to each other in an optical phase-locked loop (OPLL). Further necessary Pound-Drever-Hall (PDH) locking schemes are omitted for simplicity. The red ellipses indicate the work done for this thesis. The OPLL is described in detail in chapter 4, the two SFG stages in chapter 5.

2.3 Achieving phase stability of lasers at ∼100 GHz frequency splitting

To achieve frequency locking of both Raman lasers, different schemes can be employed, some of which are introduced in subsection 2.3.2. However, all of these require the laser frequencies to be much closer together than ∼100 GHz. As solution, sideband generation can be used to create stable spectral features which can act as reference for another laser to be locked to [38], possibly bridging the gap between both Raman frequencies. This sideband generation is explained first, followed by a short introduction to different frequency-locking schemes.

2.3.1 Sideband generation for phase-locking

Modulating the phase of an oscillating electrical field produces sidebands, which can be seen from the following identity:

$$\mathrm{e}^{i\omega t+i\beta\sin{(\Omega t)}} = J_0(\beta)\mathrm{e}^{i\omega t} + \sum_{k=1}^{\infty} J_k(\beta)\mathrm{e}^{i(\omega+k\Omega)t} + \sum_{k=1}^{\infty}(-1)^k J_k(\beta)\mathrm{e}^{i(\omega-k\Omega)t}, \tag{2.1}$$

which is a variant of the Jacobi-Anger expansion [39]. Here, ω would be the frequency of the laser field, β and Ω the phase modulation amplitude and frequency, and $J_k(\beta)$ the k-th Bessel function of the first kind. We see that phase modulation with the frequency Ω creates sidebands at frequencies $\omega \pm k\Omega$, whose amplitudes scale with $J_k(\beta)$. The zeroth, first and second order Bessel functions are plotted in figure 2.3, giving the normalized amplitude of the respective sidebands. By choosing β accordingly, the amplitudes of the first or second order sidebands can be maximized. For $\beta = 1.841$, the first sideband is maximal and contains about 34% of the total power. For $\beta = 3.054$, the second sideband is maximal and contains about 24% of the total power.

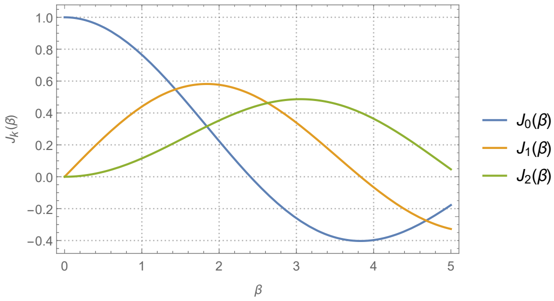

Figure 2.3: k-th order Bessel functions of the first kind $J_k(\beta)$ for $k = 0, 1, 2$. The function values give the amplitude of the k-th phase modulation sideband for modulation amplitude β.

Such phase modulation of a laser field can be achieved with electro-optical modulators (EOMs). Then, β is determined by the applied voltage, which is usually referenced with the voltage V_π for which $\beta = \pi$. State-of-the-art fiber optical EOMs at 1550 nm can modulate with frequencies of up to 40 GHz [40], so that a sideband which bridges the gap between both qubit frequencies should be possible to create. Note that due to the SHG step, the frequency between carrier and sideband is effectively doubled, so that at 1550 nm the difference between both Raman beams has to be $\sim$50 GHz. Depending on the exact magnetic field, the qubit transition frequency might be higher or lower, determining whether the first or second sideband has to be used.

2.3.2 Locking schemes

As mentioned before, an absolute frequency lock can be achieved with different schemes such as the PDH lock [36], which uses a stable cavity as reference. This could also be employed for the two 1550 nm seed lasers of the Raman beamlines, however since only relative frequency stability is needed, simpler schemes are also sufficient and might still yield higher performances. In these, light from one laser, called master laser, is used as a reference and the second laser, called slave laser, is controlled in such way that its frequency follows that of the master laser. In the following, several of such locking schemes, which achieve relative frequency stability, are briefly introduced. Some of them might have to be considered as alternatives in case the performance of the OPLL implemented for this thesis is not sufficient.

2.3.2.1 OPLL schemes

In a heterodyne optical phase-locked loop (OPLL) [31, 41], light from both lasers is overlapped on a photodiode, and its beat note in the RF regime is compared to a phase-stable reference signal. Applying feedback to the slave laser then controls its frequency such that the beat note is locked to the reference, and thus both lasers assume a stable frequency difference. Here, also the beat note created from a sideband of the master laser with the slave laser can be used to lock. Due to its relative simplicity in implementation, the heterodyne OPLL scheme was chosen to be set up as first option for the frequency stabilization of the two Raman seed lasers. This was done in the first part of this thesis, which is why chapters 3 and 4 are devoted to describing feedback loops in general, and the heterodyne OPLL specifically.

An extension to the OPLL scheme is the sub-carrier optical phase-locked loop technique (SC-OPLL) [41]. There, the feedback is applied to a component which generated sidebands also for the slave laser, which can allow for faster frequency tuning than in a normal OPLL.

For even higher performance, OPLL schemes with dual-loop configuration can be employed [42]. There, the beat note between master and slave laser is monitored on two photodiodes, so that an additional feedback path to an external phase-modulator also yields faster feedback than in a normal OPLL.

2.3.2.2 OIL schemes

One alternative to an OPLL is optical injection locking (OIL) [38, 43], in which light from the master laser is injected into the cavity of the slave laser. If both frequencies are close enough to each other, the slave laser oscillates at the frequency of the master laser and is thus locked to it. This requires an optical isolator which prevents light of the slave laser from entering the master laser. Also, there is then no frequency difference between both lasers, which is not what is needed for the two Raman beams in our setup. However, this can be overcome by modulating part of the output from the master laser like described in subsection 2.3.1, to obtain a comb of frequencies with spacing controlled by a phase-stable RF source. Then filtering the output light to select only one of these sidebands allows to achieve frequency differences between master and slave laser of $\sim$100 GHz [38].

A downside to OIL is that the master laser can drift away from the locking range of the slave laser, for example due to different temperature fluctuations of both laser cavities. This detuning increases the phase error of the locked lasers and can eventually make the lock unstable. To overcome this issue, optical injection locking can be combined with an OPLL to form an optical injection phase-locked loop (OIPLL) [43]. The operational principle is similar to that of OIL, but in addition the laser outputs are treated in the same way as in an OPLL. The feedback that acts on the slave laser then ensures that it follows the possible frequency drifts of the master laser.

If one has a powerful enough master laser, splitting off a part of its output for sideband generation and subsequent filtering might already yield enough optical power to drive the laser amplifiers sketched in figure 2.2 directly. This would make the additional slave laser and thus the extra locking schemes obsolete, but has the big disadvantage that the sideband filtering limits the tuning range of the master laser frequency, which is why this possibility has not been looked into further.

Now that the various possibilities of locking one Raman laser onto the other have been sketched, the OPLL will be described in more detail. The groundwork for this is laid in the following chapter, which introduces classical control theory as a means to describe a feedback loop in an abstract way.

Chapter 3

Classical control theory

In this work, the goal was to optimize the OPLL as much as possible in terms of phase-stability and loop bandwidth. In order to do this, a detailed understanding of the system is essential. To characterize the control loop in an abstract way, we describe it with classical control theory, which also reveals the limits to what performance is possible for a given system. In classical control theory, it is generally assumed that the systems under consideration are linear and time-invariant, which we expect to be true for the scope of this work. Similarly, it is sufficient that we discuss only single-input single-output systems here.

3.1 The transfer function

We treat any system as a black box, which is fully characterized by the relation between its input $x(t)$ and output $y(t)$. Instead of relating time-domain signal like $x(t)$ and $y(t)$, one can equivalently analyze the system's response in frequency domain. The function which relates input and output in frequency domain is called the transfer function. More general than the Fourier transform is the Laplace transformation, so one takes the Laplace transform $\mathcal{L}$ of the input and output functions $x(t)$ and $y(t)$. In the following, we will denote Laplace transforms of a function with the capital letter corresponding to its lower case letter in time domain. The Laplace transform of a function $g(t)$ is defined as

$$G(s) \equiv \mathcal{L}\left\{g(t)\right\}(s) = \int_0^\infty g(t)\mathrm{e}^{-st}\mathrm{d}t, \tag{3.1}$$

where $s = \sigma + i\omega$ with the frequency ω. If σ is larger zero, it attenuates the function with time. This allows the integration of functions which would not be integrable otherwise. The relation between input and output signals defines the transfer function:

$$F(s) = \frac{Y(s)}{X(s)} = \frac{\mathcal{L}\left\{y(t)\right\}(s)}{\mathcal{L}\left\{x(t)\right\}(s)}. \tag{3.2}$$

The transfer function can be written in terms of its zeros z_n and poles p_m, the roots of its nominator and denominator, respectively:

$$F(s) = K\frac{\prod_{n=1}^{N}(s - z_n)}{\prod_{m=1}^{M}(s - p_m)}. \tag{3.3}$$

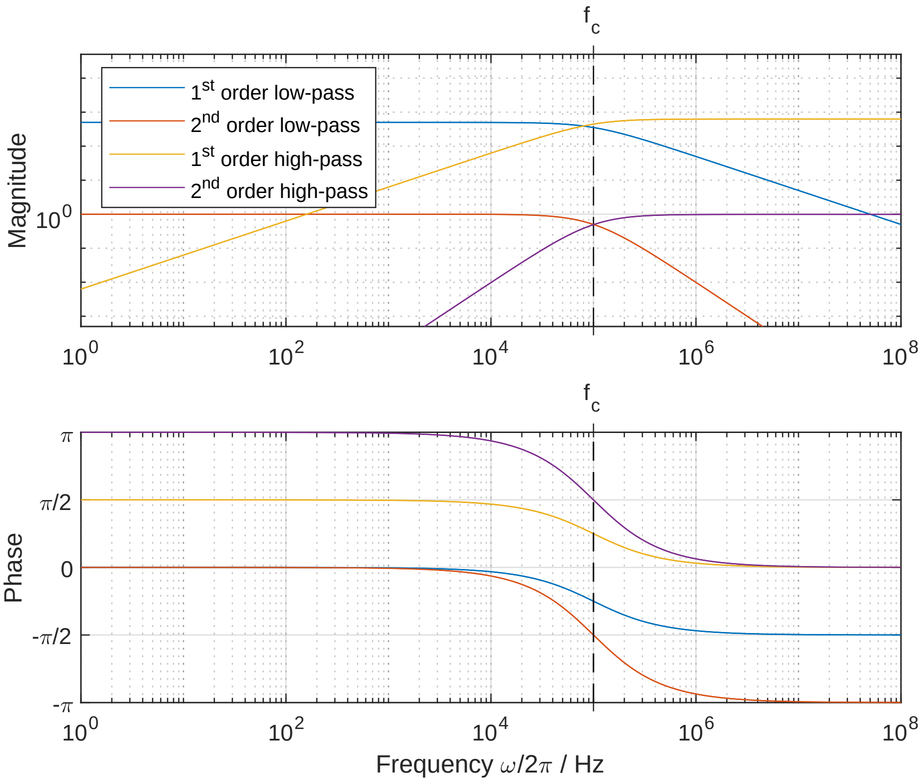

Figure 3.1: Bode plot showing the magnitude and phase for first and second order high- and low-pass filters with cutoff frequency f_c indicated by the dashed line. A slope of n order of magnitude in gain per frequency decade corresponds to a phase of $n\frac{\pi}{2}$, according to Bode's relations (3.6)

For many typical systems, the theoretical description in terms of zeros and poles is exact, whereas others can be approximated with this form using the function's Padé approximant [44]. The number and values of the poles and zeros can reveal much about the basic behaviour of the system, which will become important for the frequency modulation response of a semiconductor laser, see subsection 4.2.1.

Since transfer functions in general are complex-valued, it is instructive to consider both its magnitude, also called gain, and its phase. For all our applications, there is no need to add an additional attenuating factor to the time-domain functions for them to be integrable. So we set $\sigma = 0$ so that $s = i\omega$. Then, the Laplace transform reduces to the Fourier transform and the magnitude and phase can be visualized as functions of frequency. Usually, the behaviour is captured best on a double logarithmic scale in a so-called Bode plot. Figure 3.1 shows a Bode plot of the transfer functions of first and second order low- and high-pass filters, defined by

$$F_{k,f_c}^{(\mathrm{LP})}(i\omega) = K\left(\frac{1}{1+\frac{i\omega}{2\pi f_c}}\right)^k \tag{3.4}$$

$$F_{k,f_c}^{(\mathrm{HP})}(i\omega) = K\left(\frac{i\omega}{1+\frac{i\omega}{2\pi f_c}}\right)^k, \tag{3.5}$$

with k being the order of the filter and f_c its respective cutoff frequency. A low-pass filter has constant gain at low frequencies, and falling gain at frequencies higher than its cutoff frequency. For a high-pass filter, the situation is reversed: the gain rises up to the cutoff frequency, after which it stays constant. The order of the filter is equivalent to the respective number of first-order filters acting in series, i.e. its transfer functions being multiplied. For a higher-order filter, the slope of the rising or falling gain is steeper.

Bode plots like figure 3.1 are especially useful because they visualize Bode's relations, [45] which relate the magnitude and phase of the transfer function:

$$\frac{\mathrm{d}\log|F(i\omega)|}{\mathrm{d}\log\omega} = n \iff \arg F(i\omega) = n\frac{\pi}{2}. \tag{3.6}$$

They state that if the slope of the magnitude on a double logarithmic scale n is constant, the phase assumes a fixed value at the corresponding multiple of $\frac{\pi}{2}$. This gives an intuition that a rising gain results in a positive phase, called phase lead, and a falling gain is accompanied by a negative phase, called phase lag. Depending on the steepness of the slope, the phase lead/lag is larger or smaller. This means that for a second order filter, the phase lead/lag assumes value twice as large as for a first-order filter. Another observation is that although the gain changes around the cutoff-frequency, indicated by dashed lines, the phase change starts around a frequency decade earlier. At the cutoff frequency, the phase lead/lag has already assumed half its maximal/minimal value. In an experiment this means that even if a low-pass component has a high enough cutoff frequency so that the influence by its gain drop-off is negligible, the phase lag may still be noticeable.

Another thing to note is that Bode's relations should rather be regarded as inequality than as equality. [46] They give the minimum phase lag that a physical system can achieve, which is called the minimum-phase response. As we will see later again, other systems, for example ones that include signal delay, exhibit greater phase lag than predicted by Bode's relations. These are then termed non-minimum phase systems.

3.2 General feedback loop

We use the formalism of transfer functions to describe a general feedback loop in terms of control theory, which is shown schematically in figure 4.2. In the following, the respective arguments (t) and (s) of time-domain or Laplace transformed variables are omitted for better clarity. From an error signal e, the controller C produces a control signal u, which controls the plant P, i.e. the process to be controlled. Since this is often implemented with an electronic filter, C is also called control or loop filter. The process output together with a disturbance d yields the signal y. This is fed back and together with measurement noise n and the setpoint r it forms the error signal. In our case, disturbances could be temperature fluctuations or vibrations induced by other influences. Measurement noise would enter through devices like photodiodes, for example. C and P together form the open loop transfer function L. To describe all components which

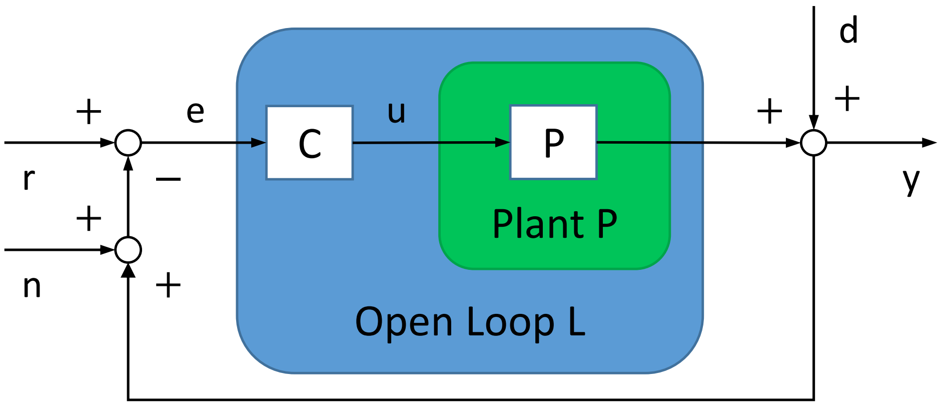

Figure 3.2: General scheme of a feedback loop. From an error signal e, the controller C produces a control signal u, which controls the plant P. The plant is the process to be controlled. The process output together with a disturbance d yields the signal y. This is fed back and together with measurement noise n and the setpoint r it forms the error signal. C and P together form the open loop transfer function L.

make up the loop, let us first consider the scheme without the feedback path. In this case, the signal y is connected to the setpoint r only via the controller C and the plant P and one can define the open loop transfer function

$$TF_{\mathrm{yr}}^{(\mathrm{open})} = CP =: L. \tag{3.7}$$

The plant represents the process which should be controlled. In our experiment, this is the laser head and any signal propagation delay, which will be treated in more detail in chapter 4.

Now let us include the feedback path and propagate the signal y back:

$$\begin{aligned} Y &= D + LE \\ &= D + L(R - N - Y). \end{aligned} \tag{3.8}$$

Solving for Y yields

$$Y = \frac{1}{1+L}D + \frac{L}{1+L}R - \frac{L}{1+L}N. \tag{3.9}$$

This gives us expressions for the effect of a disturbance d, the setpoint r or measurement noise n onto the signal y. Correspondingly, one can define the transfer functions

$$TF_{\mathrm{yd}} = \frac{1}{1+L} =: S \tag{3.10}$$

$$TF_{\mathrm{yr}}^{(\mathrm{closed})} = \frac{L}{1+L} \tag{3.11}$$

$$TF_{\mathrm{yn}} = -\frac{L}{1+L} =: -T. \tag{3.12}$$

Analogous to L, $TF_{\mathrm{yr}}^{(\mathrm{closed})}$ is the closed loop transfer function, i.e. the relation between signal and setpoint when the feedback loop is closed. Similarly, one can compute transfer functions to

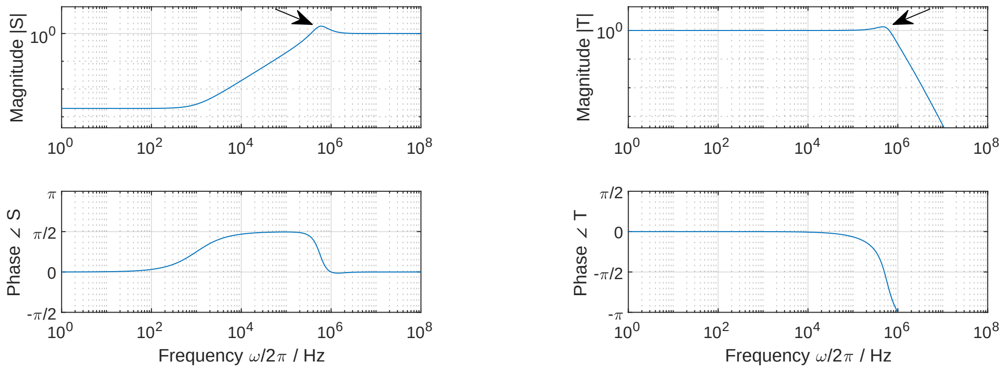

(a) (b)

Figure 3.3: (a) Sensitivity function $S(s)$ and (b) complementary sensitivity function $T(s)$ as defined in equations (3.10) and (3.12), for a low-pass open loop transfer function. The corresponding $L(s)$ is plotted in figure 3.4 and defined in equation (3.13). The arrows indicate where the magnitude is > 1, i.e. where disturbances and measurement noise are amplified to form servo bumps.

any other variable of interest, for example the error signal e, if one wants to examine how they are influenced by the other process variables.

In equations (3.10) and (3.12), we have also defined the sensitivity function $S(s)$ and the complementary sensitivity function $T(s)$. They are measures of the loop's sensitivity to disturbances or measurement noise, and its ability to attenuate either one of them. Figures 3.3a and 3.3b show how S and T look like for an example system where the control filter C is a first-order low-pass with cutoff frequency f_1, and the plant transfer function P is a second order low-pass with cutoff frequency f_2. Then, the open loop transfer function L is given by

$$\begin{aligned} L^{\text{example}}(i\omega) &= F^{(\text{LP})}_{1,f_1}(i\omega)\, F^{(\text{LP})}_{2,f_2}(i\omega) \\ &= K \frac{1}{\left(1 + \frac{i\omega}{2\pi f_1}\right)\left(1 + \frac{i\omega}{2\pi f_2}\right)^2}. \end{aligned} \tag{3.13}$$

L is plotted in figure 3.4 and will be discussed in more detail in section 3.3.

Ideally, one would like to reduce both S and T as far as possible, to attenuate both measurement noise as well as disturbance influences in the signal. However, there exists a trade-off between both, since for making L large, T becomes large, and for making L small, S becomes large. Moreover, S cannot be made arbitrarily small at all frequencies, which follows from Bode's sensitivity integral [45]:

$$\int_0^\infty \log |S(i\omega)|\, \mathrm{d}\omega = \pi \sum_m p_m, \tag{3.14}$$

where p_m are the right half-plane poles of L, i.e. where $\mathrm{Re}\,\{s\} \geq 0$. The poles are defined in the decomposition of L as in equation (3.3). This relation holds if $sL(s) \to 0$ for $s \to \infty$, which is true since all processes eventually exhibit low-pass behaviour at higher frequencies [45]. From Bode's sensitivity integral, and a similar, more complicated version for T [45], follows that there exist frequencies, for which $|S|$ or $|T| > 1$. This means that at these frequencies, disturbances or

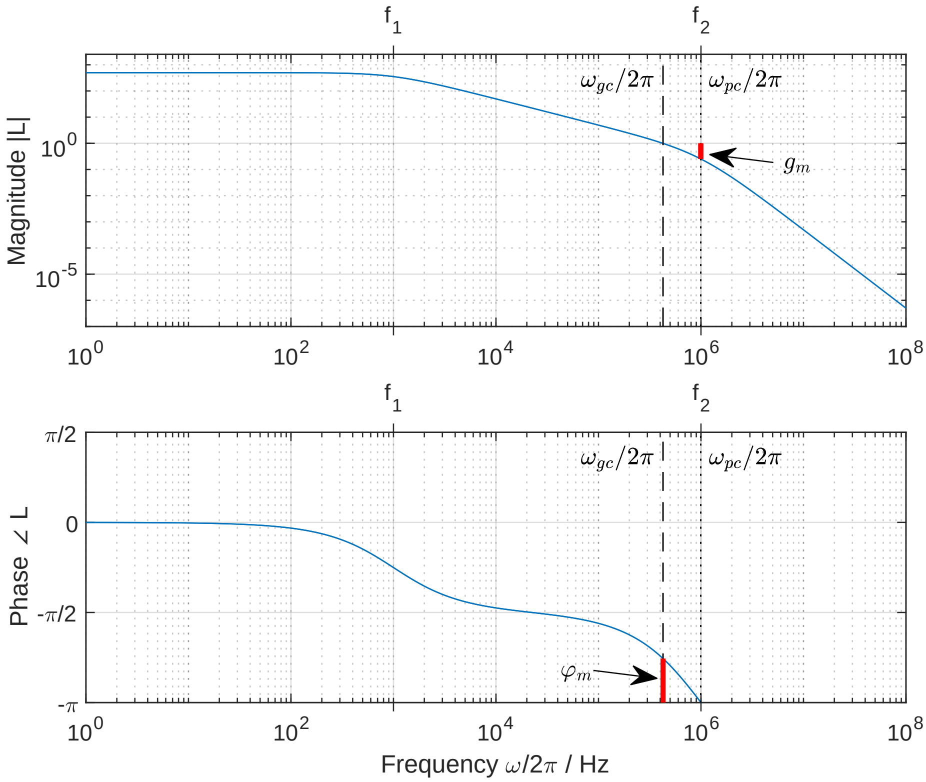

Figure 3.4: Open loop transfer function $L(s)$ for an example system with low-pass behaviour. The exact form of $L(s)$ is defined in equation (3.13), and f_1 and f_2 mark the two cutoff frequencies. The dashed line indicates the gain crossover frequency $\omega_{\mathrm{gc}}/2\pi$ as defined in equation (3.15), the dotted line marks the phase crossover frequency $\omega_{\mathrm{pc}}/2\pi$ as defined in equation (3.16). g_{m} and φ_{m} are the gain and phase margins, respectively.

noise are amplified instead of attenuated. In fact, this accumulation of spectral noise can become visible as a peak in the spectrum of the signal y. These bumps are called servo bumps [47] since they are caused by the servomechanism, i.e. the error-correcting feedback mechanism itself. As we will see in section 3.3, the servo bumps occur at a frequency which is indicative of the loop bandwidth, which is a performance measure of the feedback loop. Note that the frequency and gain of the servo bumps is strongly dependent on how the loop filter is shaped. Thus, one of the main uses of the loop filter is to influence the position and shape of the servo bumps. The loop filter and its optimal settings in this experiment are discussed in detail in section 4.3. As unwanted features in the signal spectrum, the servo bumps can play an important role in the experiment, and one must be aware of them. In section 4.5, the role of servo bumps in this experiment is examined.

3.3 Loop stability and phase reversal

Since S and T are completely determined by the open loop transfer function, lets look at some characteristic features of L, from which we can also draw conclusions about the stability of the loop. We use the same example system as in section 3.2, whose open loop transfer function is given by equation (3.13). Figure 3.4 shows L, plotted for example values of $K = 10^3$, $f_1 = 1$ kHz and $f_2 = 1$ MHz.

For a working loop, we want the error signal feedback to be amplified up to as high frequencies as possible, because then the negative feedback leads to correction of the error. To characterize the loop performance in this regard one defines the gain crossover frequency ω_{gc}, the smallest ω for which

$$|L(i\omega_{\mathrm{gc}})| = 1 = 0 \text{ dB}. \tag{3.15}$$

Above this frequency, amplification turns into attenuation and errors are not corrected efficiently anymore. One thus also speaks of the loop bandwidth, and we will later see that this is the frequency where servo bumps occur.

According to Bode's relations (3.6), the emerging low-pass behaviour at higher frequencies is accompanied by a phase lag. If multiple components act together, its slopes stack and produce a phase lag which exceeds that of a standard first-order low-pass filter. This poses a problem for the feedback loop, since for phases close to $-\pi$, positive feedback turns into negative feedback. This means for disturbances at this frequency, the feedback loop pushes the signal away from its setpoint instead of correcting for the error that the disturbance introduced. Thus, one also defines the phase crossover frequency ω_{pc}, the smallest ω for which

$$\arg L(i\omega_{\mathrm{pc}}) = -\pi. \tag{3.16}$$

One also speaks of this as the frequency of phase reversal.

If the gain at the phase crossover frequency is > 1, then the positive feedback is amplified and the loop becomes unstable. Thus, one criterion for a stable loop is the Bode stability criterion, which requires that the gain at ω_{pc} is smaller than unity, i.e. positive feedback is attenuated:

$$|L(i\omega_{\mathrm{pc}})| \overset{!}{<} 0 \text{ dB}. \tag{3.17}$$

In order to quantify how far the loop is from this critical point of instability, one defines the gain and phase margins g_{m} and φ_{m} [48]:

$$\begin{aligned} 10\log_{10}(g_{\mathrm{m}}) &= 0 \text{ dB} - 10\log_{10}|L(i\omega_{\mathrm{pc}})| \\ g_{\mathrm{m}} &= \frac{1}{|L(i\omega_{\mathrm{pc}})|} \end{aligned} \tag{3.18}$$

$$\varphi_{\mathrm{m}} = \pi + \arg L(i\omega_{\mathrm{gc}}). \tag{3.19}$$

In figure 3.4, g_{m} and φ_{m} are indicated with bold red lines. As we will see later in section 4.2, the frequency of phase reversal is the limiting factor to the performance of the feedback loop. Thus, an effort is made to shape the loop in a way which maximizes this frequency ω_{gc}.

From the definitions of S, T, ω_{gc} and φ_{m} (equations (3.10), (3.12), (3.15) and (3.19)), the following relation can be derived [48]:

$$|S(i\omega_{\mathrm{gc}})| = |T(i\omega_{\mathrm{gc}})| = \frac{1}{2\sin(\varphi_{\mathrm{m}}/2)}. \tag{3.20}$$

It relates the phase margin to the amplification or attenuation of disturbances and measurement noise, i.e. the magnitude of S and T, at the gain crossover frequency. Now if the phase margin is small enough so that the denominator becomes smaller than unity, we know that amplification occurs. This is the case for $\sin(\varphi_{\mathrm{m}}/2) < \frac{1}{2}$, so that

$$\varphi_{\mathrm{m}} < \frac{\pi}{3} \iff |S(i\omega_{\mathrm{gc}})| = |T(i\omega_{\mathrm{gc}})| > 1. \tag{3.21}$$

This relation not only reveals that the amplification of disturbances and noise occurs at the same frequency, but also that this happens at the gain crossover frequency, i.e. the limit of the loop bandwidth. From this we conclude that we can use the features of servo bumps as indicators of the loop bandwidth.

From equation (3.20), we also observe the stability criterion that the phase margin must be larger than zero. Otherwise, the denominator of the right-hand side would become zero which corresponds to infinite amplification of disturbances and measurement noise. In contrast, a loop with phase margin that is almost zero, but not quite, can still be stable, it just leads to very pronounced servo bumps. We use the tunable overall gain to operate in this regime and so determine the maximum achievable loop bandwidth for the given filter configuration. Note that equation (3.20) does not specify at which frequency S and T take on their maximum gain values. However, by operating with very little phase margin, we still know that there will be strong amplification at ω_{gc}, visible as servo bump. Now if the servo bump is very pointed, this means that its maximum is not too far off from ω_{gc}.

The maximum absolute value of S, $M_S = \max|S(i\omega)|$, is related to the gain and phase margin by the following inequalities [49]:

$$g_{\mathrm{m}} \geq \frac{M_S}{M_S + 1} \tag{3.22}$$

$$\varphi_{\mathrm{m}} \geq 2 \arcsin \frac{1}{2M_S}, \tag{3.23}$$

where equation (3.23) follows from equation (3.20). The inequalities allow to infer the minimum phase and gain margin the loop must have in order to avoid amplification of disturbances over a certain level.

Chapter 4

Phase-locking of Raman lasers

As discussed in subsection 2.2.1, it is necessary to stabilize the phase of one of the Raman IR seed lasers with respect to the other. This can be achieved with a heterodyne optical phase-locked loop.

4.1 Heterodyne optical phase-locked loop

A phase-locked loop is a control mechanism which affects the input signal with the aim to minimize the difference between input phase and a setpoint phase. In an optical phase-locked loop (OPLL), the signal to be controlled is the phase of an oscillating electromagnetic field of a highly coherent light source, like a laser. Then the setpoint is given by a laser field as well, which is at a similar frequency. This "master laser" sets the frequency and phase to which the "slave laser" shall be locked. The total phase difference of the electric fields is detected by interference on a photodiode. To avoid noise on the photodiode, the lasers are locked to slightly different frequencies, where the difference frequency is set by a phase-stable RF source. From this, one obtains an error signal as described in chapter 3, which is amplified and shaped in a control filter. The output of the filter is connected to the laser to apply negative feedback and to correct for the detected error.

In the following subsection, the propagation of signals through the loop is described in more detail, from which it becomes clear how the two laser phases are compared to each other. Subsection 4.1.2 then discusses the way in which feedback is applied to the slave laser.

4.1.1 Signal propagation through the loop

Figure 4.1 is a scheme of a general heterodyne OPLL as implemented in this project. Two fields $\mathcal{E}_\mathrm{M}$ and $\mathcal{E}_\mathrm{S}$ from a master and slave laser, respectively, oscillate at average frequencies ω_M and ω_S with phases ϕ_M and ϕ_S. To the slave laser, a noise term is added, which accounts for imperfections in photodetection and other noise sources. For the master laser, the noise is already included in ϕ_M. The laser fields are overlapped on a photodiode, at which they have the following form:

$$\mathcal{E}_\mathrm{M} = \mathrm{Re}\left\{E_\mathrm{M}\mathrm{e}^{i\omega_\mathrm{M}t+i\phi_\mathrm{M}}\right\} \tag{4.1}$$

$$\mathcal{E}_\mathrm{S} = \mathrm{Re}\left\{E_\mathrm{S}\mathrm{e}^{i\omega_\mathrm{S}t+i(\phi_\mathrm{S}+\phi_n)}\right\}, \tag{4.2}$$

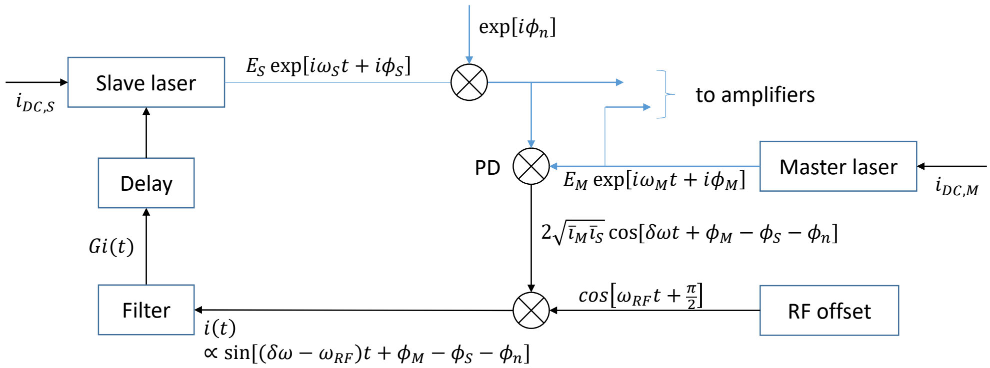

Figure 4.1: Scheme of a heterodyne optical phase-locked loop (OPLL). See text for detailed description. Blue/black lines represent optical or electrical connections, respectively.

written in terms of complex wave functions with amplitudes E_M and E_S. The output current of the photodiode is proportional to the optical power P, which in turn is the optical intensity I integrated over the detector area: $P = \int_{A_\mathrm{PD}} I \mathrm{d}A$. Proper alignment of the laser beams ensures that the angle between wavefronts and detector is small enough so that the optical phase does not vary over the detector area. The optical intensity I is the modulus squared of the incident electric field(s):

$$\begin{aligned} I &= \left| E_\mathrm{M} \mathrm{e}^{i\omega_\mathrm{M} t + i\phi_\mathrm{M}} + E_\mathrm{S} \mathrm{e}^{i\omega_\mathrm{S} t + i(\phi_\mathrm{S} + \phi_n)} \right|^2 \\ &= |E_\mathrm{M}|^2 + |E_\mathrm{S}|^2 + 2\,|E_\mathrm{M}|\,|E_\mathrm{S}| \cos\left[\delta\omega t + \phi_\mathrm{M} - \phi_\mathrm{S} - \phi_n\right], \end{aligned} \tag{4.3}$$

with the difference frequency $\delta\omega = \omega_\mathrm{M} - \omega_\mathrm{S}$, which is sometimes also called intermediate frequency. If it is non-zero, i.e. the fields on the photodiode now have different frequencies, one speaks of heterodyne detection. In analogy to acoustics, one can also speak of a beat note between the two laser fields. The third term represents this interference between both electric fields. Its contrast would be reduced if the optical phases were not constant across the detector area. The mean photocurrent $\bar{i}_\mathrm{PD}(t)$ at the output of the photodiode is thus given by:

$$\bar{i}_\mathrm{PD}(t) = \frac{\eta e}{\hbar\bar{\omega}} P(t) \tag{4.4}$$

$$= \bar{i}_\mathrm{M} + \bar{i}_\mathrm{S} + 2\sqrt{\bar{i}_\mathrm{M}\bar{i}_\mathrm{S}} \cos\left[\delta\omega t + \phi_\mathrm{M} - \phi_\mathrm{S} - \phi_n\right], \tag{4.5}$$

where η is the detector quantum efficiency, $\bar{i}_\mathrm{M}$ and $\bar{i}_\mathrm{S}$ the photocurrents created by the master and slave laser individually, and $\bar{\omega} = \frac{\omega_\mathrm{S} + \omega_\mathrm{M}}{2}$ [50]. Note that, as here, the photodiode is often formally depicted as frequency mixer. However, the optical intensity is defined as twice the average of the squared wave function over a time much longer than an optical cycle. This means that the photocurrent only contains a frequency component oscillating at the difference and not the sum frequency. For the OPLL, the difference frequency is the relevant one.

For a better loop performance, it is advantageous to reduce optical and electrical noise as much as possible. Many electrical components in the laboratory work with frequencies below 1 MHz, leading to noise pickup in that frequency range. Also, there is pink noise which scales inversely with frequency. Influence of both can thus be reduced by operating at higher frequencies wherever possible, for example on the photodiode. For the OPLL, this is achieved by introducing an additional radio frequency (RF) offset between the laser frequencies. This means the frequency of one laser is separated from the other by the RF offset frequency, i.e. $\delta\omega \approx \omega_{\mathrm{RF}}$. Then, in an additional step, the photocurrent is mixed with the offset signal at ω_{RF}, which gives the error signal current:

$$\begin{aligned} i_{\text{error}}(t) &\propto \cos\left[\omega_{\mathrm{RF}}t + \tfrac{\pi}{2}\right]\cos\left[\delta\omega t + \phi_{\mathrm{M}} - \phi_{\mathrm{S}} - \phi_n\right] \\ &= \frac{1}{2}\sin\left[(\delta\omega - \omega_{\mathrm{RF}})t + \phi_{\mathrm{M}} - \phi_{\mathrm{S}} - \phi_n\right] - \frac{1}{2}\sin\left[(\delta\omega + \omega_{\mathrm{RF}})t + \phi_{\mathrm{M}} - \phi_{\mathrm{S}} - \phi_n\right], \end{aligned} \tag{4.6}$$

where we assume that any phase fluctuations of the RF source are negligible. Using an additional RF offset also has the advantage that one can control the optical phase of the slave laser by adjusting the electronic phase of the RF source. From both frequency components $\delta\omega \pm \omega_{\mathrm{RF}}$, the difference frequency is the one of interest, which will yield the error signal in the end. Slow components like the loop filter will eliminate the sum frequency component, but for convenience one already here considers only the difference frequency component. This can be justified because we assume all components to respond linearly. The same argument holds for other higher frequency components, like ones resulting from other sidebands created by the EOM as described in subsection 2.3.1. In our case actually, the photodiode would have attenuated such frequency components already since its cutoff frequency is much lower than the sideband splitting.

As mentioned before, the difference frequency and the RF frequency are similar: $\delta\omega \approx \omega_{\mathrm{RF}}$. The difference component thus oscillates almost at direct current (DC). If also the optical phases do not deviate very much from each other, then the argument of the sine is $<< 1$ and we can make the small angle approximation:

$$\begin{aligned} i_{\text{error}}(t) &\propto \sin\left[(\delta\omega - \omega_{\mathrm{RF}})t + \phi_{\mathrm{M}} - \phi_{\mathrm{S}} - \phi_n\right] \\ &\approx (\delta\omega - \omega_{\mathrm{RF}})t + \phi_{\mathrm{M}} - \phi_{\mathrm{S}} - \phi_n. \end{aligned} \tag{4.7}$$

We thus obtain an error signal current, which is proportional to the difference between master and slave laser frequencies, offset by the RF frequency.

This error signal current is fed into a control filter corresponding to C in chapter 3, which can be of varying complexity. The device used in the experimental setup is described in section 4.3. Here we include only a simple proportional filter so that the output current is given by $Gi_{\text{error}}(t)$ where the constant G is called main gain. A simple filter like this is sufficient for a working feedback loop as we will show in subsection 4.1.2. Still, the loop performance can be improved by shaping the loop filter in more complicated ways, which is described in section 4.3.

So far, all propagating currents have been treated as real quantities. However, a more complex loop filter, as well as signal propagation delay and low-pass behaviour of other components, introduces a frequency-dependent phase shift, which we describe with transfer functions like in chapter 3. It is not essential for the basic understanding of a phase-locked loop, but will introduce limitations to the performance of the loop, which will be discussed in section 4.2.

Due to the finite speed of signal propagation in electrical cables or optical fibers, delay is accumulated over the whole signal path. The distributed delay can be treated as a single 'localized' component, which is why it is included in the scheme. However for this section, we ignore it and assume the input current modulation of the slave laser to be $i_{\text{mod}}(t) = Gi_{\text{error}}(t)$.

In order to complete the phase-locked loop, one has to link input current to the frequency of the slave laser field, which will be discussed in the following subsection.

4.1.2 Semiconductor laser as current-controlled oscillator

There are different paths that can be used to apply feedback to the laser frequency. Since we want to compensate for errors as fast as possible, the feedback path should also exhibit a fast response.

In general, controlling the laser field frequency can be achieved by modulating the output field with an electro-optic or acousto-optic phase shifter, which would be driven by a voltage-controlled oscillator (VCO). However, this would introduce additional external components in the beam path and their respective losses. Alternatively, one can apply a voltage to the piezo-controlled mirrors which form the laser cavity and tune the resonance frequency in this way. In fact, we use this as one feedback path, but it has the disadvantage of exhibiting slower response times than external phase shifters. Although loop bandwidths of the order of 100 kHz have been demonstrated, the typical bandwidth achieved with piezoelectric mirrors is of the order of 10 kHz [51]. With its large tuning range, it is suitable to counteract slow drifts in the laser frequency, but there is still the need to compensate for faster fluctuations. A semiconductor laser (SCL) like a diode laser has the advantage of offering a third option, which is directly modulating the current that pumps the gain medium and thus influences the frequency of maximal gain. The SCL then acts as current-controlled oscillator, the optical equivalent to a VCO. This scheme does not require outside components after the laser. Also, as we will see in subsection 4.2.1, the response of the laser current modulation is faster than the modulation bandwidth of a few KHz of the piezo-controlled mirrors. This allows one to compensate for errors with higher frequency components.

Following [52], it is shown how the output frequency of a slave SCL can be locked by feeding an error signal like in equation (4.7) into its current modulation port. For simplification, we are neglecting any additional noise ϕ_n for this treatment. So far, no time dependence of laser frequencies and phases has been denoted. The purpose of the OPLL is to compensate for fluctuations in these quantities, so we define the instantaneous frequency of the slave laser field as

$$\omega_{\mathrm{S}}(t) = \langle\omega_{\mathrm{S}}\rangle + \Delta\omega_{\mathrm{S}}(t), \tag{4.8}$$

with $\Delta\omega_{\mathrm{S}}(t) = \frac{\mathrm{d}}{\mathrm{d}t}\phi_{\mathrm{S}}(t)$ and $\langle\Delta\omega_{\mathrm{S}}(t)\rangle = 0$. What was formerly denoted as ω_{S} is now the mean frequency $\langle\omega_{\mathrm{S}}\rangle$, and all fluctuations are absorbed in the time-dependent phase $\phi_{\mathrm{S}}(t)$.

The frequency change of a SCL can also be influenced by its input current. For this, we are taking only into account the electrical response of the laser diode, not the thermal response. In subsection 4.2.1, the implications of both responses acting together will be discussed in more detail. For frequencies well below the electrical modulation resonance of the SCL, i.e. the cutoff of the electrical response, the $\Delta\omega_{\mathrm{S}}(t)$ is given by the following:

$$\Delta\omega_{\mathrm{S}}(t) = a\frac{\mathrm{d}}{\mathrm{d}t}\Delta i_{\mathrm{S}}(t) + b\Delta i_{\mathrm{S}}(t), \tag{4.9}$$

where $\Delta i_{\mathrm{S}}(t) = i_{\mathrm{S}}(t) - i_{\mathrm{S,th}}$ is the excess of the total current in the slave laser gain medium $i_{\mathrm{S}}(t)$ over its threshold value $i_{\mathrm{S,th}}$. a and b are constants depending on the gain medium and the laser cavity. Note that $\Delta i_{\mathrm{S}}(t)$ is not equal to $i_{\mathrm{mod}}(t)$, but $i_{\mathrm{DC}} + i_{\mathrm{mod}}(t) = i_{\mathrm{S}}(t) = i_{\mathrm{S,th}} + \Delta i_{\mathrm{S}}(t)$.

As seen in subsection 4.1.1, the error signal current is given by

$$i_{\mathrm{error}}(t) \approx K\left[(\langle\delta\omega\rangle - \omega_{\mathrm{RF}})t + \phi_{\mathrm{M}}(t) - \phi_{\mathrm{S}}(t)\right], \tag{4.10}$$

where is K is some proportionality constant. We treat ω_{RF} as a constant because we assume that the phase fluctuations of the RF source are much smaller than that of the semiconductor laser. If this were not the case, it would not make sense to use the RF source as setpoint for the

OPLL. Taking the derivative with respect to time on both sides yields

$$\frac{\mathrm{d}}{\mathrm{d}t} i_{\mathrm{error}}(t) = K\left[(\langle\delta\omega\rangle - \omega_{\mathrm{RF}}) + \frac{\mathrm{d}\phi_{\mathrm{M}}(t)}{\mathrm{d}t} - \frac{\mathrm{d}\phi_{\mathrm{S}}(t)}{\mathrm{d}t}\right] \tag{4.11}$$

$$\frac{1}{K}\frac{\mathrm{d}}{\mathrm{d}t} i_{\mathrm{error}}(t) = (\langle\delta\omega\rangle - \omega_{\mathrm{RF}}) + \frac{\mathrm{d}\phi_{\mathrm{M}}(t)}{\mathrm{d}t} - a\frac{\mathrm{d}}{\mathrm{d}t}\Delta i_{\mathrm{S}}(t) - b\Delta i_{\mathrm{S}}(t) \tag{4.12}$$

$$\frac{1}{K}\frac{\mathrm{d}}{\mathrm{d}t}\Delta i_{\mathrm{error}}(t) = (\langle\delta\omega\rangle - \omega_{\mathrm{RF}}) + \frac{\mathrm{d}\phi_{\mathrm{M}}(t)}{\mathrm{d}t} - aG\frac{\mathrm{d}}{\mathrm{d}t}\Delta i_{\mathrm{error}}(t) - bG\Delta i_{\mathrm{error}}(t), \tag{4.13}$$

where in the first step, $\frac{\mathrm{d}}{\mathrm{d}t}\phi_{\mathrm{S}}(t) = \Delta\omega_{\mathrm{S}}(t)$ was replaced with equation (4.9), and in the second step $\Delta i_{\mathrm{error}}(t) = \frac{\Delta i_{\mathrm{S}}(t)}{G} = i_{\mathrm{error}}(t) + \frac{1}{G}(i_{\mathrm{DC}} - i_{\mathrm{S,th}})$ was introduced. This differential equation now links the phase of the master laser $\phi_{\mathrm{M}}(t)$ to a current change $\Delta i_{\mathrm{error}}(t)$ in the loop, depending on the loop filter and the difference between beat note frequency $\delta\omega$ and the RF offset ω_{RF}.

In the steady state, all derivatives are zero, which leads to

$$\langle\delta\omega\rangle - \omega_{\mathrm{RF}} = bG\Delta i_{\mathrm{error}}^{(\mathrm{SS})}. \tag{4.14}$$

Similarly, equation (4.9) gives

$$\Delta\omega_{\mathrm{S}}^{(\mathrm{SS})} = bG\Delta i_{\mathrm{error}}^{(\mathrm{SS})}. \tag{4.15}$$

From this follows $\Delta\omega_{\mathrm{S}}^{(\mathrm{SS})} = \langle\delta\omega\rangle - \omega_{\mathrm{RF}}$ and thus the instantaneous frequency of the slave laser in the steady state is equal to

$$\omega_{\mathrm{S}}^{(\mathrm{SS})} = \langle\omega_{\mathrm{S}}\rangle + \Delta\omega_{\mathrm{S}}^{(\mathrm{SS})} = \langle\omega_{\mathrm{M}}\rangle - \omega_{\mathrm{RF}}, \tag{4.16}$$

which is what we wanted to achieve with the phase-locked loop. In this simplified treatment, the slave laser frequency is not fluctuating anymore, but remains fixed at a value equal to the frequency of the master laser, offset by the RF frequency. In reality, noise introduced by components in the loop reduces the accuracy with which the slave laser is held at the lock frequency. Also, signal propagation delay and response times of all elements in the loop limit the speed with which the loop compensates phase fluctuations. Most notably, the thermal response of the laser diode, the optical and electrical path length, and the cutoff frequency of the loop filter electronics add up to form a loop which can typically compensate fluctuations with frequency components of up to a few MHz. Connecting this to the laser linewidth means that only lasers with smaller linewidth can have all their optical power locked to the master laser frequency.

4.2 Performance limitations

In order to discuss the limitations of the feedback loop, we draw on classical control theory, which was introduced in chapter 3. This means we look at the relations between input and output signals in the frequency domain, so that a system's response is quantified by its transfer function. Examining the transfer functions of the OPLL components thus allows to identify the limitations each one introduces.

Figure 4.2 is a scheme of an OPLL in terms of control theory, similar to figure 3.2 in chapter 3. Here however, the plant is specified in more detail. It consists of the laser head and signal propagation delay, with transfer function Θ. In this form, any systematic nonlinearity of additional components like the photodiode is neglected. Note that its noise still enters through n. In the laser head, in addition to the frequency modulation response H, the conversion from frequency to phase with an integration term I has to be taken into account. So together, the plant transfer function is $P = HI\Theta$. Each of these three terms contributes to limiting the performance of the OPLL and they will be discussed separately in the following subsections. Subsection 4.2.4 is then focusing on how their respective influences can be compensated for.

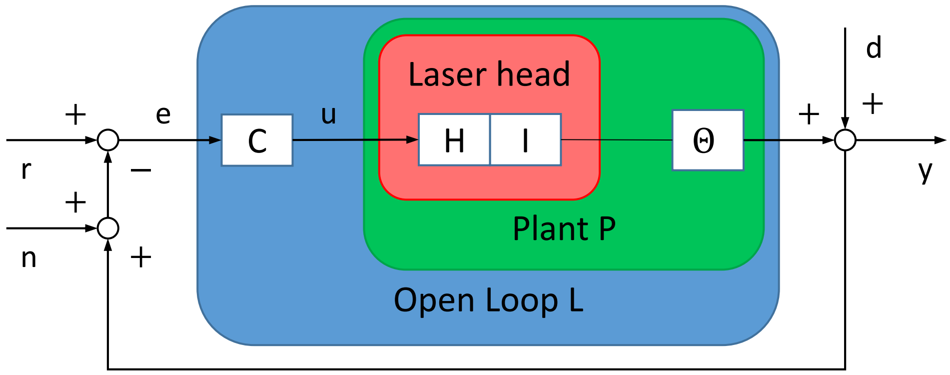

Figure 4.2: Scheme of the OPLL in terms of control theory. Similar to figure 3.2, the output of the plant P together with a disturbance d yields the output signal y. This is measured, introducing measurement noise n, and is compared to the setpoint r, creating an error signal e which the control filter turns into a suitable control signal u. In an OPLL the plant is formed by the laser head and delay Θ, neglecting any frequency-dependent behaviour from other sources like the photodiode. The laser head formally consists of its frequency modulation response H and an integration term I. H, I and Θ are discussed in subsections 4.2.1, 4.2.2 and 4.2.3, respectively.

4.2.1 Diode laser frequency modulation response

The frequency modulation response of a SCL is composed of two parts. Modulating the current that runs through the laser diode changes the carrier density in the gain medium. This in turn has an effect on its refractive index, which influences the wavelength of maximum gain. It can be modeled using small-signal rate equations [53] and we will call this pathway the electrical response of the SCL. On the other hand, the injection current and stimulated emission also act as a heat source, which via thermal expansion also change the resonance frequency of the laser. We call this pathway the thermal response of the laser diode.

The first quantitative description of the thermal response was given in [54], and phenomenologically describes it as a modified low-pass filter (LPF):

$$H_{\mathrm{th}}^{(\mathrm{LPF})}(i\nu) \propto \frac{1}{1+\sqrt{i\nu}}, \tag{4.17}$$

where $\nu = \frac{f}{f_{\mathrm{c}}}$ is the normalized modulation frequency and f_{c} is the cutoff frequency of the low-pass filter. A more physical description is based on treating the gain medium as a single layer and the injection current as a heat source at its center. Then, modeling the one-dimensional heat flow and connecting it to the frequency via the thermal expansion and refractive index coefficients, the transfer function is of the form [55]

$$H_{\mathrm{th}}^{(\mathrm{heatflow})}(i\nu) \propto \frac{\tanh\left(\sqrt{i\nu}\right) + \tanh\left(\frac{\sqrt{i\nu}}{2}\right)}{\sqrt{i\nu}}. \tag{4.18}$$

It is not very clear which of both transfer functions represents experimental results the best: Correc *et al.* [56] find that the transfer function based on the physical heat flow model fits their results better, whereas Satyan [42] discards it since the empirically found modified low-pass filter fits best.

For the electrical response, the only limiting factor is the stimulated lifetime of the carrier electrons, which allows for modulation frequencies of up to > 20 GHz [52]. For frequencies below 10 MHz however, the thermal response is the dominant one, with cutoff frequencies ranging from around 50 kHz [54–56] to 1.8 MHz [42]. This means in the regime of modulation frequencies up to a few MHz, the electrical response can be considered constant: $H_{\mathrm{el}} = K_{\mathrm{el}}$.

Together, the transfer function for the frequency modulation response of the diode laser is given by

$$H(i\nu) = K_{\mathrm{el}} - K_{\mathrm{th}} H_{\mathrm{th}}(i\nu). \tag{4.19}$$

Here, the exact form of the thermal response is not crucial. The important point to note is that both contributions enter with a different sign. This means that in the crossover region, where the thermal response drops off, they cancel each other out and a diminished response is observed as a dip in magnitude between 0.1 to 10 MHz [42, 56]. After the thermal response has dropped off, the gain as well as the phase due to the electrical response stays constant. Still, the different sign between both terms causes the overall phase of H to be $-\pi$, contrary to what would be expected from Bode's relations (cf. chapter 3). This means that H exhibits a non-minimum phase response. More specifically, H forms a non-minimum phase zero, or right-half plane zero. This feature is a general issue for control mechanisms, because it can cause an initial undershoot in the system response, i.e. the response initially goes into the wrong direction [45, 57].

Overall, the frequency modulation response of the SCL shows a phase reversal and as discussed earlier, this will limit the performance of a feedback loop which is based on this pathway.

4.2.2 Feedback onto frequency instead of phase

Following the small signal analysis in subsection 4.1.1, the quantities considered as signals for the OPLL are the phases of the oscillating electrical fields. However, as has been discussed in subsection 4.1.2, modulation of the current that runs through the laser diode acts on the frequency at which the laser oscillates. So in order to obtain the output signal of the laser head in terms of phase again, the frequency has to be converted to total phase by the integral $\phi = \int \omega(t)\mathrm{d}t + \phi_0$.

This means that in addition to the frequency modulation response H, the laser head transfer function is formed by an integral term I. The Laplace transform of the integration operation is a division by s, which gives $I = \frac{1}{s}$. The gain of this transfer function on a double-logarithmic scale has a slope of -1. Thus it follows from Bode's relations (3.6) that the phase assumes a constant value at $-\frac{\pi}{2}$. Just from the fact that the feedback in the loop acts on frequency and not phase, half of the phase margin until the point of phase reversal is already not available anymore. Hence, a feedback path directly onto phase would greatly benefit the OPLL.

4.2.3 Signal delay

Already in the beginning of fiber-optic communication development, which also brought up OPLLs, it was realized that the loop performance is decreased if the signal propagation delay is non-negligible [58]. As mentioned earlier, the distributed delay over the whole loop can be treated as a single component with the transfer function

$$\Theta(s) = \mathrm{e}^{-sT_{\mathrm{d}}}, \tag{4.20}$$

where T_{r} is the signal delay when it goes through the loop once. If, like in our case, $\sigma = 1$, $|\Theta| = 1$ for all frequencies, thus it does not have a direct influence on the amplification of noise or the attenuation of disturbances. However, it introduces a significant phase lag for higher

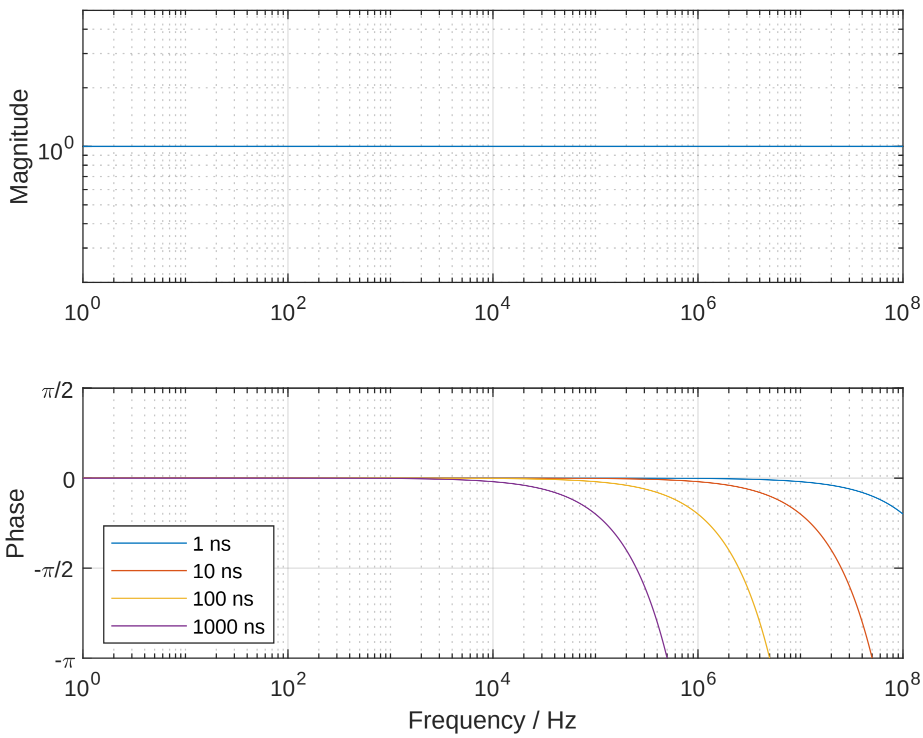

Figure 4.3: Bode plot of Θ, the transfer function for signal propagation delay, for different values of T_d. Significant phase lag in the few MHz regime occurs already at tens of ns delay.

frequencies, and this can vastly limit the loop bandwidth. As mentioned in chapter 3, this is a non-minimum phase response, exceeding the phase lag predicted by Bode's relations. For a loop composed by simple components, one can calculate limits for the maximum value attained by the product of delay and loop bandwidth [58]. This is not pursued here due to our uncertainty of exact transfer functions, like the laser frequency modulation response (cf. subsection 4.2.1), or cutoff frequencies.

Figure 4.3 is a Bode plot of Θ for various time delays T_d. Already a time delay of 100 ns leads to a phase lag of $\frac{\pi}{4}$ for frequencies of a few MHz, 1 ms delay leads to the same lag already for a few 100 kHz. For low phase lag in the few MHz regime, one should rather keep the delay below 10 ns, which corresponds to 3 m of free space light propagation, or around 2 m of signal propagation through cables and optical fibers. With connections between every component contributing to the delay, a normal setup in the laboratory quickly arrives at these values. [31] gives an overview of recent work where this limitation is tackled by the use of integrated optics. In our setup, an effort is made to keep the electrical connections as short as feasible, and custom made fiber splitters and combiners are employed.

4.2.4 Compensation

The main problem which limits the loop bandwidth is the increasing phase lag of the plant at higher frequencies. As mentioned in section 3.3, this eventually leads to a phase reversal which turns positive into negative feedback, thus limiting the maximum frequency at which errors can be corrected. Accordingly, one can compensate for this issue by introducing phase lead at higher frequency, which can be achieved by employing a suitable control filter C. From Bode's relations (3.6) follows that a gain with positive slope leads to phase lead. However, a positive slope means that the controller has to provide increasingly large gain, which becomes challenging at higher frequencies due to the controllers innate low-pass behaviour. Therefore, it is useful to limit the phase lead to a smaller frequency region where it is required. Still, this frequency region should not be too small in order to keep robustness. Also, more phase lead than with a simple first-order filter can be obtained by cascading multiple components, leading to a steeper slope in gain. Ultimately, the highest crossover frequency is limited by the achievable gain at high frequencies.

For this work, we did not measure the frequency modulation response of the employed diode laser, but the previous works [42, 54–56] give an understanding of the phase reversal and how one can compensate for it. We need phase lead at frequencies close to the crossover, and we want to minimize the additional phase lag introduced by signal propagation delays.

4.3 Toptica Fast Analog Linewidth Control (FALC)

Phase lead close to the phase crossover frequency can be introduced by appropriately shaping the employed control filter, which corresponds to C in figure 4.2. The control filter we use in this setup is the Toptica mFALC 110. To understand the Fast Analog Linewidth Control (FALC), it is useful to first introduce what a PID controller is, since the basic concepts of both filters are similar.

A PID controller is a filter with three stages, for which the gain can be controlled individually. The P term has no frequency dependence and gives a control signal proportional to the error signal. The I term outputs a signal proportional to the integral of the error signal with respect to time. This is needed so that the output signal arrives at the setpoint in a finite time. However, a too strong I term will accumulate to a large control signal if the output signal deviates from the setpoint a lot. This causes it too overshoot the setpoint and eventually settle after a number of oscillations. The D term produces a control signal proportional to the derivative of the error signal with respect to time, which aims to anticipate the signal corrections and thus prevent overshoot. The output control signal $u(t)$ of a PID controller for a given input error signal $e(t)$ is thus given by

$$u(t) = K_{\mathrm{p}} e(t) + K_{\mathrm{i}} \int_0^{t'} \mathrm{d}t' e(t') + K_{\mathrm{d}} \frac{\mathrm{d}}{\mathrm{d}t} e(t), \tag{4.21}$$

and its transfer function C is

$$C(s) = K_{\mathrm{p}} + K_{\mathrm{i}} \frac{1}{s} + K_{\mathrm{d}} s. \tag{4.22}$$

The proportional term has a gain constant with frequency, and thus provides neither phase lead, nor phase lag. The gain of the integrator term has a slope of -1 on a double-logarithmic scale, i.e. -10 dB per frequency decade, which is accompanied by a phase lag of $-\frac{\pi}{2}$ and thus leads to phase lag. The derivative term has a gain slope of 1 and gives a phase lead of $\frac{\pi}{2}$. In practice, the behaviour of a PID controller will exhibit some frequency dependence in its response, and different components might be suitable for different applications. In the FALC, the PID stages are implemented in a way that they only act in specific frequency ranges. This is obtained by a transfer function with one zero and one pole:

$$F(s) = \tilde{K}\frac{p+s}{z+s} = K\frac{1+i\frac{f}{f_\mathrm{z}}}{1+i\frac{f}{f_\mathrm{p}}}. \tag{4.23}$$

A filter in which the stages take this form which yields phase lead or lag only over the frequency range between f_z and f_p is called a lead-lag compensator.

Figure 4.4 is a Bode plot of equation (4.23) for different combinations of zero and pole corner frequencies f_z and f_p. The respective f_z are marked with crosses, the f_p with open circles. One can distinguish two general cases.

If $f_\mathrm{z} < f_\mathrm{p}$ (blue and red curves), the gain rises with a slope of up to 10 dB per decade between both frequencies. Over this range, the phase is positive and the stage acts as a differentiator. Note that although the maximum phase of around $\frac{\pi}{2}$ is only achieved if the slope is constant over a large range. For an only shortly rising gain (red curve), the phase stays far below this maximum value. On the other hand, the phase starts to increase already long before the corner frequency. In fact, for the blue curve the phase almost reached the value $\frac{\pi}{4}$ at the $f = f_\mathrm{p}$.

If $f_\mathrm{z} > f_\mathrm{p}$ (yellow and purple curves), the gain decreases with a slope of down to -10 dB per decade between both frequencies. This means the stage acts as an integrator and the phase is negative with a minimal value of around $-\frac{\pi}{2}$, if the frequency range is large enough. Similarly to before, now the purple curve does not reach this value by far. And again, the decrease in gain slope is heralded by the change in phase.

For both cases applies that at f_z, the second derivative of the gain with respect to frequency is negative, whereas at f_p, it is positive. Note also that for the same value of initial gain, a broader frequency range where the stage acts as differentiator (integrator) results in a higher (lower) final gain at high frequencies when compared to a smaller frequency range. Thus, as mentioned in subsection 4.2.4, a phase lead over a broad frequency range must be earned by providing large gain values at high frequencies.

The FALC is composed of four such stages in series: three integral terms and one derivative term. For each, the operating frequency range can be shifted by choosing different settings, which then also fix its width. Figure 4.5 is a Bode plot of the FALC transfer function calculated using four stages like in equation (4.23). The zero and pole corner frequencies were chosen according to a typical example setting in the FALC manual. There, the very fist stage, the extra slow limited integrator (XSLI), was left off (setting 6). The corner frequencies of the second stage, the slow limited integrator (SLI), were $f_\mathrm{z}^\mathrm{SLI} = 30$ kHz and $f_\mathrm{p}^\mathrm{SLI} = 500$ Hz (setting 4). The corner frequencies of the third stage, the fast limited integrator (FLI), were $f_\mathrm{z}^\mathrm{FLI} = 800$ kHz and $f_\mathrm{p}^\mathrm{FLI} = 65$ kHz. The corner frequencies of the fourth stage, the fast limited differentiator (FLD), were $f_\mathrm{z}^\mathrm{FLD} = 4.2$ MHz and $f_\mathrm{p}^\mathrm{FLD} = 22.5$ MHz. The last value was not provided, but was interpolated based on the spacing of the other corner frequency settings. Comparing with the FALC transfer function network analysis provided in the manual [59], the shapes of both magnitude and phase agree well. For the phase, also the absolute values match well, whereas for the magnitude they do not agree. The first reason for that is that the manual does not provide an absolute setting for the overall gain. Also, the overall slope of the integrator section seems to be steeper in the measured values. This is interesting since with Bode's relations magnitude and phase are tightly connected and the absolute values of the phase agree rather well. Probably the actual implementation of the filter stages is not exactly described by equation (4.23), but filters with steeper slopes are employed. Another point of disagreement is in the behaviour at very high frequencies. Above around 10 MHz, the overall low-pass behaviour of the FALC due to its limited bandwidth manifests itself in reduced gain and quickly dropping phase, which is not captured here.

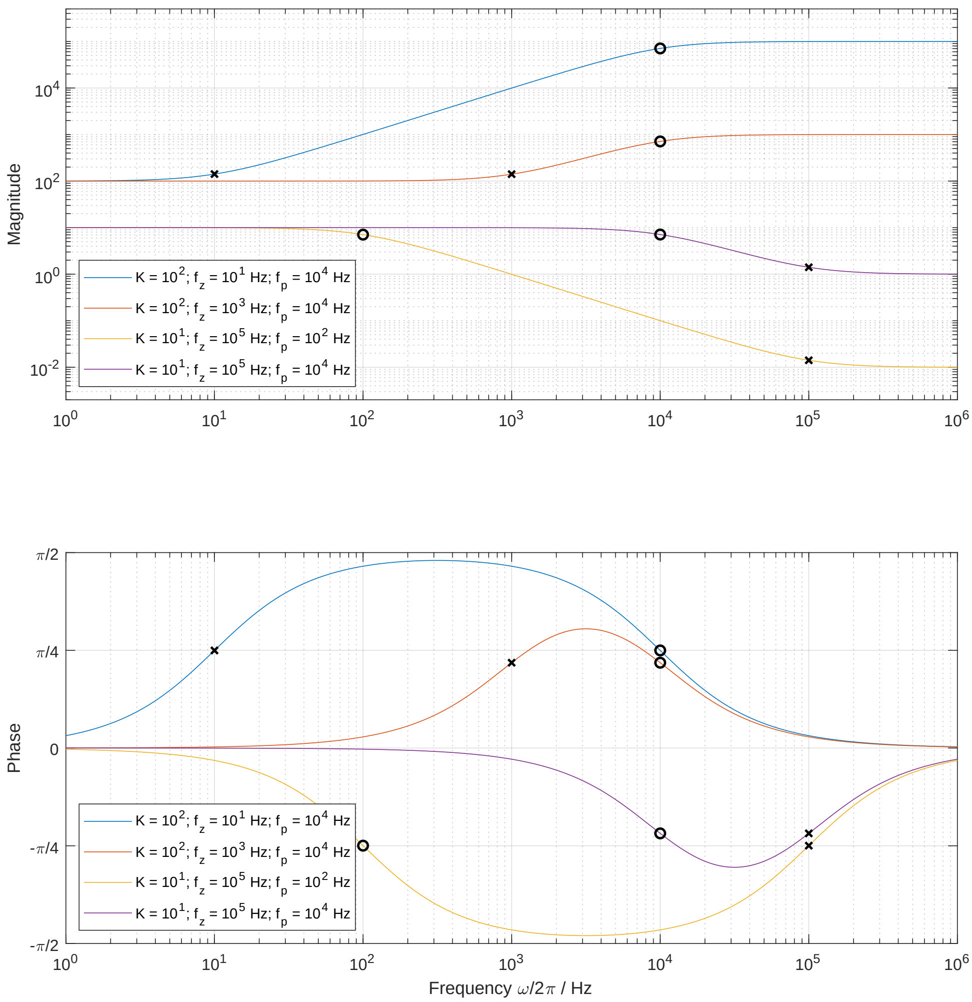

Figure 4.4: Bode plot of equation (4.23) for different values of K, f_z and f_p. The respective f_z are marked with crosses, the f_p with open circles. K determines the gain at zero frequency. If $f_\mathrm{z} < f_\mathrm{p}$, the stage acts as differentiator between these frequencies and leads to phase lead, if $f_\mathrm{z} > f_\mathrm{p}$, it acts as integrator and leads to phase lag.

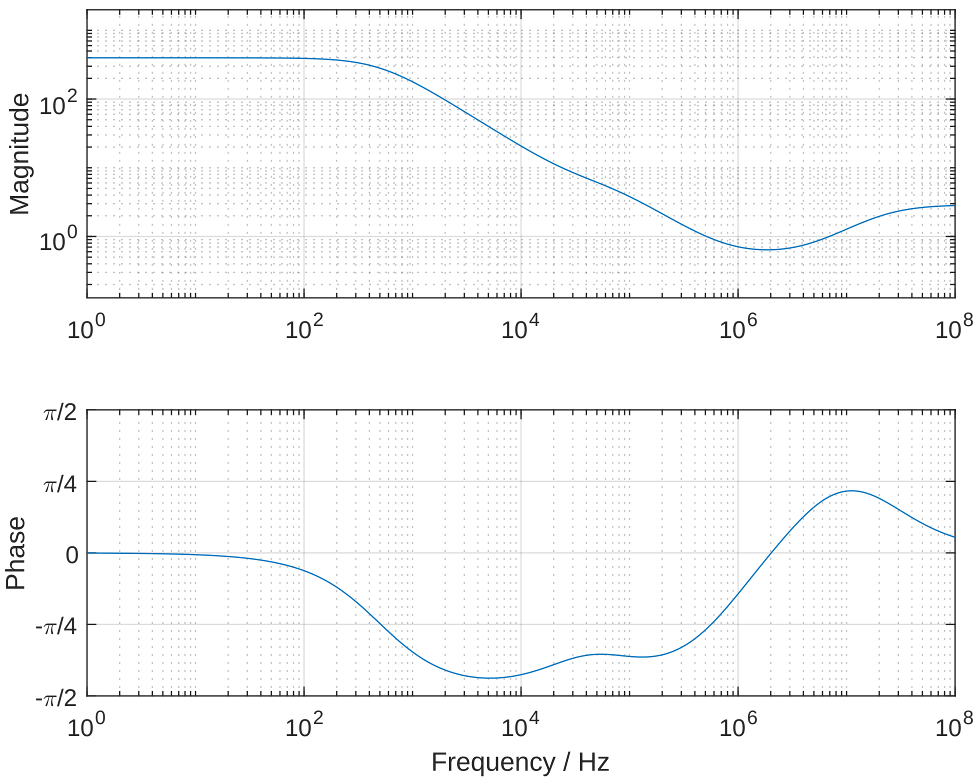

Figure 4.5: Bode plot of overall transfer function of FALC, based on stages like equation (4.23), with example corner frequencies according to the FALC manual. The corner frequencies of each stage are given in the text. The absolute gain values are not to scale, but the general shape agrees with the measured network analysis provided in the FALC manual. Only at very high frequencies close to 100 MHz, the FALC exhibits stronger low-pass behaviour, which is not captured here.

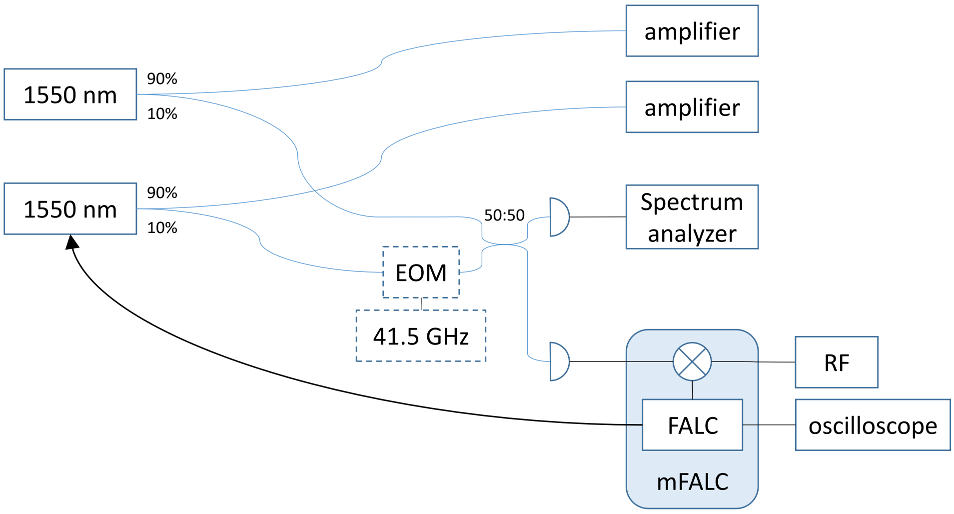

Figure 4.6: Fiber optical setup for the heterodyne optical phase-locked loop between the two 1550 nm Raman seed lasers. Blue connections denote optical fibers, black connections represent electrical cables. The optical fiber length from laser head to photodiode is around 3.6 m, which limits the loop performance. Additional optical and electrical attenuators were included to prevent damaging or saturation of subsequent components, but are omitted for clarity. The dashes components indicate where the EOM for sideband generation would enter in the future.

In the transfer function, one can nicely identify the effect of the FLD, which is to provide a phase lead at higher frequencies. By shifting its frequency range, one can optimize it to lie around the phase reversal of the open loop transfer function L, in order to increase the loop bandwidth a little bit more. In addition, the FALC offers a setting for extra FLD gain, which was also used in this work.

The circuit described so far was one section of the FALC, which is used for fast feedback to modulate the injection current of the slave SCL. The other section of the FALC is called the unlimited integrator (ULI) and is used for slower feedback. It is connected to the piezo voltage-controlled cavity mirror of the slave laser, which, although slow, provides a larger frequency tuning range than the injection current. This is used to compensate for long-term drifts and to keep the slave laser frequency within the hold-in range of the fast feedback loop.

4.4 Experimental realization and results

4.4.1 First fiber-optical setup

The employed laser heads as well as the laser amplifiers for the Raman setup are based on fiber-optical inputs and outputs. Thus for the long term, all optical components of the OPLL should be fiber-based as well and it was first set up like this. Figure 4.6 is a scheme of the actual setup to implement the heterodyne OPLL. For initial testing, the objective was to lock both lasers to the same frequency, without the additional EOM to create sidebands. Of both Toptica DL Pro seed lasers, the main portion of the power is fed into the Keopsys laser amplifiers. Only 10 % each is split off using a fiber tap and then combined with a balanced fiber coupler. Both outputs of the coupler are led onto fast fiber-coupled photodiodes (Thorlabs FPD610-FC-NIR, DC - 600 MHz). Optical attenuators (not shown) were added in order to keep the incident power in a range where the photodiodes do not show saturation behaviour. The output of one photodiode is used for out-of-loop monitoring of the beat note signal on a spectrum analyzer (RIGOL DSA815), whereas the photocurrent of the other one is fed into the the Toptica mFALC 110. The RF offset signal is generated by an Aim-TTi TGR1 040 RF signal generator, the initial frequency of 50 MHz was later increased to 150 MHz. An oscilloscope (Tektronix TBS1000B) can be used to monitor either the error signal, or the injection current modulation which is fed back into one of the seed lasers. The injection current was attenuated slightly in order to prevent any possible damage of the laser diode.

The light travels around 4 meters through the fiber splitters and combiners, since fibers with standard lengths were used. The electrical path length was reduced to about 0.3 meters. For reference, 4 meters of fibers corresponds to 20 ns time delay. If all components in the loop exhibited perfectly linear response, so phase lag resulted only from this time delay and of course the integration term, the frequency of phase reversal would be at 12 MHz. However experimentally, with these parameters and an RF offset frequency of 50 MHz, the servo bumps were observed at around 1.8 MHz. The optimal FALC settings to achieve this value were FLD setting 5 and all integrator stages left off, also the input gain was left minimal. In general, higher main gain pushed the servo bumps further out until at some point the loop becomes unstable. The estimates of the loop bandwidth are given for high main gain values where the servo bumps appear pronounced. The loop bandwidth could be increased to around 2.1 MHz by switching the FLD gain to maximal. A test with 6 meters additional cable length lead to a decrease in loop bandwidth to about 1.5 MHz, indicating that the phase margin at these frequencies is small enough for delay to become noticeable. This suggests that a decrease in signal path length might increase the loop bandwidth. In hindsight, the fact that the phase margin at lower frequencies is too small to allow for additional phase lag is supported by another observation: Switching on any of the integrator stages drastically reduced the loop bandwidth or even made the whole loop unstable.

4.4.2 Free space test setup

In order to test the possible improvement with a shortened optical path length, a layout where the beam propagates in free space instead of through optical fibers was set up. For this, a 50:50 beam splitter replaced the fiber coupler. The free space path length could thus be reduced to about 40 cm, adding to the 35 cm of the fiber photodiode. This lead to a loop performing with a bandwidth of about 2.5 MHz, achieved with similar settings as in the fiber-based setup. However, increasing the RF offset frequency to 150 MHz further enhanced the loop bandwidth to around 2.7 MHz. This might me due to a lower contribution of pink noise, or another component in the laboratory produces disturbance at this frequency. Further increasing the RF offset to 300 MHz did not yield an additional improvement.

Figure 4.7 shows the beat note between both lasers in the locked state for low and high gain values. In both cases, the central peak is very sharp, which indicates the phase-stability of one laser with respect to the other. For low gain, the servo bumps are flat and broad, while for high gain they become stronger and more pronounced. Also, the distance of the servo bump to the center peak increases, i.e. the loop bandwidth increases. For comparison to the unlocked case, figure 4.9 shows the beat note between seed lasers when both are free-running. The linewidth is specified to be at least 10 kHz. In addition, the frequency of the beat note is free to drift.

The central peak is shown in more detail in figure 4.8. Although the resolution is limited by the resolution bandwidth (RBW) of the electrical spectrum analyzer, one can estimate the half

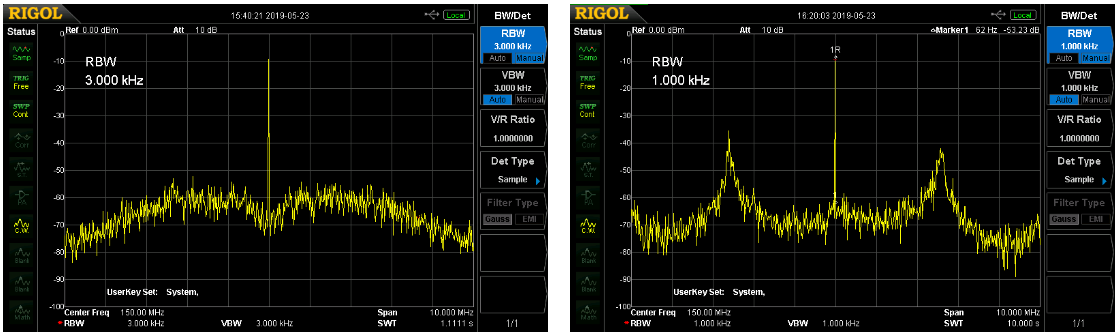

(a) Low gain

(b) High gain

Figure 4.7: Beat note between both seed lasers when one is locked to the other via the free space test setup. a) Main gain set to a low value, the servo bumps are flat and broad. b) Main gain set to a high value, which increases the one-sided loop bandwidth to about 2.7 MHz. Also, the servo bumps become much more pronounced. The central peak is shown in more detail in figure 4.8.

width at half max to be about 8 Hz. The small bump 50 Hz above the main signal might be caused by the alternating current of the mains electricity. The peak is not exactly at 150 MHz as set by the RF source, but about 60 Hz below. This might be due to inaccuracy of the electrical spectrum analyzer or of the RF source, since neither of them is synchronized to a reference clock.

4.5 Influence of servo bumps in the experiment

We have seen in chapter 3 that the feedback mechanism of the phase-locked loop creates unwanted spectral features near the loop bandwidth due to the amplification of disturbances and noise. From the results of the previous section we know that for our system, the loop bandwidth is a few MHz. However, typical motional frequencies of trapped ions are in the same range, which can cause problems in the experiment. To discuss how these problems arise, the interaction of the ion's internal state with its motional state via an external electrical field is briefly introduced. For a more detailed discussion, the reader is referred to Haroche and Raimond [60] or Wineland *et al.* [30].

4.5.1 Coupling of ion internal and motional state

For trapped ion quantum information processing, the internal state of a single trapped ion is simplified to a 2-level structure acting as qubit with the Hamiltonian

$$\hat{H}_{\mathrm{a}} = \frac{\hbar\omega_{\mathrm{a}}}{2}\sigma_z, \tag{4.24}$$

where $\omega_{\mathrm{a}}/2\pi$ is the frequency of the atomic transition under consideration, and σ_z is the Pauli spin matrix. The ion's motion along one of the trap axes, which we set to be the z axis, is treated as mode of an harmonic oscillator, for which the Hamiltonian is given by

$$\hat{H}_{\mathrm{m}} = \hbar\omega_z \hat{a}^\dagger \hat{a}, \tag{4.25}$$

where $\omega_z/2\pi$ is the frequency of the oscillator mode, also called motional frequency or trap frequency. $\hat{a}^\dagger$ and $\hat{a}$ are the respective creation and annihilation operators. The interaction

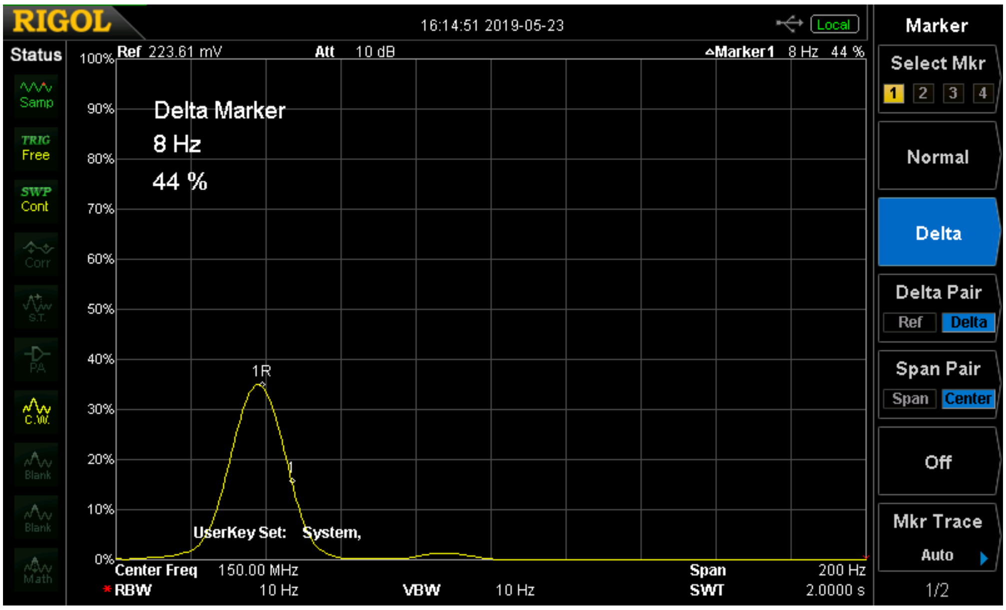

Figure 4.8: Close-up spectrum of the central peak of the locked beat note for low gain, the shape stays similar for high gain. The half width at half maximum (HWHM) is about 8 Hz, the resolution is limited the by the resolution bandwidth (RBW) of the electrical spectrum analyzer.

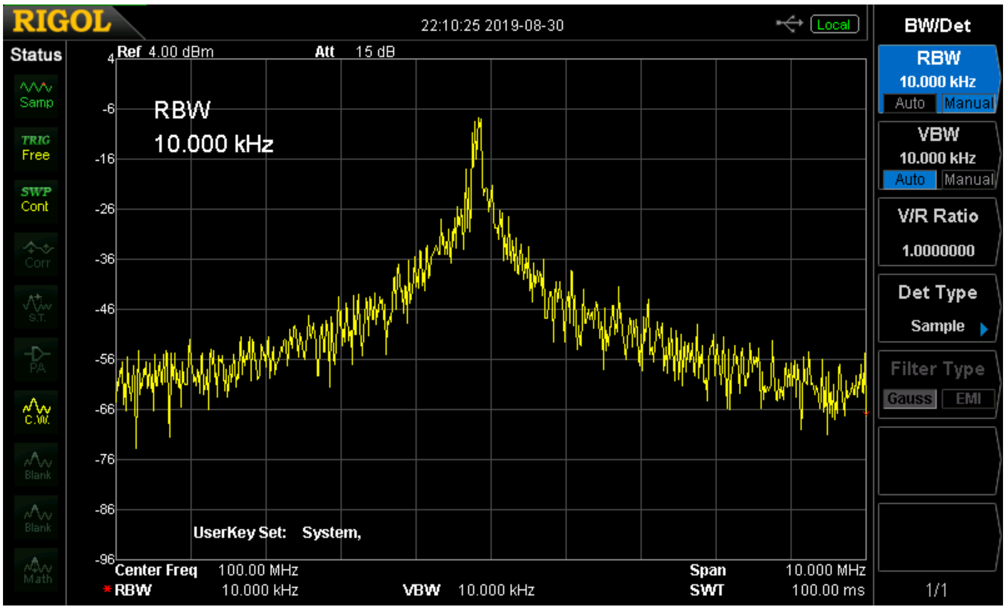

Figure 4.9: Beat note between both free-running seed lasers. The linewidth of each laser is specified to be above 10 kHz.

between both the qubit state and the harmonic oscillator can be mediated by an external electric field. For a monochromatic laser field in the coherent state $|\alpha\rangle$, the interaction Hamiltonian in the dipole approximation is then given by

$$\hat{H}_1 = -i\frac{\hbar\Omega_0}{2}\mathrm{e}^{i\boldsymbol{k}\cdot\hat{\boldsymbol{R}}}\mathrm{e}^{-i(\omega_{\mathrm{L}}t+\phi)}\sigma_+ + \mathrm{h.c.} \tag{4.26}$$

Here, $\Omega_0 = -\frac{2\boldsymbol{d}\boldsymbol{E}_0}{\hbar}$ is the vacuum Rabi frequency with $\boldsymbol{d} = q\langle e|\hat{\boldsymbol{r}}|g\rangle$ being the transition dipole element of the qubit, and $\boldsymbol{E}_0$ the electric field vector amplitude. $\boldsymbol{k}$ is the wave vector of the laser field and $\boldsymbol{k}\cdot\hat{\boldsymbol{R}} = \eta(\hat{a}+\hat{a}^\dagger)$ where we have defined the Lamb-Dicke parameter $\eta = k\sqrt{\frac{\hbar}{2m\omega_z}}\cos\theta$ with m being the mass of the ion and θ the angle between $\boldsymbol{k}$ and the trap axis. $\omega_{\mathrm{L}}/2\pi$ and ϕ are the frequency and phase of the laser field and σ_+ is the qubit raising operator.

Usually in trapped ion experiments, the condition $\eta \ll 1$ is fulfilled and the interaction is said to be in the Lamb-Dicke regime. Then, the first exponent in equation (4.26) can be expanded in a power series. Keeping only the terms up to first order and going to the interaction picture with respect to $\hat{H}_0 = \hat{H}_{\mathrm{a}} + \hat{H}_{\mathrm{m}}$ yields

$$\hat{H}_{\mathrm{I}} = -i\frac{\hbar\Omega_0}{2}\mathrm{e}^{-i(\omega_{\mathrm{L}}t+\phi)}\sigma_+\mathrm{e}^{i\omega_{\mathrm{a}}t}\left(1 + i\eta\hat{a}\mathrm{e}^{-i\omega_z t} + i\eta\hat{a}^\dagger\mathrm{e}^{i\omega_z t}\right) + \mathrm{h.c.} \tag{4.27}$$

Now we can do the rotating wave approximation and neglect off-resonant terms. Depending on the laser frequency, three major cases can be distinguished:

- For $\omega_{\mathrm{L}} = \omega_{\mathrm{a}}$:
$$\hat{H}_{\mathrm{I,carrier}} = -i\frac{\hbar\Omega_0}{2}\left(\sigma_+\mathrm{e}^{-i\phi} - \sigma_-\mathrm{e}^{i\phi}\right). \tag{4.28}$$
This corresponds to a carrier transition, so on the Bloch sphere, the evolution under this Hamiltonian corresponds to a rotation around an axis with azimuthal angle ϕ by the angle $\Omega_0 t$. The motion of the ion is not affected.

- For $\omega_{\mathrm{L}} = \omega_{\mathrm{a}} - \omega_z$:
$$\hat{H}_{\mathrm{I,RSB}} = \frac{\hbar\Omega_0\eta}{2}\left(\hat{a}\sigma_+\mathrm{e}^{-i\phi} + \hat{a}^\dagger\sigma_-\mathrm{e}^{i\phi}\right). \tag{4.29}$$
RSB stands for red-sideband, which comes from the fact that the laser is red-detuned with respect to the atomic transition. Due to the lower frequency of the laser field, the energy difference between a photon of the laser field and the qubit excited state is made up for by one quantum of the ion's motion. This means if one photon of the laser field is absorbed, also one motional quantum has to be removed in order to excite the qubit. Similarly, when the qubit emits one photon into the laser field, also one quantum is added to the ion motion. This means the number of excitations in the qubit and the motion is conserved. For a laser phase of $\phi = 0$, this Hamiltonian equals the Jaynes-Cummings Hamiltonian of cavity quantum electrodynamics [60]. The effective Rabi frequency of this process is reduced to $\Omega_0\eta$.

- For $\omega_{\mathrm{L}} = \omega_{\mathrm{a}} + \omega_z$:
$$\hat{H}_{\mathrm{I,BSB}} = \frac{\hbar\Omega_0\eta}{2}\left(\hat{a}^\dagger\sigma_+\mathrm{e}^{-i\phi} + \hat{a}\sigma_-\mathrm{e}^{i\phi}\right). \tag{4.30}$$
Similarly, this is the blue-sideband Hamiltonian. Now for each absorbed photon, one motional quantum is added instead of removed. For each emitted photon, one motional quantum is also removed. In reference to the red-sideband Hamiltonian, $\hat{H}_{\mathrm{I,BSB}}$ is also called the anti-Jaynes-Cummings Hamiltonian.

For stimulated Raman transitions, the corresponding Hamiltonians are very similar and are obtained by the substitutions $\omega_{\mathrm{L}} \to \delta\omega = \omega_1 - \omega_2$, $\boldsymbol{k} \to \Delta\boldsymbol{k} = \boldsymbol{k}_1 - \boldsymbol{k}_2$ and $\phi \to \phi_1 - \phi_2$ [30].

The red- and blue-sideband Hamiltonians are important in quantum information processing with trapped ions, since they are a means to transfer information from one qubit to another via the ions' collective motion. So in order to create entangled states between multiple qubits, sideband transitions have to be involved [6, 7]. In the following it is discussed how servo bumps can cause errors in an experiment involving sideband transitions.

4.5.2 Error during sideband transitions

Coming back to the phase-locked lasers, imagine that the frequency distance between the central peak of the locked laser and the servo bump is similar to the motional frequency of the ion ω_z. Then, the servo bumps appear as features in the laser spectrum which may be resonant with a transition that is different from the one which is driven by the central peak. For example, if $\omega_{\mathrm{L}} = \omega_{\mathrm{a}}$, then the servo bumps are located at the frequencies $\omega_{\mathrm{a}} \pm \omega_z$. This means that they would drive the red- and blue-sideband transitions unwantedly, and thus introduce errors to the experiment. This case is not of main concern, since in addition to the reduced power in the servo bumps compared to the central peak, the rate of sideband transitions is reduced by a factor of $\eta \ll 1$ compared to the carrier transition. However, the case becomes worse when $\omega_{\mathrm{L}} = \omega_{\mathrm{a}} \pm \omega_z$, which is the case when we want to drive a sideband transition. Then, one of the servo bumps would be located at ω_{a}, and would drive the carrier transition with an increased rate over the sideband transition. This situation can become an issue in every experiment involving sideband transitions, and so should be avoided. A simplified mathematical treatment of the error probability in this case was prepared in the group [61], and is presented in the following subsubsection. Subsubsection 4.5.2.2 then presents the results of the error estimation based on the beat note spectra obtained in this work.

4.5.2.1 Carrier transition probability

This theoretical treatment of the error introduced by a servo bump during a sideband transition follows an internal document by J. Home [61].

The potential error which we consider here occurs during a sideband transition, which is described by either equation (4.29) or (4.30). The servo bump, however, is at a frequency which corresponds to the carrier transition. Due to the reduced optical power in the servo bump compared to the central peak, we introduce a new Hamiltonian similar to the carrier Hamiltonian, but with a rate reduced by a factor $\epsilon(t)$:

$$\hat{H}_{\text{carrier}}^{(\text{servo bump})} = \hbar\epsilon(t)\Omega_0\left(\sigma_+ + \sigma_-\right), \tag{4.31}$$

where the laser phase has been set to $\phi = -\frac{\pi}{2}$ for simplicity. Note that this Hamiltonian is now in the Schrödinger picture and $\epsilon(t)$ carries the time-dependence of the electric field. From perturbation theory, the transition amplitude from an initial state $|\psi_i\rangle$ to a final state $|\psi_f\rangle$, both being eigenstates of the bare atomic Hamiltonian H_{a}, is given by:

$$\mathcal{S}_{fi} = \delta_{fi} + \frac{1}{i\hbar}\int_{t_i}^{t_f} \mathrm{d}t' V_{fi} \mathrm{e}^{\frac{i}{\hbar}(E_f - E_i)t'}, \tag{4.32}$$

where δ_{fi} is the Dirac delta function, $E_{i/f}$ are the eigenenergies of $\left|\psi_{i/f}\right\rangle$ and $V_{fi} = \langle\psi_f|V|\psi_i\rangle$ is the corresponding transition matrix element of the interaction part of the Hamiltonian [62]. In our case, $V = \hat{H}_{\text{carrier}}^{(\text{servo bump})}$, $|\psi_i\rangle = |0\rangle$ and $|\psi_f\rangle = |1\rangle$. We also set $t_i = 0$ and $t_f = T_\pi$, which is the effective pulse time for the sideband transition which is driven by the main peak. Then, the transition probability after time T_π is

$$\mathcal{P}_{fi}(T_\pi) = |\mathcal{S}_{fi}|^2 \tag{4.33}$$

$$= \left| -i \int_0^{T_\pi} \mathrm{d}t' \epsilon(t') \Omega_0 \langle 1|(\sigma_+ + \sigma_-)|0\rangle \, \mathrm{e}^{i\omega_\mathrm{a} t'} \right|^2 , \tag{4.34}$$

with $\omega_\mathrm{a} = \frac{E_1 - E_0}{\hbar}$. Expanding the magnitude squared, using $\sigma_+ = |1\rangle\langle 0|$ and $\sigma_- = |0\rangle\langle 1|$, and assuming Ω_0 and $\epsilon(t)$ are real yields

$$\mathcal{P}_{fi}(T_\pi) = \Omega_0^2 \int_0^{T_\pi} \mathrm{d}t' \epsilon(t') \mathrm{e}^{-i\omega_\mathrm{a} t'} \int_0^{T_\pi} \mathrm{d}t'' \epsilon(t'') \mathrm{e}^{i\omega_\mathrm{a} t''} \tag{4.35}$$

$$= \Omega_0^2 \int_0^{T_\pi} \mathrm{d}t' \int_0^{T_\pi} \mathrm{d}\tau \epsilon(t') \epsilon(t' - \tau) \mathrm{e}^{-i\omega_\mathrm{a} \tau}, \tag{4.36}$$

where $\tau = t' - t''$ was introduced in the second line. Assuming that $\epsilon(t)$ is a stationary process and using the autocorrelation function for times T much larger than the correlation time τ_c of $\epsilon(t)$

$$\langle \epsilon(t)\epsilon(t+\tau)\rangle = \frac{1}{T} \int_0^T \mathrm{d}t \epsilon(t)\epsilon(t+\tau), \tag{4.37}$$

the transition probability can be written as

$$\mathcal{P}_{fi}(T_\pi) = \Omega_0^2 T_\pi \int_0^{T_\pi} \mathrm{d}\tau \, \langle \epsilon(t)\epsilon(t+\tau)\rangle \, \mathrm{e}^{-i\omega_\mathrm{a}\tau}. \tag{4.38}$$

Here, we can recognize the finite Fourier transform of the autocorrelation function at the frequency ω_a. The Wiener-Khinchin theorem relates this Fourier transform to the power spectral density of $\epsilon(t)$, $S_\epsilon(\omega)$ [50]:

$$S_\epsilon(\omega) = \int_{-\infty}^{\infty} \mathrm{d}\tau \, \langle \epsilon(t)\epsilon(t+\tau)\rangle \, \mathrm{e}^{-i\omega\tau}. \tag{4.39}$$

Since $T_\pi \gg \tau_c$, the limits of integration in equation (4.38) can formally be extended to infinity and we write

$$\mathcal{P}_{fi}(T_\pi) = \Omega_0^2 T_\pi S_\epsilon(\omega_\mathrm{a}), \tag{4.40}$$

giving us an expression for the transition probability of the carrier transition dependent on the power spectral density of the servo bump.

To obtain an analytic expression for the power spectral density of the servo bump, we can assume the autocorrelation function to have a specific form. Here we take it to feature an exponential decay with τ:

$$\langle \epsilon(t)\epsilon(t+\tau)\rangle = \epsilon_0^2 \mathrm{e}^{-\Gamma_\mathrm{SB}|\tau|} \mathrm{e}^{-i\omega_\mathrm{SB}\tau}, \tag{4.41}$$

where Γ_SB is the decay constant, and $\omega_\mathrm{SB}/2\pi$ is the frequency of the servo bump. Fourier transformation of this autocorrelation function according to equation (4.39) yields the power spectral density of the servo bump:

$$S_\epsilon(\omega) = \epsilon_0^2 \frac{2\Gamma_\mathrm{SB}}{\delta^2 + \Gamma_\mathrm{SB}^2}, \tag{4.42}$$

where $\delta = \omega - \omega_{\mathrm{SB}}$ is the detuning from the servo bump. This form of the power spectral density is a Lorentzian with half width at half maximum (HWHM) of Γ_{SB}. Inserting into equation (4.40) yields:

$$\mathcal{P}_{fi}(T_\pi) = \Omega_0^2 T_\pi \epsilon_0^2 \frac{2\Gamma_{\mathrm{SB}}}{\delta_{\mathrm{a}}^2 + \Gamma_{\mathrm{SB}}^2}, \tag{4.43}$$

where $\delta_{\mathrm{a}} = \omega_{\mathrm{a}} - \omega_{\mathrm{SB}}$.

In this result, we can relate Ω_0 to the time T_π it takes for the π-pulse on the sideband transition. The evolution $\mathrm{e}^{-\frac{i}{\hbar}\hbar\eta\Omega_0(\sigma_+ a + \sigma_- a^\dagger)T}$ under for example the red sideband Hamiltonian for the time T corresponds to a rotation $e^{i\frac{\theta}{2}\sigma_x}$ in the qubit subspace, so the angle $\frac{\theta}{2}$ corresponds to $\eta\Omega_0 T$. In our case where $\theta = \pi$ it then follows that $\Omega_0 = \frac{\pi}{2\eta T_\pi}$ and we finally obtain

$$\mathcal{P}_{fi}(T_\pi) = \left(\frac{\pi\epsilon_0}{2\eta}\right)^2 \frac{1}{T_\pi} \frac{2\Gamma_{\mathrm{SB}}}{\delta_{\mathrm{a}}^2 + \Gamma_{\mathrm{SB}}^2}. \tag{4.44}$$

This result allows to estimate the probability of a carrier transition induced by a servo bump, viewed as error during a sideband transition. From a servo bump spectrum, normalized to the power in the main peak, the parameters ϵ_0, ω_{SB} and Γ_{SB} can be obtained. η and T_π are dependent on the experimental settings for which the error shall be estimated. In the following, such an estimation is presented for typical parameters.

4.5.2.2 Estimation based on beat note spectra

In this work, the power spectral density of the servo bumps can be inferred from the beat note spectra recorded with an electrical spectrum analyzer (cf. section 4.4). In the following, the procedure and results of the estimation based on these spectra is described.

First of all, one should note the ambiguity of using the term *power* in this context, since both electrical and optical power could be referred to. It is important to differentiate the two: the voltage of the measured signal of the spectrum analyzer is originating from the photodiode and is thus proportional to optical power. However, the voltage as an electrical signal also generates a power, the electrical power which scales as $P = \frac{V^2}{R}$, with V being the voltage and R the resistance. In this subsubsection, the term *power* refers to the electrical power, unless stated otherwise. Also the symbol P is reserved for electrical power, whereas V is used for the voltage representing the optical power.

The data which was recorded in units of Volts was converted to dBm according to

$$P^{(\mathrm{dBm})} = 10\log_{10}\left[\frac{\frac{V^2}{R}}{10^{-3}\ \mathrm{W}}\right], \tag{4.45}$$

where $R = 50\ \Omega$ is the resistance of the spectrum analyzer and W stands for the unit Watt. Then, the recorded data was subjected to some corrections and conversions:

- The internal attenuation of the spectrum analyzer reduced the recorded amplitude compared to the actual signal. Thus the corresponding number of decibels was added to $P^{(\mathrm{dBm})}$.
- $10\log_{10}$ of the resolution bandwidth (RBW) of the spectrum analyzer was subtracted from the power in dBm in order to obtain the electrical power spectral density in dBm $PSD^{(\mathrm{dBm})}$.
- Due to the ratio of equivalent noise bandwidth to the -3 dB RBW, a constant of $10\log_{10}(1.056) = 0.24$ dB was subtracted [63].

Finally, the power spectral density in dBm was converted back to volts using

$$VSD = \sqrt{R \times 10^{-3}\ \mathrm{W} \times 10^{PSD^{(\mathrm{dBm})}/10}}, \tag{4.46}$$

where VSD stands for voltage spectral density.

Now we need to find how the voltage spectral density relates to the optical power spectral density of the servo bump. As mentioned before, the voltage is proportional to the optical power, which in turn is just the optical intensity integrated over the detector area. From the interference equation (equation (4.3) in section 4.1), it becomes clear that the intensity of the component at the beat note frequency scales with the electric field amplitudes of both lasers $|E_{\mathrm{M}}E_{\mathrm{S}}|$. Also, the effective Rabi frequency of the Raman transition scales as follows: $\Omega_{\mathrm{eff}} \propto \frac{\Omega_{\mathrm{M}}\Omega_{\mathrm{S}}}{\Delta}$, where $\Omega_{\mathrm{M/S}} \propto |E_{\mathrm{M/S}}|$. This means that the voltage from the photodiode is proportional to the effective Rabi frequency. To obtain the ratio ϵ_0 of Rabi frequencies from the main peak and the servo bump, one thus has to compare the integrated voltage spectral densities at those frequencies. This can be accomplished by fitting the servo bump with a Lorentzian and obtaining the area analytically. However, this fit would not yield the correct width Γ_{SB} to use in equation (4.44), since there the optical power spectral density of the servo bump was considered, which is proportional to the square of the electric field of the servo bump. Thus, we fit the voltage spectral density at the servo bump as obtained from equation (4.46) with the square root of a Lorentzian

$$\sqrt{A\frac{2\Gamma}{\delta^2+\Gamma^2}} \tag{4.47}$$

to obtain the fitted parameters A_{SB}, Γ_{SB} and ω_{SB}. Similar fitting of the central peak of the beat note yields A_{C}, Γ_{C} and ω_{C}, where C stands for central. The area under a Lorentzian curve $A\frac{2\Gamma}{\delta^2+\Gamma^2}$ is $2A$, so the normalization factor of the optical power in the servo bump ϵ_0 is obtained by $\epsilon_0 = \sqrt{A_{\mathrm{SB}}/A_{\mathrm{C}}}$.

Figures 4.10a and 4.10b show the beat note spectra at the servo bump and at the central peak, for a medium loop filter gain setting. The servo bump spectrum was obtained by averaging over 100 single sweeps. The yellow lines indicate the fits according to equation (4.47). Neither the servo bump, nor the central peak match their fitted profile well, but the fit allows to extract the order of magnitude of the parameters ϵ_0^2 and Γ_{SB} to perform an error estimation according to the theory introduced in subsubsection 4.5.2.1.

Figure 4.11 shows the error probability due to carrier excitation by the servo bump during a sideband transition, plotted versus detuning δ_{a} of the carrier transition from the servo bump. The probability was calculated according to equation (4.44), with parameters ϵ_0^2 and Γ_{SB} obtained from the fits in figures 4.10a and 4.10b. $\eta = 0.1$ and $T_\pi = 30$ µs were chosen to represent typical experimental conditions. A maximum error probability of 82% indicates that a servo bump directly at the carrier transition during a sideband transition is not tolerable in an experiment. Detuning of the servo bump 2 MHz away from the carrier transition improves the error probability down to the few percent level. However, as the servo bump does not match the Lorentzian profile well, the dropoff should be treated with special care.

For a Lamb-Dicke parameter of $\eta = 0.2$, the error probability is reduced to one quarter of the value for $\eta = 0.1$. The error is also reduced by a less pronounced servo bump, which is the result of a lower main gain of the loop filter. Fitting of such low gain spectra yields reduced error probabilities of 14% and 4% for $\eta = 0.1$ and 0.2, respectively. An overview over the resulting error probabilities for these different gain settings and η values is given in table 4.1. Only $\eta = 0.2$ together with far detuning of the servo bump from the carrier frequency yields error probabilities in the range below 10^{-2}. Because in our case, the trap frequency ω_z was not fixed yet, the loop

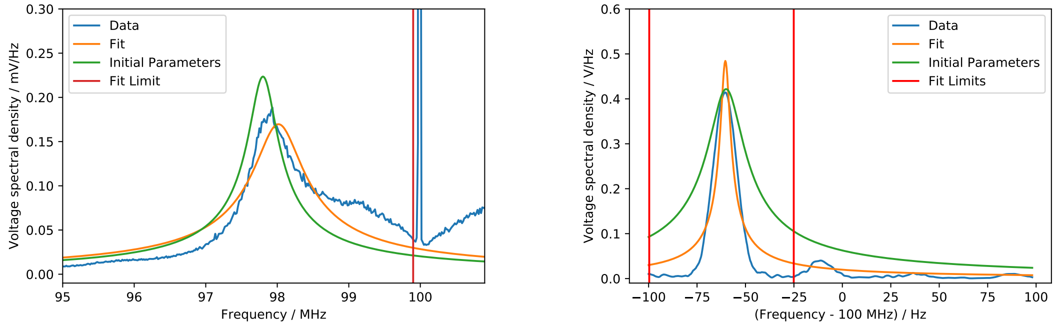

(a) (b)

Figure 4.10: Fits of the voltage spectral density of the servo bump (a) and the central peak (b) according to equation (4.47). The beat note spectrum of the servo bump was obtained by 100 times averaging. The main gain setting of the FALC was at a medium value. From the obtained fitting parameters, the error probability during a sideband transition is calculated using equation (4.44) and is plotted in figure 4.11 for some typical experimental parameters.

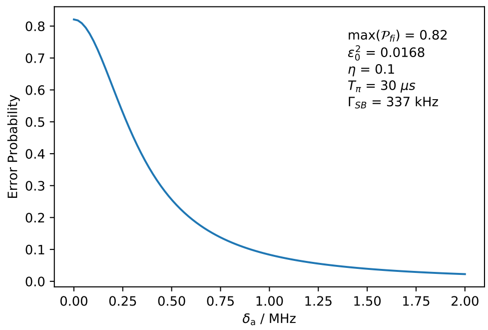

Figure 4.11: Error probability during a sideband transition as calculated with equation (4.44), plotted as function of detuning δ_a of the carrier frequency from the servo bump. The parameters ϵ_0^2 and Γ_SB were obtained from fits to the spectra presented in figures 4.10a and 4.10b. $\eta = 0.1$ and $T_\pi = 30$ µs were chosen as typical experimental parameters.

η	0.1		0.2	
main gain	medium	low	medium	low
$\mathcal{P}_{fi}$ @ $\delta_\mathrm{a} = 0$ MHz	0.82	0.14	0.21	0.04
$\mathcal{P}_{fi}$ @ $\delta_\mathrm{a} = 2$ MHz	0.02	0.12	0.006	0.03

Table 4.1: Error probabilities $\mathcal{P}_{fi}$ according to equation (4.44) for different η and control filter main gain settings. $T_\pi = 30$ µs; ϵ_0 and Γ_SB were obtained by fits of the beat note spectra (cf. figures 4.10a and 4.10b).

bandwidth was increased as much as possible in order to create the greatest leeway in influencing the position and amplitude of the servo bumps, away from the motional frequency of the ion.

All in all, the error probabilities due to a servo bump at or near the carrier transition frequency can be high enough to be relevant for almost all quantum information processing experiments. Especially the tuning of loop filter main gain allows for a certain adaption of the position and power in the servo bumps. Depending on the specific experimental implementation with its combination of trap frequency and Lamb-Dicke parameter, the resulting achievable error probabilities may be sufficient for high-fidelity sideband transitions. If they are not, additions to the OPLL scheme like an additional external phase-shifter (cf. subsubsection 2.3.2.1) or even different approaches like optical injection locking (cf. subsubsection 2.3.2.2) may need to be employed as alternatives to the work in this thesis.

Chapter 5

Sum-frequency generation in periodically-poled $LiNbO_3$

As second part of this work, two beamlines of 626 nm sum-frequency generation (SFG) were set up. In the overview over the laser setup for the Penning experiment (cf. figure 2.2 in chapter 2), the two respective stages are marked. The first one is part of the beamline for the cooling and detection beam, the second is part of one of the Raman beamlines. In the following, the theory behind sum-frequency generation (SFG) and its conversion efficiency is touched upon (section 5.1). Section 5.2 then describes how the SFG setup was planned and set up. In section 5.3, the resulting performance of one SFG stage is presented. Seeding both SFG stages from phase-locked lasers, the beat note is observed at 626 nm, which is described in section 5.4.

5.1 Nonlinear optics

In a homogeneous, isotropic, non-magnetic dielectric medium, the wave equation derived from Maxwell's equations takes the form [50]

$$\nabla^2 \boldsymbol{\mathcal{E}} - \frac{1}{c_0^2}\frac{\partial^2 \boldsymbol{\mathcal{E}}}{\partial t^2} = \mu_0 \frac{\partial^2 \boldsymbol{\mathcal{P}}}{\partial t^2}, \tag{5.1}$$

with the electric field $\boldsymbol{\mathcal{E}}$, the vacuum speed of light c_0, the vacuum permeability μ_0 and the polarization density $\boldsymbol{\mathcal{P}}$. Vector quantities are in bold print. For linear media, $\boldsymbol{\mathcal{P}}$ and $\boldsymbol{\mathcal{E}}$ are then related by $\boldsymbol{\mathcal{P}} = \epsilon_0 \chi \boldsymbol{\mathcal{E}}$, where ϵ_0 is the vacuum permittivity and χ is the electric susceptibility. A nonlinear medium is defined as one where the relation between $\boldsymbol{\mathcal{P}}$ and $\boldsymbol{\mathcal{E}}$ does not take this simple form, but exhibits nonlinearity. It can then be written in general form as $\boldsymbol{\mathcal{P}} = \Psi(\boldsymbol{\mathcal{E}})$.

Even with focused laser beams, these externally applied electrical fields are usually weak compared to their interatomic counterparts, so one can expand $\Psi(\boldsymbol{\mathcal{E}})$ to

$$\mathcal{P} = \epsilon_0 \chi \mathcal{E} + \epsilon_0 \chi^{(2)} \mathcal{E}^2 + \epsilon_0 \chi^{(3)} \mathcal{E}^3 + ..., \tag{5.2}$$

where the nonlinear optical coefficients $\chi^{(2)}$ (often denoted as d) and $\chi^{(3)}$ describe the second- and third-order nonlinear effects. Note that $\mathcal{P}$ and $\mathcal{E}$ here aren't vector quantities anymore, but the individual vector components which can be treated separately since the medium is assumed to be isotropic, i.e. $\boldsymbol{\mathcal{P}}$ is always parallel to $\boldsymbol{\mathcal{E}}$.

5.1.1 Second-order nonlinear optics

If a material is non-centrosymmetric, $\chi^{(2)}$ is non-zero and second-order nonlinear processes such as sum-frequency generation can occur. For an incident electric field of the form $\mathcal{E}(t) = \text{Re}\left\{E_1 \mathrm{e}^{i\omega_1 t} + E_2 \mathrm{e}^{i\omega_2 t}\right\}$, the nonlinear part of the polarization density for the second-order nonlinearity is given by

$$
\begin{aligned}
\mathcal{P}_{\text{NL}}^{(2)} &= \epsilon_0 \chi^{(2)} \mathcal{E}^2 && (5.3)\\
&= \frac{\epsilon_0 \chi^{(2)}}{2} E_1^2 + E_2^2 && (5.4)\\
&+ \frac{\epsilon_0 \chi^{(2)}}{2} \left(\cos\left[2\omega_1 t\right] + E_2^2 \cos\left[2\omega_2 t\right]\right) && (5.5)\\
&+ \epsilon_0 \chi^{(2)} E_1 E_2 \cos\left[(\omega_1 + \omega_2)t\right] && (5.6)\\
&+ \epsilon_0 \chi^{(2)} E_1 E_2 \cos\left[(\omega_1 - \omega_2)t\right]. && (5.7)
\end{aligned}
$$

Equation (5.4) describes the effect of optical rectification, equation (5.5) yields second-harmonic generation, and the terms (5.6) and (5.7) describe sum- and difference-frequency generation, respectively. Here we concern ourselves with the former, which describes the creation of one photon at the sum frequency from two photons at angular frequencies ω_1 and ω_2:

$$\omega_1 + \omega_2 = \omega_3, \tag{5.8}$$

obeying energy conservation. However, not all photons of the starting frequencies are converted, and also the other mentioned terms act as competitive processes. Which of these dominates, is greatly determined by the phase-matching condition:

$$\boldsymbol{k}_1 + \boldsymbol{k}_2 = \boldsymbol{k}_3, \tag{5.9}$$

where $|\boldsymbol{k}_i| = \frac{2\pi}{\lambda_i}$ are the wave vectors of the corresponding electric fields at wavelengths λ_i. If this condition is fulfilled, it ensures that photons created at different times in different locations of the nonlinear medium are in-phase. This means they add up constructively to give a macroscopic electric field amplitude at this frequency. For processes for which the phase-matching condition is not fulfilled, the newly created microscopic electrical fields at different locations are in random phase relation to each other and thus cancel each other out.

For optimal beam overlap, the wave vectors are collinear. In order to fulfil the phase-matching condition, the refractive index of the nonlinear medium then has to take the same value for all three optical frequencies involved. However, this is in general not possible due to dispersion. Thus one defines the wave vector mismatch, or phase mismatch

$$\Delta k' = k_3 - (k_1 + k_2), \tag{5.10}$$

now written in scalar form since the wave vectors are assumed to be collinear. Usually, $\Delta k'$ is written without the prime, but we include it here to differentiate it from its counterpart in quasi-phase-matching. From the phase mismatch, the coherence length is defined as

$$L_\text{c} = \frac{\pi}{\Delta k'}, \tag{5.11}$$

i.e. the length in the crystal over which a photon at ω_3 has assumed a phase difference of π compared to a newly created photon at the final location. This means photons created at a distance L_c apart cancel each other out by destructive interference.

5.1.2 Quasi-phase-matching

As an alternative to birefringent phase-matching, which is very wavelength-sensitive, one method to overcome the issue of wave vector mismatch is to use quasi-phase-matching [64]. In this experiment, we employ periodically-poled Lithium niobate (PPLN) to achieve quasi-phase-matching. As its name suggests, the crystal exhibits a sequence of regions along the optical axis which vary periodically in their direction of the permanent electric dipole moment. If the direction of the electric dipole moment is swapped, $\chi^{(2)}$ changes its sign, or equivalently the phase of $\mathcal{P}$ is shifted by π. Now if the poling period is matched to be an integer multiple of the coherence length L_c, what would have been destructive interference is turned into constructive interference, thus correcting the phase-mismatch. This allows for buildup of optical power over a longer distance, even if the phase-matching condition is not perfectly matched. We thus adjust the phase-matching condition to account for quasi-phase-matching and write

$$\Delta k = k_3 - (k_1 + k_2) - K_m. \tag{5.12}$$

Here, we introduced the grating wave vector of the mth-harmonic

$$K_m = \frac{2\pi m}{\Lambda}, \tag{5.13}$$

where Λ is the poling period of the crystal. Thus the effect of periodic poling is to shift the actual wave vector mismatch $\Delta k'$ by an amount K_m to yield an effective or total wave vector mismatch of Δk, which then determines the conversion efficiency. The dependency of the output power at the sum frequency ω_3 on the effective wave vector mismatch and the crystal length L is given by the following factor [64]:

$$P_{\omega_3} \propto \mathrm{sinc}^2\left(\frac{\Delta k L}{2}\right), \tag{5.14}$$

where $\mathrm{sinc}(x) = \frac{\sin(x)}{x}$. This factor can be tuned by the temperature of the crystal, which influences both Δk and L:

$$\frac{\partial}{\partial T}(\Delta k L) = L\frac{\partial \Delta k'}{\partial T} + \alpha \Delta k' L, \tag{5.15}$$

where $\alpha = \frac{1}{L}\frac{\partial L}{\partial T}$ is the coefficient of linear thermal expansion for the crystal material [64]. The change of temperature influences the crystal length and poling period due to thermal expansion, but also the refractive index might vary slightly which affects the wave vector mismatch. PPLN crystals are typically operated in an oven at temperatures above 100 °C in order to prevent damage from photorefractive effects. Using the temperature control then also allows to precisely adjust the product $\Delta k L$ in order to maximize the output power for the given set of wavelengths.

5.1.3 Conversion efficiency

We describe the conversion efficiency of the SFG process in terms of output power per input power product per crystal length:

$$\Gamma_{\mathrm{SFG}} = \frac{P_{\omega_3}}{P_{\omega_1} P_{\omega_2} L}. \tag{5.16}$$

Boyd and Kleinman [65] theoretically describe the shape that the incoming electrical fields should have in order to maximize the conversion efficiency in second-harmonic generation or sum-frequency generation. For maximal overlap, both input beams should be collinear perfect Gaussian beams, and the focus of both should coincide and be centered in the crystal along the optical axis. Instead of the minimum possible value, the optimal waist size is given in relation to the crystal length L and the wavelength in the crystal. More specifically, they derive an optimal value for the focusing parameter

$$\xi = \frac{L}{2z_\mathrm{R}}. \tag{5.17}$$

Here, z_R is the Rayleigh range of a Gaussian beam with waist radius W_0, given by

$$z_\mathrm{R} = \frac{\pi W_0^2}{\lambda}. \tag{5.18}$$

For the case of no double refraction, Boyd and Kleinman find that $\xi_\mathrm{optim}^{(\mathrm{BK})} = 2.84$.

The process of interest for us is $\omega_{1050} + \omega_{1550} = \omega_{626}$. For this however, Lo *et al.* [29] find an optimal waist radius which corresponds to a lower focusing parameter, namely $\xi_\mathrm{optim}^{(\mathrm{Lo})} = 1.3$. They ascribe this to possible imperfections in mode overlap, caused by absorption-induced heating. In comparison to other publications using the same crystal for this process [28, 66], their result boasts the highest conversion efficiency, which indicates that the theoretical prediction by Boyd and Kleinman should rather be used as guideline with room for empirical corrections. As will be described in subsection 5.2.2, we indeed aimed for the focusing parameter found by Lo *et al.* instead of the one by Boyd and Kleinman.

5.2 SFG setup

From the optimum focusing parameter, we know the waist radii W_0 of the Gaussian beams that we want to achieve in the middle of the crystal. In order to plan how to focus the beam in this way, the beams coming from the amplifier outcoupler first had to be characterized, which is described in subsection 5.2.1. Then the beam propagation through a pair of lenses, which we call telescope, can be simulated (subsection 5.2.2) and the beamline can be set up accordingly (subsection 5.2.3).

5.2.1 Beam profile measurements

Before all beam measurements, the amplifiers were left running for at least 30 minutes at the final power setting in order to warm up and stabilize the output power and beam shape. The amplifiers for 1050 nm (Keopsys CYFA-PB) were set by current, while the 1550 nm amplifiers (Keopsys CEFA-C-PB) allowed setting the output power directly. The minimum output power of the amplifiers is greater than 0.5 W, so for all alignment and measurement purposes, the majority of the power was split off and dumped using a half-wave plate (HWP) and polarizing beam splitter (PBS). The resulting beam carried down to about 1 % of the initial power.

A beam profiler (Thorlabs BC106N-VIS/M) was available for 1050 nm, which allowed simple measurements of the waist sizes of those lasers. For 1550 nm, other methods had to be employed, which make use of the fact that the transverse intensity profile of a Gaussian beam is of Gaussian shape, as the name suggests:

$$I(x, y, z) = I_0 \frac{W_0^2}{W^2(z)} \exp\left[-\frac{2((x - x_0)^2 + (y - y_0)^2)}{W^2(z)}\right], \tag{5.19}$$

where I_0 is a constant, z is the coordinate along the optical axis, x_0 and y_0 are the coordinates of maximum intensity in the transverse plane and W_0 is the waist radius at the focus [50]. The

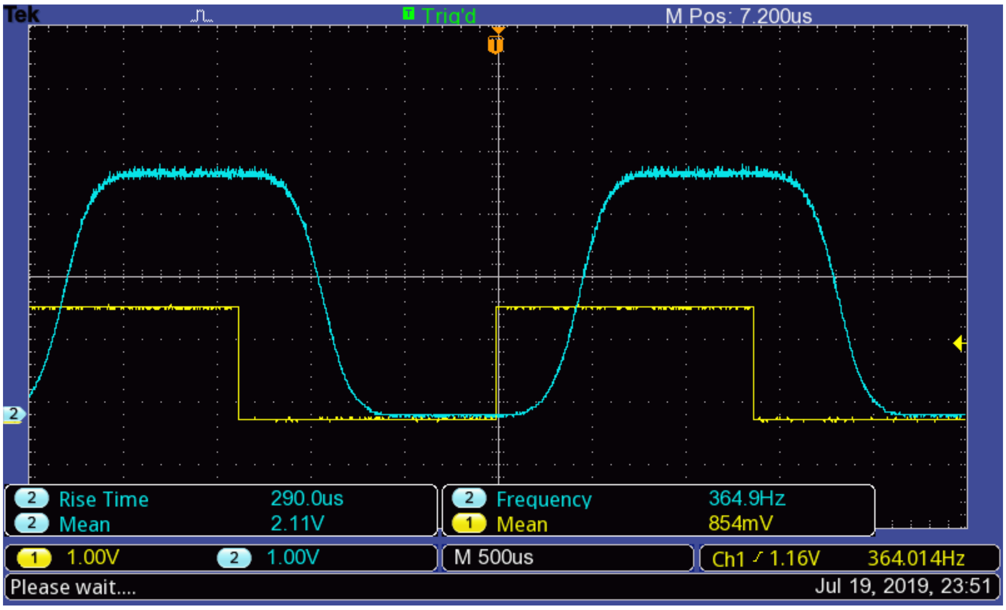

Figure 5.1: Yellow: Trigger. Blue: Oscilloscope trace of the photodiode signal of a laser beam which is being chopped with a chopper wheel. From the falling edge, the width of the beam in chopping direction can be inferred by fitting equation (5.21).

waist radius at a position z is given by

$$W(z) = W_0\sqrt{1+\left(\frac{z-z_0}{z_R}\right)^2}, \tag{5.20}$$

where z_0 is the position of the focus along the optical axis. Note that the Rayleigh range, which we denote here as z_R, is in the literature sometimes called z_0. The waist radius is the radial distance from the beam center at which the intensity has dropped to $\frac{1}{e^2}$ of its maximum value. To estimate it, one can block part of the beam along one of the transverse directions by a knife-edge, whose position is given by (x, z). Then, the measured power is the integral over the remaining non-obstructed area of the beam:

$$\begin{aligned} P(x,z) &= \sqrt{\frac{2}{\pi}} I_0 \frac{W_0^2}{W^2(z)} \int_x^\infty \mathrm{d}x' \exp\left[-\frac{2(x'-x_0)^2}{W^2(z)}\right] \\ &= \frac{2}{\pi} I_0 W_0^2 \operatorname{erfc}\left[-\frac{\sqrt{2}(x-x_0)}{W(z)}\right], \end{aligned} \tag{5.21}$$

where erfc is the complementary error function. Taking data at various positions x for fixed z allows the extraction of the waist radius $W(z)$ at position z by fitting equation (5.21).

As first attempt, this procedure was performed with a knife-edge mounted on a translation stage. However, the taken data was not suitable for analysis because the measured beam power exhibited significant fluctuations during the data-taking. This was because small relative fluctuations in transmission through the PBS resulted in large absolute fluctuations for the weak output beam.

As an alternative, a chopper wheel was placed in the beam path and the photodiode signal was observed on an oscilloscope. Figure 5.1 shows the oscilloscope trace of one of the 1550 nm beams (blue), as well as the trigger signal from the chopper wheel controller (yellow). The falling edges of the trace take the form of the error function like in equation (5.21), except for the fact that the trace is a function of time and not position. Thus, one has to convert the time axis into an axis describing the position of the chopping edge. This can be achieved using its linear velocity v_{edge}. However, the velocity of the chopping edge is not easily measured directly. Instead, the chopping frequency f_{chop} is held constant by the controller, for which we chose the value of 364 Hz. Dividing by the number of chopping blades n_{blades} yields the rotation frequency of a single blade $f_{\mathrm{rot}} = \frac{f_{\mathrm{chop}}}{n_{\mathrm{blades}}}$. Since the angular velocity is $\omega_{\mathrm{rot}} = 2\pi f_{\mathrm{rot}}$, the linear velocity can be calculated using the radius of the center of the beam from the center of the chopper wheel R:

$$v_{\mathrm{edge}} = \omega_{\mathrm{rot}} R. \tag{5.22}$$

The measurement of this radius was the main source of error, with an inaccuracy of ± 1 mm. The position of the chopping edge as function of time is thus given by

$$x - x_0 = 2\pi \frac{f_{\mathrm{chop}}}{n_{\mathrm{blades}}} R(t - t_0). \tag{5.23}$$

t_0 is now the time when the chopping edge passes the center of the beam, corresponding to the point of steepest slope of the oscilloscope trace. Inserting equation (5.23) into equation (5.21) now allows to fit the oscilloscope traces and thus obtain $W(z)$. Figure 5.2 shows the data of such an oscilloscope trace and its fit.

A simpler way to obtain a value for the beam width is to connect it to the 10% to 90% rise time Δt_{rise}, which can already be pre-calculated and displayed on the oscilloscope. Then, $W(z)$ is given by [67]

$$W(z) = 0.7809\ \omega_{\mathrm{rot}} R \Delta t_{\mathrm{rise}}. \tag{5.24}$$

Note that such a measurement gives the waist radius of the Gaussian beam only along one of the transverse axes. To measure along the other axis, the chopper wheel had to be placed perpendicular to its initial orientation. A perfect Gaussian beam is cylindrical, but for the laser beams in our setup, the waist radii measured along the different transverse axes were not always equal, indicating ellipticity. Another caveat that one should have in mind when performing such a beam width measurement, is that the axis along which the chopping edge travels through the beam is generally not one of the major axes of the beam ellipse. If the measurement axes were tilted with respect to the major axes by 45°, then the results would point to a perfectly cylindrical shape, even though this is not the case. Thus the measurement with a chopper wheel can only ever underestimate the ellipticity of the beam. If a beam is elliptical, this also means that its focii do not have to coincide along the optical axis. For our purposes, the ellipticities of the beams were small enough that we decided to neglect them.

Once the waist radii for different z are known, one can assess whether the beam is collimated or diverges. For our purpose, we call a beam collimated if its waist size stays similar over the length of the optical table. If it changes, we call the beam diverging. This is also indicates by the Rayleigh length, which is the distance from the focus at which the waist radius has increase by a factor of $\sqrt{2}$. The 1550 nm beams were found to have similar beam widths for distances from the fiber outcoupler from 20 to 90 cm, so they are properly collimated. As examples, $W(z)$ values from 2.4 to 2.9 mm were found for the different amplifiers for different orientations, corresponding to Rayleigh ranges of several meters.

The waists of the 1050 nm beams however were found to diverge, corresponding to Rayleigh ranges of only ~10 cm. Figure 5.3 shows the data taken in the horizontal direction for the

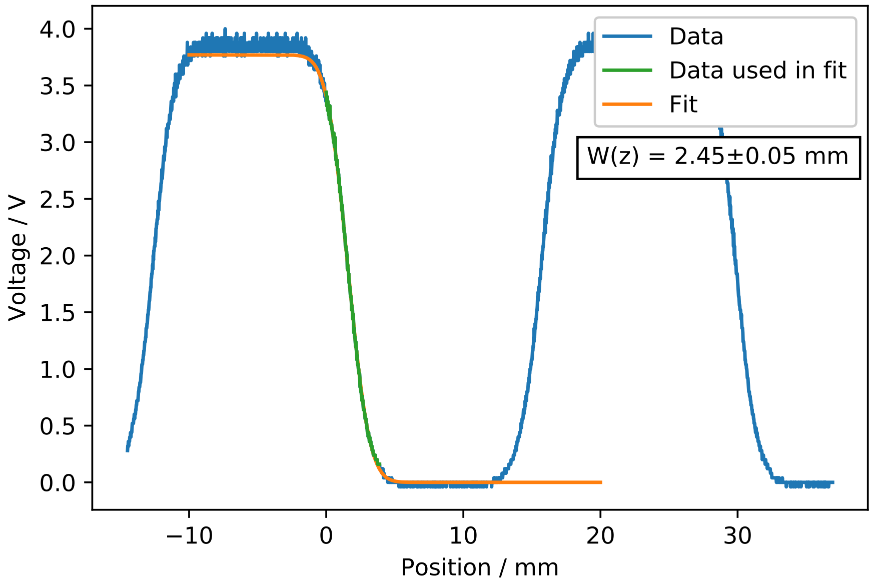

Figure 5.2: Fit of oscilloscope trace according to equation (5.21) to obtain the beam waist $W(z) = 2.45 \pm 0.05$ mm. The error bar is determined by the uncertainty of measuring R. The time axis was converted to position of the chopping edge using equation (5.23).

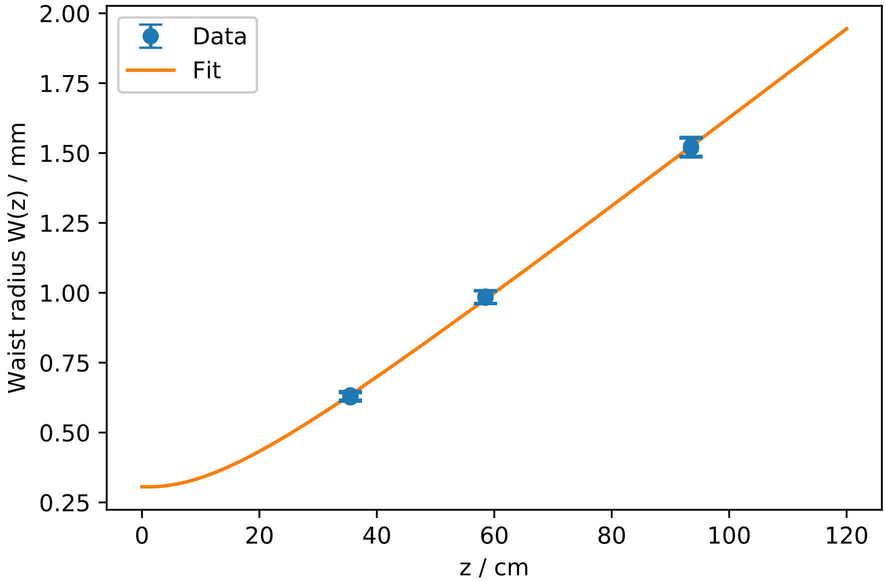

Figure 5.3: Measured waist radii of the 1050 nm beam for the Raman beamlines in the horizontal direction. At each distance z, multiple data points were taken. The error bars are determined by the inaccuracy in measuring R. The diverging beam was fit according to equation (5.20).

1050 nm amplifier of the Raman beamline. The data points were fit with equation (5.20), using equation (5.18) for z_R. This yields the waist radius at the focus W_0 and the position of the focus z_0. The focii were found to be roughly at the position of the outcoupler, the waist radii at the focus were 0.31(1) mm for the Raman 1050 nm beam in both directions, and 0.128(3) mm (0.166(4) mm) for the repumping and cooling/detection 1050 nm beam in horizontal (vertical) direction. The value in parentheses is one standard deviation. With these values, the Gaussian beam is fully characterized, and its propagation through an optical system can be simulated, which is described in the following subsection.

5.2.2 Gaussian beam propagation

A Gaussian beam is fully characterized by its direction of propagation, which we choose to be along the z-axis, the position of its waist z_0 along this optical axis and two more parameters. These can be any two of its wavelength λ, the Rayleigh range z_R, the waist radius at the focus W_0, the waist radius at position z, $W(z)$, or the radius of curvature at position z, $R(z)$, which can be calculated interchangeably using equations (5.18), (5.20) or

$$R(z) = z\left(1 + \left(\frac{z_\mathrm{R}}{z - z_0}\right)^2\right). \tag{5.25}$$

Once a Gaussian beam is fully characterized, one can calculate its propagation through a system of optical components. As mentioned before, we set the z axis to be the optical axis. In addition, the origin is set to the focus of the Gaussian beam, so $x_0 = y_0 = z_0 = 0$. If we know the wavelength λ, then the beam at position z is fully characterized by the complex beam parameter, or q-parameter:

$$q = z + iz_\mathrm{R}. \tag{5.26}$$

By propagation through an optical component which does not change λ, the resulting beam can be described by an 'output' q-parameter $q' = z' + iz'_\mathrm{R}$. It is very important to note that z' is now referenced to a different origin, which is now the new position of the focus if it has been changed by the optical component. So the real part of the q-parameter always gives the position relative to the Gaussian beams' focus, irrespective of the position in the laboratory coordinate system at which q describes the beam.

The output q' is related to the 'input' q by

$$q' = \frac{aq + b}{cq + d}. \tag{5.27}$$

a, b, c and d are constants determined by the optical system which the beam propagates through. They are the components of the so-called ABCD-matrix $\underline{\mathrm{M}}$ of the respective system:

$$\underline{\mathrm{M}} = \begin{bmatrix} a & b \\ c & d \end{bmatrix}, \tag{5.28}$$

which is usually known from the propagation in terms of ray optics [50]. Here we denote matrices with an underbar. The ABCD-matrices for some general optical components are the following:

- Propagation over a distance d:

$$\underline{\mathrm{M}}_d^{(\mathrm{prop})} = \begin{bmatrix} 1 & d \\ 0 & 1 \end{bmatrix}. \tag{5.29}$$

- Propagation through a thin lens with focal length f:

$$\underline{\mathrm{M}}_{f}^{(\mathrm{tl})} = \begin{bmatrix} 1 & 0 \\ -\frac{1}{f} & 1 \end{bmatrix}, \tag{5.30}$$

  where $f > 0$ means the lens is convex, whereas it is concave for $f < 0$.

- Refraction at an interface between materials with refractive indices n_1 and n_2:

$$\underline{\mathrm{M}}_{n_1,n_2}^{(\mathrm{refr})} = \begin{bmatrix} 1 & 0 \\ 0 & \frac{n_1}{n_2} \end{bmatrix}. \tag{5.31}$$

- Propagation through a larger system of N components is then described by a single matrix which is the product of the ABCD-matrices of each individual component:

$$\underline{\mathrm{M}}^{(1,2\ldots N)} = \underline{\mathrm{M}}^{(N)} \cdots \underline{\mathrm{M}}^{(2)} \underline{\mathrm{M}}^{(1)}. \tag{5.32}$$

Accordingly, the propagation through a telescope like the one used in this experiment, i.e. two thin lenses separated by air, is given by

$$\underline{\mathrm{M}}_{f_1,f_2,d_1,d_2,d_3}^{(\mathrm{a})} = \underline{\mathrm{M}}_{d_3}^{(\mathrm{prop})} \underline{\mathrm{M}}_{f_2}^{(\mathrm{tl})} \underline{\mathrm{M}}_{d_2}^{(\mathrm{prop})} \underline{\mathrm{M}}_{f_1}^{(\mathrm{tl})} \underline{\mathrm{M}}_{d_1}^{(\mathrm{prop})}, \tag{5.33}$$

where d_1 is the distance before the first lens (focal length f_1), d_2 is the distance between the two lenses, and d_3 is the distance after the second lens (focal length f_2). For convenience, we call this system (a).

System (b) is then propagation through the same telescope, but appended with refraction into a different material, which for us is the PPLN crystal, and propagation over the distance d_4 within that material:

$$\underline{\mathrm{M}}_{f_1,f_2,d_1,d_2,d_3,d_4,n_1,n_2}^{(\mathrm{b})} = \underline{\mathrm{M}}_{d_4}^{(\mathrm{prop})} \underline{\mathrm{M}}_{n_1,n_2}^{(\mathrm{refr})} \underline{\mathrm{M}}_{d_3}^{(\mathrm{prop})} \underline{\mathrm{M}}_{f_2}^{(\mathrm{tl})} \underline{\mathrm{M}}_{d_2}^{(\mathrm{prop})} \underline{\mathrm{M}}_{f_1}^{(\mathrm{tl})} \underline{\mathrm{M}}_{d_1}^{(\mathrm{prop})}. \tag{5.34}$$

We can thus simulate which combination of parameters d_i and f_i leads to the desired waits size in the crystal, optimizing the focusing parameter ξ (cf. section 5.1). Using the same parameters for system (a), we can find at which distance from the second lens the focus will be in free space, i.e. before the crystal is put into place. This prediction can then be used to set up the beam line in this optimal way. Simulating until the free space focus in addition to the focus in the crystal is necessary because they are not at the exact same location. This means inserting the crystal into the beam path shifts the focus by a non-negligible amount, which has to be taken into account when placing the crystal so that the focus is centered along its length. Note that the waist radius stays the same, irrespective of the medium's refractive index.

Figure 5.4 shows the propagation of the 1050 nm Raman beam through systems (a) and (b), simulated with Wolfram Mathematica. The parameters are chosen in order to yield an optimal focusing parameter in the nonlinear crystal, which for a 4 cm crystal length corresponds to a waist radius of 47 µm. The beam diverges already from the outcoupler to the first lens. The first lens has a focal length of $f_1 = -100$ mm, expanding the beam even further. The second lens has focal length of $f_2 = 100$ mm, focusing the beam to the optimal waist after around 20 cm. With the crystal placed such that the focus is centered along the crystal length, the focus is located about 1 cm further away from the second lens than the free-space focus. This particular choice of lenses was made for several reasons: Focal lengths should be a least 75 mm in order to reduce aberrations. Also, they should be available as stock items. The increased focal lengths had two other advantages: The effective focal length of the telescope arrangement was large enough to

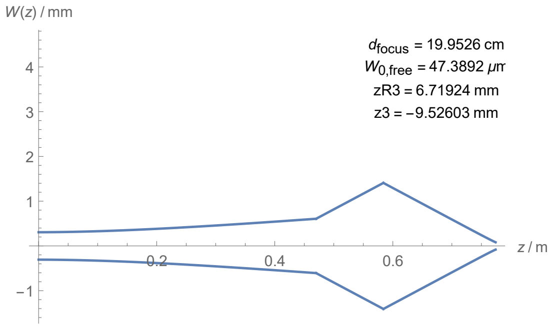

(a)

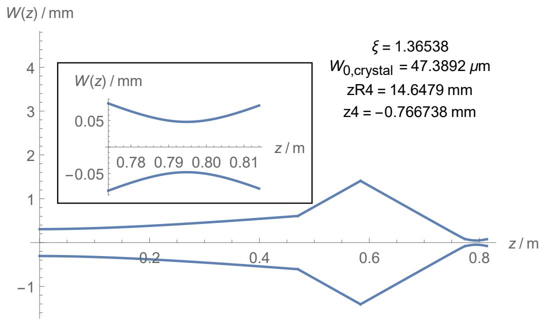

(b)

Figure 5.4: Propagation of the Gaussian beam from the outcoupler of the 1050 Raman amplifier through the two lenses of the telescope. a) Propagation in free space with corresponding output parameters. b) Propagation through free space into the crystal. The focus in the crystal (see inset) has the same waist radius as the free space focus, but it is shifted by about 1 cm.

allow a geometrically convenient beam layout, and the sensitivity of the focal spot size to the distance between telescope lenses was reduced, allowing for easier optimization.

Similar simulations were performed for the other beams involved in the two SFG beamlines. For the 1550 nm telescopes, lenses with the same focal lengths were chosen, which focus the beam down to a target waist size of 58 µm after a distance of about 40 cm. Having this estimated optimal lens placement, in principle the setup can be built accordingly. In practice however, this was an iterative process of laying out the components such that the focii are in the same location, measuring the distances between components and recalculating the parameters until a satisfying layout was found. Especially for the diverging 1050 nm beams, the distance from outcoupler to the first lens has an influence onto the beam waist even when the distance between lenses remained fixed.

5.2.3 Set up procedure

In the following, the procedure of setting up one SFG beamline is described in detail. For reference, figure 5.5 shows the final setup of the Raman SFG beamline.

As mentioned before, setting up was performed with laser beams where the majority of the power was split off and dumped with a HWP and a PBS, so that the power was reduced for alignment. Also, the mirrors were set up first whereas the telescopes were put into place later. The beam path for one of the two beams was set up first. Knowing where the telescope will be placed then fixes the position of the focus. The second beam path is then set up in order to allow the second telescope on its 3-axis translation stage (OptoSigma TSD-403) to be placed in such way that the second focus in the same position as the focus of the first beam. For the telescopes, enough space is left to be able to correct for small deviations from the simulation results. With the mirrors in place and the telescope placement planned, the exact distances between components were measured again and the beam propagation re-simulated. In case a different placement was necessary, the previous steps were repeated iteratively until both focii can in principle be set to the same position with the correct spot size. Once every component except the telescopes was in place, both beams were walked in order to overlap them after a dichroic mirror. First, this was performed by eye using fluorescence cards. While doing this, care was taken to keep the beams close to the center of the mirrors. Precise overlapping was

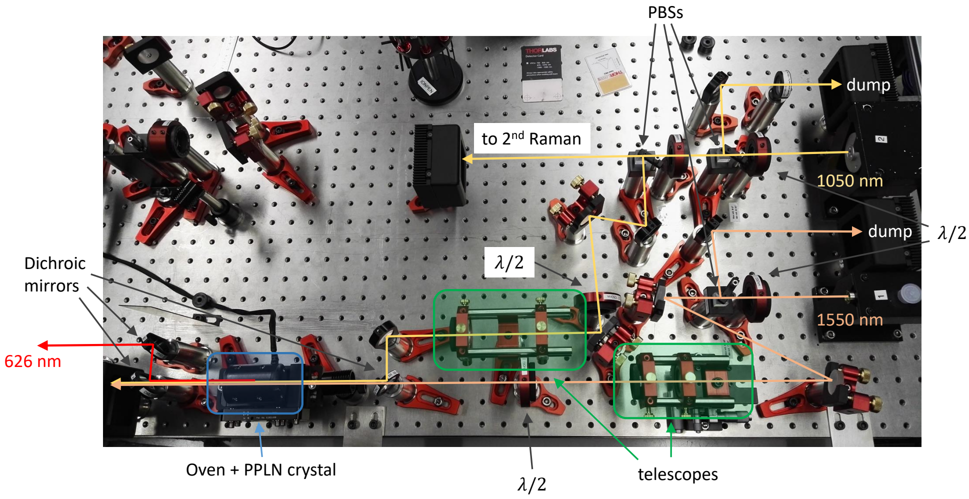

Figure 5.5: Picture of the experimental setup for one of the Raman SFG stages. Polarizing beam splitters (PBSs) allow for controlling the power that is sent through the setup, even with fixed amplifier gain. Telescopes focus the beam to the desired waist size in the non-linear crystal. The crystal is heated by an oven with small entry and exit slits. Dichroic mirrors are used to overlap both IR beams, and after the crystal to separate 626 nm light from the unconverted IR light.

performed with a chopper wheel: Using dichroic mirrors, both beams were focused onto separate photodiodes, whose outputs were monitored on different channels of an oscilloscope. A chopper wheel in the beam path then produces rising/falling edge signals as in figure 5.1, for both channels. In these signals, the relative position of the beam centers in the chopping plane corresponds to relative timing of the rising/falling edge signals. Thus, both beams are overlapped when the turning points of the rising or falling edges of both channels coincide. Vertical and horizontal alignment was adjusted in positions close to and far from the beam-combining dichroic mirror iteratively, until no temporal shift of the rising and falling edges was visible anymore.

When the beams were optimally overlapped, the first telescope was put into its place. Care was taken to let the beams pass through the lens centers in order to avoid aberrations. This was optimized by overlapping both beams again, this time using only the telescope's lens adjustment screws. The second telescope was then placed in the same way. Also, in each beam path a HWP was placed to allow for optimization of the electric field polarization at the nonlinear crystal.

Using the chopper wheel again, the positions of both focii were found by searching for the fastest rise time of each signal. The previous simulation of the Gaussian beam propagation ensured that both were positioned close enough to each other to perform adjustments by shifting the telescopes without the need to re-build the complete beam path. The waist radii were estimated with the rise time method (cf. equation (5.24)) and the distances between the lenses in both telescopes were adjusted until the desired waist size was achieved. This also required slight adjustment of the telescope position with its translation stage, since the distance between both telescope lenses influences the telescope's effective focal length.

With both beams overlapped, the focii in the same position and having the desired waist radii, the crystal oven (Covesion PV40) was put into position. The crystal (Covesion MSFG626-0.5-40) was put into place, accounting for the shift of focal position by refraction at the crystal interface (cf. subsection 5.2.2). After the crystal, two dichroic mirrors which reflect only 626 nm light were placed in order to separate the light at the sum-frequency from the unconverted IR light. At first, the crystal oven was kept open, and very low optical power was shone onto the crystal. Using an IR viewer which is sensitive to 1050 nm light (Electrophysics ElectroViewer 7215) and a 5-axis translation stage (New Focus 9081), the crystal was positioned such that the focused beams pass through one of the crystal lanes properly. The different lanes of the PPLN crystal exhibit slightly different poling periods, which then require different crystal temperatures for quasi-phase-matching (cf. subsection 5.1.2). The oven was now closed, the crystal heated to this optimum temperature (oven controller Covesion OC2) and the optical power increased for both beams to about 1 W. When the crystal lane was found properly, some red light was now visible after the two dichroic mirrors. The red light at 626 nm was measured with a power meter, which allowed for optimization of the conversion efficiency.

Optimization of the conversion efficiency is described in the following. Since one beam is used as reference beam, its degrees of freedom were not optimized. Instead, the 5 axes of the crystal translation stage, the 3 axes of the telescope translation stage of the beam which is not used as reference, the lens adjustment screws of said telescope and the mirrors in this beam path were used as one set of degrees of freedom to optimize. This set was optimized alternatingly with the crystal temperature, whose optimum changes with different alignment. After several rounds of optimization, the change in output power with further rounds became small enough that this optimization was stopped. For the cooling/detection beamline, the distance between the lenses in the non-reference beam, which changes the waist radius at the focus, was also optimized. This implies changing the distance, multiple rounds of optimization as described before, and finally comparing with the output power that was obtained with the previous configuration. From this, we found that the optimum waist size at the focus agrees with the value found by Lo *et al.* [29].

Now the optical power of the IR beams was increased further. Care was taken to avoid abrupt changes of input power, to avoid breaking the crystal due to thermally induced stress. With increased input power, changing the alignment did not improve the conversion efficiency further. However, the optimum temperature changed, as will be further discussed in section 5.3.

5.3 SFG Results

After set-up and optimization as described in subsection 5.2.3, the cooling/detection SFG stage was characterized. The output power was measured as a function of input power product and temperature. The respective results are presented in subsections 5.3.1 and 5.3.2. The Raman SFG beamline was optimized to similar efficiencies, but was not characterized in detail.

5.3.1 Efficiency

Figure 5.6 shows the 626 nm output power of the cooling/detection SFG stage as function of input power product $P_{1050} \times P_{1550}$ as red triangles. For this data, the conversion efficiency calculated according to equation (5.16) is shown as blue circles. The fact that the efficiency drops with input power product can be attributed to the effect of absorption-induced heating, which locally changes the mode in the crystal away from its optimal shape [29, 68]. For this beamline, the aim was to produce at least 1.5 W 626 nm power with an input power product of $3\ \mathrm{W} \times 5\ \mathrm{W} = 15\ \mathrm{W}^2$. This was achieved, and with the laser amplifiers delivering up to $10\ \mathrm{W} \times 10\ \mathrm{W} = 100\ \mathrm{W}^2$, there is enough leeway for possibly increased power demand in the future. The efficiencies are similar to the values found by Lo *et al.*, which range from 3.5 to 3.1 $\%\mathrm{W}^{-1}\mathrm{cm}^{-1}$ for input powers from 1 to 15 W^2. This means that this setup achieves efficiencies as good as the best published result in literature. However, as will be discussed in subsection 5.3.2, the setup was later re-optimized

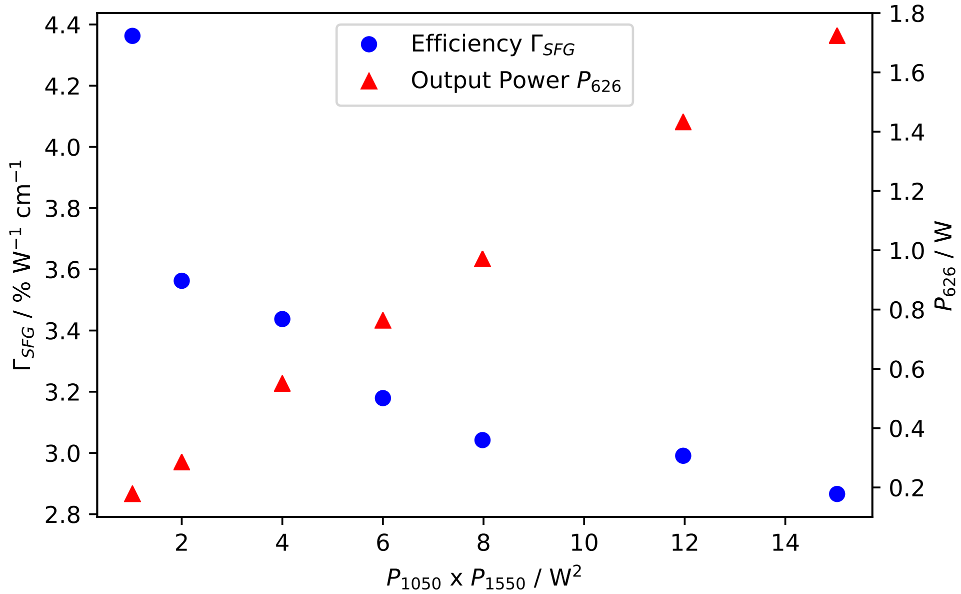

Figure 5.6: Red triangles: 626 nm output power of the cooling/detection SFG stage, as function of input power product. No realigning was performed after changing the input power, but the crystal temperature was reoptimized. The found optimum temperatures are plotted in figure 5.7. Blue circles: conversion efficiency calculated according to equation (5.16). The efficiencies are as good as the values obtained by Lo *et. al.*

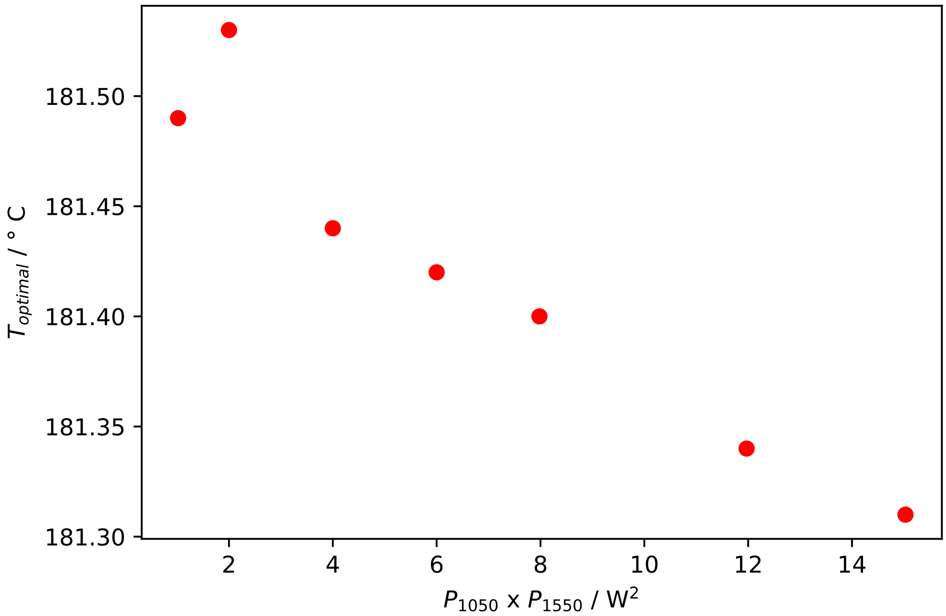

Figure 5.7: Experimentally found optimum crystal temperatures for the same input powers as the data in figure 5.6. The outlier at $P_{1050} \times P_{1550} = 2\ \mathrm{W}^2$ might be due to insufficient thermal equilibration during the measurement process.

for improved beam shape, which reduced the conversion efficiency. Also, it should be noted that the input powers were measured only with limited accuracy. The procedure for this was the following: With a power sensor in front of the crystal, the HWP before the initial PBS was set to yield a number of desired powers at the sensor, and the corresponding HWP angles were noted down. The power sensor was only removed when the incident power was turned low enough to not induce too much thermally induced stress onto the crystal when subjecting it to the laser beams abruptly. Then, the HWP was again set to the angles of the respective input powers to take the measurements.

For every data point, the alignment was not changed. However, the temperature was adjusted, whose optimum values are plotted in figure 5.7. The dependence of conversion efficiency on crystal temperature is discussed in the following subsection.

5.3.2 Optimum temperature

Figure 5.7 shows the optimum crystal temperature for the input powers as plotted in figure 5.6. The overall trend is that the optimum temperature decreases with input power product, which can be explained by the bulk crystal temperature needing to balance absorption-induced heating by increased input power. Only the data point at $P_{1050} \times P_{1550} = 2\ \mathrm{W}^2$ deviates from this trend, which might be due to a complex interplay of alignment, quasi-phase-matching and absorption-induced heating. Then again, insufficient thermal equilibration during the measurement process is a simpler explanation.

So far, the beamline has always been optimized with regards to output power. However, the alignment which maximizes output power does not necessarily optimize the output beam shape.

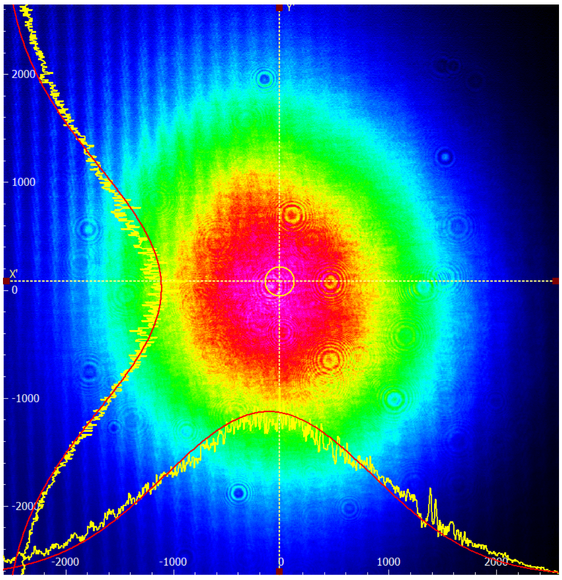

Figure 5.8: Beam profile of the cooling/detection 626 nm output after optimization for output beam shape.

Tobias Sägesser performed realignment while simultaneously monitoring the beam shape on a beam profiler. Optimization by eye towards an approximately Gaussian shape yielded a beam profile as shown in figure 5.8. Whilst doing so, the output power decreased from previously 180 mW at $P_{1050} \times P_{1550} = 1$ W^2 to 130 mW for the same input power. However, this step is necessary since the 626 nm light will have to be coupled into an optical fiber for transport to the 626 $\rightarrow$ 313 nm doubling cavities, and the loss through inefficient fiber coupling caused by a non-Gaussian beam shape presumably is higher than the decrease in power by realignment.

For the realigned beam, the dependence of 626 nm output power on crystal temperature for $P_{1050} \times P_{1550} = 1$ W^2 input power is plotted in figure 5.9. No realignment was performed in between different data points. The orange curve is a fit according to the model $P_{626} = A\,\mathrm{sinc}^2\left(w(T - T_0)\right) + B$ to represent the factor $\mathrm{sinc}^2\left(\frac{\Delta k L}{2}\right)$ (equation (5.14)) introduced in subsection 5.1.2. The constant B was included to account for spurious SFG conversion even when quasi-phase-matching predicts zero output power. The reason for this effect might be imperfect alignment, which relaxes the strict analytical result. We find that the full width at half maximum (FWHM) of the fitted curve is 1.01 °C. The fit matches the experimental data well, except for the side lobes on the lower temperature side, which are much weaker and appear for lower temperatures in the experimental data, which has been observed before [69]. The reason for this might be a change of alignment with crystal temperature, which does not have to be a symmetric effect. Another reason is the non-trivial dependency of the argument of the sinc^2 function on temperature: $\frac{\partial}{\partial T}(\Delta k L) = L\frac{\partial \Delta k'}{\partial T} + \alpha \Delta k' L$ (equation (5.15)) [64]. As soon as $\frac{\partial \Delta k'}{\partial T}$ varies over the temperature range of interest, $\frac{\Delta k L}{2}$ is not anymore only linearly dependent on temperature, and the fit function does not represent the physical model. Also, we did not measure the exact wavelengths of the input and output beams, from which $\Delta k'$ can be inferred. Knowing α, $\Delta k'$ and L, the fit result would allow to calculate an estimate for $\frac{\partial \Delta k'}{\partial T}$.

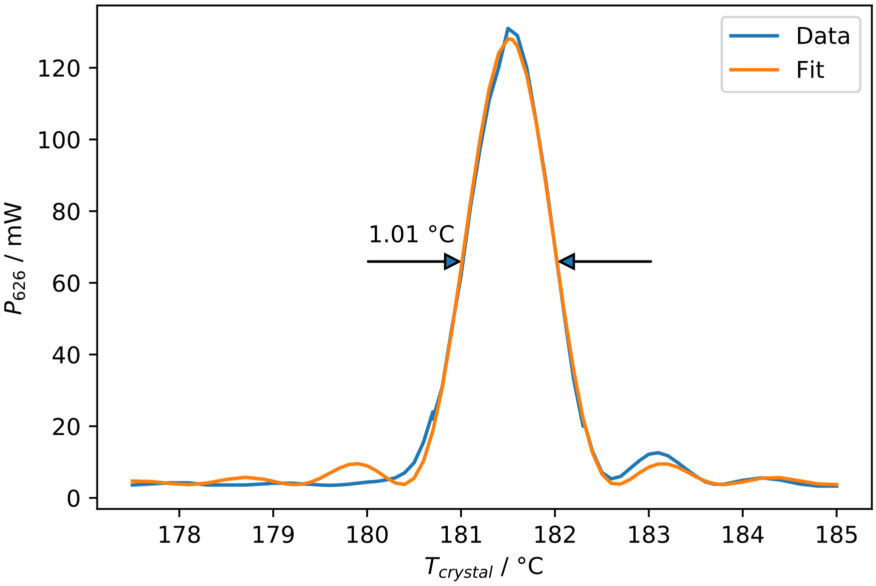

Figure 5.9: 626 nm output power of the cooling/detection SFG stage as function of crystal temperature. No realignment was performed after changing the crystal temperature, the input power was $P_{1050} \times P_{1550} = 1\ \mathrm{W}^2$. The resulting curve roughly agrees with the sinc^2 shape predicted by equation (5.14). The asymmetry might be due to slight misalignment caused by thermal expansion.

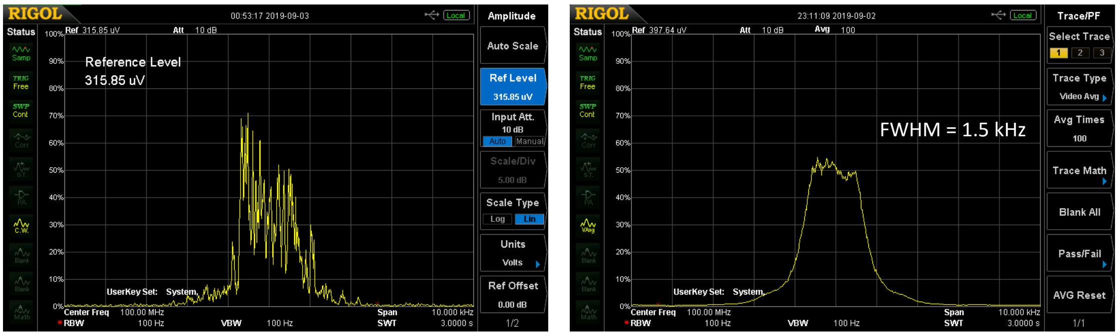

(a) (b)

Figure 5.10: Beat note central peak between both lasers in the locked state observed at 626 nm. The span is 10 kHz. (a) Single sweep. (b) Average over 100 sweeps. Whilst taking the measurement, the beat note central peak observed at 1550 nm looked similar to figure 4.8.

5.4 Observing beat note at 626 nm

Using both SFG beamlines that have been set up, the influence of the SFG stages on the beat note between both Raman seed lasers in the locked state can be observed. Since the two SFG stages are not the two Raman stages next to each other (cf. figure 2.2), the light of the 1050 nm Raman seed laser has been split up to be input to both 1050 nm amplifiers. The two locked 1550 nm seed lasers have been connected such that they provide the input for the two 1550 nm amplifiers which are part of the built SFG stages. Then, the 626 nm light from both SFG stages was overlapped with a non-polarizing beam splitter and focused onto a photodiode (Thorlabs PDA10A-EC). The lock was set to a gain in between the values for figures 4.7a and 4.7b, and the beat note center peak in the locked state at 1550 nm was similar to figure 4.8. While in this state, the beat note center observed at 626 nm is presented in figure 5.10. Note that the shown span is 10 kHz. (a) shows the signal for a single sweep, which exhibits many sharp peaks corresponding to fast fluctuations. (b) shows the same signal, but averaged over 100 sweeps. There, the sharp peaks average out and the lineshape is more defined. The signal resembles a Lorentzian peak which is truncated at about half its maximum. Saturation as reason for this truncation was ruled out, since the single sweep signal includes higher voltage spikes, and also the reduction of optical power incident to the photodiode did not change the lineshape. The FWHM of this peak is 1.5 kHz, corresponding to $\sim$100 times broadening compared to the beat note at 1550 nm. Various reasons might be the cause for this broadening and the fast fluctuations. The most prominent is vibrations of the table on which the optical setup is placed because it is not vibration isolated yet. These vibrations lead to path length fluctuations, which manifest themselves as phase noise. This specific setup is especially prone to this source of error, since the two SFG beamlines are located at opposite ends of the optical breadboard. Acoustic noise from nearby fans might enter through a similar effect. Also the optical fibers connecting the seed lasers to the amplifiers are close to the amplifier fans. A last note is that the laboratory where the setup was located during the measurement is not temperature-stabilized. However, the time-scale of the fast fluctuations seems to fast to be attributed to temperature fluctuations, since the time for one sweep was only 3 seconds.

This measurement will be repeated with the setup in the final laboratory, where it is on a vibration isolated table, with less acoustic noise around and in a temperature-stabilized environment. Also, the relevant measurement would be to test the influence of the two Raman SFG stages, which will be located right next to each other instead of being on other ends of the optical breadboard. If the beat note signal then still exhibits similar fluctuations and broadening, a scheme for feedback at 626 nm might have to be devised.

Chapter 6

Conclusions and Outlook

6.1 Conclusions

The laser setup for a Penning trap experiment with $^{9}Be^{+}$ ions requires two Raman laser beams separated by $\sim$100 GHz, which are phase-stable with respect to each other. Deriving both from the same source is challenging so instead, two separate sources are used and stabilized with respect to each other. As first part of this work, the frequency stabilization of two seed lasers for Raman beams was implemented with an optical phase-locked loop. The loop was modeled in terms of control theory and its limits were identified, leading to optimization by addition of high-frequency phase lead and minimization of signal propagation delay. The loop is highly phase-stable with a beat note HWHM of 9 Hz. The maximum loop bandwidths were found to be about 2.1 MHz with fiber-optical connections, and up to 2.7 MHz with a free space test setup. Shortened optical fiber components are ordered and are expected to yield an intermediate result.

Since all relevant transitions of the Beryllium ion are at 313 nm and especially the Raman beams are required to carry high power, the laser setup uses IR equipment from the telecommunications industry and nonlinear optical processes to generate UV light. Sum-frequency generation of 1050 nm and 1550 nm light creates a stream of photons at 626 nm, which is subsequently converted to 313 nm by cavity-enhanced second-harmonic generation. As second part of this work, two beamlines for sum-frequency generation were set up and optimized. One of them was characterized in terms of conversion efficiency depending on input power and crystal temperature. The efficiencies of 4.4-2.9 $\%\mathrm{W}^{-1}\mathrm{cm}^{-1}$ were found to be consistent with previously published results [29]. Finally, the beat note from two phase-locked seed lasers as in the first part of this thesis was observed at 626 nm after propagation through the two sum-frequency generation beamlines. The spectrum exhibits vastly increased phase-noise, which is mainly attributed to the uncontrolled environment of the temporary laboratory.

6.2 Outlook

The next immediate steps after this work will be to set up the two remaining SFG stages in a similar fashion. Also, a 235 nm laser system for ionization of the neutral Beryllium atoms will be installed. For the already existing SFG stages, the cavity-enhanced second-harmonic generation stages yielding 313 nm light can be installed as well. The repumping and cooling/detection beams will be frequency-stabilized to an absolute reference, such as a cavity via the Pound-Drever-Hall locking scheme [36]. Locking to a transition of molecular iodine [70] seems unfeasible due to fact that the magnetic field has shifted the $^9Be^+$ transition lines away from strong enough iodine transitions at 626 nm.

As mentioned in section 5.4, the stability of the phase lock for the Raman lasers after SFG will be measured again in the final laboratory environment. Depending on the outcome, an additional or alternative locking scheme might be necessary. This could include feedback based on the beat note detection at 626 nm, having the advantage that phase fluctuations introduced over the course of the SFG stage would be counteracted. If the feedback is still applied to the seed laser, the signal propagation delay until detection would greatly increase, leading to a decrease in loop bandwidth. On the other hand, feedback onto an AOM in the beam path at 626 nm decreases the delay. EOMs would most likely not be suitable due to their limited power handling capability. However, an additional component in the beam path would introduce additional loss, so that loop bandwidth and losses would have to be balanced against each other.

Also, the influence of the servo bumps in the experiment will have to be examined at a later point. This can be done by changing the main gain of the control filter, which shifts the position and strength of the servo bumps, while maintaining proper calibration of the power in the central peak. Then, the state fidelities after quantum operations involving Raman transitions can be compared and evaluated. If no satisfying gain setting can be found, the loop bandwidth and thus the frequency from central peak to servo bump can be increased with a double-loop OPLL configuration as mentioned in subsubsection 2.3.2.1. Maybe even a complete alternative like optical injection locking might be necessary.

In general, after the full experimental apparatus of the Penning experiment including the superconducting magnet, cryogenic vacuum chamber, surface trap, Beryllium oven, light delivery, imaging and control system has been set up, the work on loading the first ions can begin. Once a single one is reliably and stably trapped, the trap can be characterized in various aspects. There, one important experiment that stands out is to measure the ion heating rate, not only at a single position but at varying height above the trap surface. This might give further insight into the anomalous heating rate [22, 23], since Paul traps inherently do not allow trapping and thus heating rate measurements without strong RF fields.

The next goal after this is to trap two ions in separate potential wells. Here, the fundamental difference to Paul trap experiments is that the ions are chained along the radial direction. This then paves the way for larger 2D arrays of microscopic Penning traps, each trapping single ions. The ions might be arranged in variable lattices, allowing to study spin-spin interactions with quantum simulations [26]. However the ultimate vision would be to combine the ability to trap $^{40}Ca^+$ ions in a 2D array with single-ion addressing via integrated optics [71, 72] to realize scalable quantum computing.

Bibliography

[1] P.W. Shor. Algorithms for quantum computation: discrete logarithms and factoring. In *Proceedings 35th Annual Symposium on Foundations of Computer Science*, pages 124–134. IEEE Comput. Soc. Press, 2002. ISBN 0-8186-6580-7. doi: 10.1109/sfcs.1994.365700.

[2] Lov K. Grover. Quantum mechanics helps in searching for a needle in a haystack. *Physical Review Letters*, 79(2):325–328, 7 1997. ISSN 10797114. doi: 10.1103/PhysRevLett.79.325.

[3] Richard Feynman. Simulating Physics with Quantum Computers. *International Journal of Theoretical Physics*, 21(6/7):467–488, 1982.

[4] Seth Lloyd. Universal quantum simulators. *Science*, 273(5278):1073–1078, 1996. ISSN 00368075. doi: 10.1126/science.273.5278.1073.

[5] Alexandre Blais, Ren Shou Huang, Andreas Wallraff, S M Girvin, and R J Schoelkopf. Cavity quantum electrodynamics for superconducting electrical circuits: An architecture for quantum computation. *Physical Review A - Atomic, Molecular, and Optical Physics*, 69 (6), 2004. ISSN 10502947. doi: 10.1103/PhysRevA.69.062320.

[6] J. I. Cirac and P. Zoller. Quantum computations with cold trapped ions. *Physical Review Letters*, 74(20):4091–4094, 1995. ISSN 00319007. doi: 10.1103/PhysRevLett.74.4091.

[7] Klaus Mølmer and Anders Sørensen. Multiparticle entanglement of hot trapped ions. *Physical Review Letters*, 82(9):1835–1838, 1999. ISSN 10797114. doi: 10.1103/PhysRevLett.82.1835.

[8] D. Hanneke, J. P. Home, J. D. Jost, J. M. Amini, D. Leibfried, and D. J. Wineland. Realization of a programmable two-qubit quantumprocessor. *Nature Physics*, 6(1):13–16, 2010. ISSN 17452481. doi: 10.1038/nphys1453. URL `http://dx.doi.org/10.1038/nphys1453`.

[9] J. P. Gaebler, T. R. Tan, Y. Lin, Y. Wan, R. Bowler, A. C. Keith, S. Glancy, K. Coakley, E. Knill, D. Leibfried, and D. J. Wineland. High-Fidelity Universal Gate Set for Be 9 + Ion Qubits. *Physical Review Letters*, 117(6):060505, 8 2016. ISSN 10797114. doi: 10.1103/PhysRevLett.117.060505.

[10] Peter W. Shor. Scheme for reducing decoherence in quantum computer memory. *Physical Review A*, 52(4):R2493–R2496, 10 1995. ISSN 10502947. doi: 10.1103/PhysRevA.52.R2493.

[11] Austin G. Fowler, Matteo Mariantoni, John M. Martinis, and Andrew N. Cleland. Surface codes: Towards practical large-scale quantum computation. *Physical Review A - Atomic, Molecular, and Optical Physics*, 86(3):032324, 9 2012. ISSN 10502947. doi: 10.1103/PhysRevA.86.032324.

[12] J. Zhang, G. Pagano, P. W. Hess, A. Kyprianidis, P. Becker, H. Kaplan, A. V. Gorshkov, Z. X. Gong, and C. Monroe. Observation of a many-body dynamical phase transition with a 53-qubit quantum simulator. *Nature*, 551(7682):601–604, 11 2017. ISSN 14764687. doi: 10.1038/nature24654.

[13] V. Negnevitsky, M. Marinelli, K. K. Mehta, H. Y. Lo, C. Flühmann, and J. P. Home. Repeated multi-qubit readout and feedback with a mixed-species trapped-ion register. *Nature*, 563(7732):527–531, 2018. ISSN 14764687. doi: 10.1038/s41586-018-0668-z.

[14] Daniel Gottesman, Alexei Kitaev, and John Preskill. Encoding a qubit in an oscillator. *Physical Review A. Atomic, Molecular, and Optical Physics*, 64(1):123101–1231021, 2001. ISSN 10502947. doi: 10.1103/PhysRevA.64.012310.

[15] C. Flühmann, T. L. Nguyen, M. Marinelli, V. Negnevitsky, K. Mehta, and J. P. Home. Encoding a qubit in a trapped-ion mechanical oscillator. *Nature*, 566(7745):513–517, 2019. ISSN 14764687. doi: 10.1038/s41586-019-0960-6. URL `http://dx.doi.org/10.1038/s41586-019-0960-6`.

[16] C Monroe and J Kim. Scaling the ion trap quantum processor. *Science*, 339(6124):1164–1169, 3 2013. ISSN 10959203. doi: 10.1126/science.1231298.

[17] Robert Weinstock. On a fallacious proof of Earnshaw's theorem. *American Journal of Physics*, 44(4):392–393, 4 1976. ISSN 0002-9505. doi: 10.1119/1.10449.

[18] Wolfgang Paul and Helmut Steinwedel. Ein neues Massenspektrometer ohne Magnetfeld. *Zeitschrift fur Naturforschung - Section A Journal of Physical Sciences*, 8(7):448–450, 1953. ISSN 18657109. doi: 10.1515/zna-1953-0710.

[19] D. J. Berkeland, J. D. Miller, J. C. Bergquist, W. M. Itano, and D. J. Wineland. Minimization of ion micromotion in a Paul trap. *Journal of Applied Physics*, 83(10):5025–5033, 5 1998. ISSN 00218979. doi: 10.1063/1.367318.

[20] S. Seidelin, J. Chiaverini, R. Reichle, J. J. Bollinger, D. Leibfried, J. Britton, J. H. Wesenberg, R. B. Blakestad, R. J. Epstein, D. B. Hume, W. M. Itano, J. D. Jost, C. Langer, R. Ozeri, N. Shiga, and D. J. Wineland. Microfabricated surface-electrode ion trap for scalable quantum information processing. *Physical Review Letters*, 96(25):253003, 6 2006. ISSN 00319007. doi: 10.1103/PhysRevLett.96.253003.

[21] D. Kielpinski, C. Monroe, and D. J. Wineland. Architecture for a large-scale ion-trap quantum computer. *Nature*, 417(6890):709–711, 6 2002. ISSN 00280836. doi: 10.1038/nature00784.

[22] Q. A. Turchette, Kielpinski, B. E. King, D. Leibfried, D. M. Meekhof, C. J. Myatt, M. A. Rowe, C. A. Sackett, C. S. Wood, W. M. Itano, C. Monroe, and D. J. Wineland. Heating of trapped ions from the quantum ground state. *Physical Review A - Atomic, Molecular, and Optical Physics*, 61(6):8, 5 2000. ISSN 10941622. doi: 10.1103/PhysRevA.61.063418.

[23] L. Deslauriers, S. Olmschenk, D. Stick, W. K. Hensinger, J. Sterk, and C. Monroe. Scaling and suppression of anomalous heating in ion traps. *Physical Review Letters*, 97(10):103007, 9 2006. ISSN 00319007. doi: 10.1103/PhysRevLett.97.103007.

[24] H. G. Dehmelt. Radiofrequency Spectroscopy of Stored Ions I: Storage. *Advances in Atomic, Molecular and Optical Physics*, 3(C):53–72, 1968. ISSN 1049250X. doi: 10.1016/S0065-2199(08)60170-0.

[25] Joseph W. Britton, Brian C. Sawyer, Adam C. Keith, C. C Joseph Wang, James K. Freericks, Hermann Uys, Michael J. Biercuk, and John J. Bollinger. Engineered two-dimensional Ising interactions in a trapped-ion quantum simulator with hundreds of spins. *Nature*, 484(7395): 489–492, 4 2012. ISSN 00280836. doi: 10.1038/nature10981.

[26] Shreyans Jain. *Micro-Fabricated Penning Trap Arrays for Quantum Simulation*. PhD thesis, ETH Zürich, 2018. URL `https://www.ethz.ch/content/dam/ethz/special-interest/phys/quantum-electronics/tiqi-dam/documents/masters_theses/masterthesis-Jain-Shreyans`.

[27] Shreyans Jain, Joseba Alonso, Matt Grau, and Jonathan P. Home. Quantum simulation with ions in micro-fabricated Penning traps, 2018. URL `http://arxiv.org/abs/1812.06755`.

[28] A. C. Wilson, C. Ospelkaus, A. P. Van Devender, J. A. Mlynek, K. R. Brown, D. Leibfried, and D. J. Wineland. A 750-mW, continuous-wave, solid-state laser source at 313 nm for cooling and manipulating trapped 9Be+ ions. *Applied Physics B: Lasers and Optics*, 105 (4):741–748, 2011. ISSN 09462171. doi: 10.1007/s00340-011-4771-1.

[29] Hsiang-Yu Lo, Joseba Alonso, Daniel Kienzler, Benjamin C. Keitch, Ludwig E. De Clercq, Vlad Negnevitsky, and Jonathan P. Home. All-solid-state continuous-wave laser systems for ionization, cooling and quantum state manipulation of beryllium ions. *Applied Physics B: Lasers and Optics*, 114(1-2):17–25, 1 2014. ISSN 09462171. doi: 10.1007/s00340-013-5605-0.

[30] D. J. Wineland, C. Monroe, W. M. Itano, D. Leibfried, B. E. King, and D. M. Meekhof. Experimental issues in coherent quantum-state manipulation of trapped atomic ions. *Journal of Research of the National Institute of Standards and Technology*, 103(3):259–328, 1997. URL `http://arxiv.org/abs/quant-ph/9710025`.

[31] Katarzyna Balakier, Lalitha Ponnampalam, Martyn J Fice, Cyril C Renaud, and Alwyn J Seeds. Integrated Semiconductor Laser Optical Phase Lock Loops. *IEEE Journal of Selected Topics in Quantum Electronics*, 24(1), 2018. ISSN 21910359. doi: 10.1109/JSTQE.2017.2711581.

[32] Michael J. Biercuk, U. Y S Hermann, Aaron P. Vandevender, Nobuyasu Shiga, Wayne M. Itano, and John J. Bollinger. High-fidelity quantum control using ion crystals in a penning trap. *Quantum Information and Computation*, 9(11-12):0920–0949, 2009. ISSN 15337146.

[33] C. Langer, R. Ozeri, J. D. Jost, J. Chiaverini, B. Demarco, A. Ben-Kish, R. B. Blakestad, J. Britton, D. B. Hume, W. M. Itano, D. Leibfried, R. Reichle, T. Rosenband, T. Schaetz, P. O. Schmidt, and D. J. Wineland. Long-lived qubit memory using atomic ions. *Physical Review Letters*, 95(6):2–5, 2005. ISSN 00319007. doi: 10.1103/PhysRevLett.95.060502.

[34] H. Ball, M. W. Lee, S. D. Gensemer, and M. J. Biercuk. A high-power 626 nm diode laser system for Beryllium ion trapping. *Review of Scientific Instruments*, 84(6):063107, 6 2013. ISSN 00346748. doi: 10.1063/1.4811093.

[35] S. Vasilyev, A. Nevsky, I. Ernsting, M. Hansen, J. Shen, and S. Schiller. Compact all-solid-state continuous-wave single-frequency UV source with frequency stabilization for laser cooling of Be+ ions. *Applied Physics B: Lasers and Optics*, 103(1):27–33, 4 2011. ISSN 09462171. doi: 10.1007/s00340-011-4435-1.

[36] R. W.P. Drever, J. L. Hall, F. V. Kowalski, J. Hough, G. M. Ford, A. J. Munley, and H. Ward. Laser phase and frequency stabilization using an optical resonator. *Applied*

Physics B Photophysics and Laser Chemistry, 31(2):97–105, 1983. ISSN 14320649. doi: 10.1007/BF00702605.

[37] J. E. Thomas, P. R. Hemmer, S. Ezekiel, C. C. Leiby, R. H. Picard, and C. R. Willis. Observation of Ramsey fringes using a stimulated, resonance Raman transition in a sodium atomic beam. *Physical Review Letters*, 48(13):867–870, 3 1982. ISSN 00319007. doi: 10.1103/PhysRevLett.48.867.

[38] Katarzyna Balakier, Martyn J. Fice, Frederic van Dijk, Gael Kervella, Guillermo Carpintero, Alwyn J. Seeds, and Cyril C. Renaud. Optical injection locking of monolithically integrated photonic source for generation of high purity signals above 100 GHz. *Optics Express*, 22 (24):29404, 12 2014. ISSN 1094-4087. doi: 10.1364/oe.22.029404.

[39] Annie Cuyt, Vigdis Brevik Petersen, Brigitte Verdonk, Haakon Waadeland, and William B Jones. Bessel functions. In *Handbook of Continued Fractions for Special Functions*, pages 343–369. Springer, 2008.

[40] IXblue Photonics. MPX and MPZ series Low frequencies to 40 GHz Phase Modulators, 2019. URL `https://www.qubig.com/products/fiber-modulators/modulators/mpx-z.html`.

[41] V. Ferrero and S. Camatel. Optical Phase Locking techniques: an overview and a novel method based on Single Side Sub-Carrier modulation. *Optics Express*, 16(2):818, 2008. doi: 10.1364/oe.16.000818.

[42] Naresh Satyan and Amnon Yariv. *Optoelectronic Control of the Phase and Frequency of Semiconductor Lasers*. PhD thesis, California Institute of Technology, 2011.

[43] Martyn J. Fice, Andrea Chiuchiarelli, Ernesto Ciaramella, and Alwyn J. Seeds. Homodyne coherent optical receiver using an optical injection phase-lock loop. *Journal of Lightwave Technology*, 29(8):1152–1164, 4 2011. ISSN 07338724. doi: 10.1109/JLT.2011.2115993.

[44] George A. Baker and P. R. Graves-Morris. *Padé approximants*. Cambridge University Press, second edition, 1996. ISBN 0521450071.

[45] K. J. Åström. Limitations on control system performance. *European Journal of Control*, 6 (1):2–20, 2000. ISSN 09473580. doi: 10.1016/S0947-3580(00)70906-X.

[46] John Bechhoefer. Kramers–Kronig, Bode, and the meaning of zero. *American Journal of Physics*, 79(10):1053–1059, 2011. ISSN 0002-9505. doi: 10.1119/1.3614039.

[47] R Wynands, T Mukai, and T. W. Hänsch. Coherent bisection of optical frequency intervals as large as 530 THz. *Optics Letters*, 17(24):1749, 1992. ISSN 0146-9592. doi: 10.1364/ol.17.001749.

[48] Karl Johan Åström and Richard M. Murray. *Feedback Systems An Introduction for Scientists and Engineers*. Princeton University Press, 2009. ISBN 9780691135762. URL `http://www.cds.caltech.edu/~murray/books/AM05/pdf/am08-complete_22Feb09.pdf`.

[49] Karl Johan Åström. Control System Design, 2002. URL `http://www.cds.caltech.edu/~murray/courses/cds101/fa02/caltech/astrom.html`.

[50] Bahaa E. A. Saleh and Malvin Carl Teich. *Fundamentals of Photonics*. John Wiley & Sons, New York, 3 edition, 2019.

[51] Travis C Briles, Dylan C Yost, Arman Cingöz, Jun Ye, and Thomas R Schibli. Simple piezoelectric-actuated mirror with 180 kHz servo bandwidth. *Optics Express*, 18(10):9739, 2010. doi: 10.1364/oe.18.009739.

[52] Amnon Yariv. Dynamic analysis of the semiconductor laser as a current-controlled oscillator in the optical phased-lock loop: applications. *Optics Letters*, 30(17):2191, 2005. ISSN 0146-9592. doi: 10.1364/ol.30.002191.

[53] M.C. Carvalho and A.J. Seeds. Simple model for frequency modulation characteristics of semiconductor lasers. *Electronics Letters*, 24(7):428, 2007. ISSN 00135194. doi: 10.1049/el:19880290.

[54] S. Saito, O. Nilsson, and Y. Yamamoto. Coherent Fsk Transmitter Using a Negative Feedback Stabilised Semiconductor Laser. *Electronics Letters*, 20(17):703–704, 1984.

[55] G. Soundra Pandian and S. Dilwali. On the Thermal FM Response of a Semiconductor Laser Diode. *IEEE Photonics Technology Letters*, 4(2):130–133, 2 1992. ISSN 19410174. doi: 10.1109/68.122338.

[56] Pascal Correc, Olivier Girard, and Ildefonso F. de Faria. On the Thermal Contribution to the FM Response of DFB Lasers: Theory and Experiment. *IEEE Journal of Quantum Electronics*, 30(11):2485–2490, 1994.

[57] Jesse B. Hoagg and Dennis S. Bernstein. Nonminimum-Phase Zeros. *IEEE Control Systems*, 27(3):45–57, 2007. ISSN 1066033X. doi: 10.1109/MCS.2007.365003.

[58] M. A. Grant, W. C. Michie, and M. J. Fletcher. The Performance of Optical Phase-Locked Loops in the Presence of Nonnegligible Loop Propagation Delay. *Journal of Lightwave Technology*, 5(4):592–597, 1987. ISSN 15582213. doi: 10.1109/JLT.1987.1075532.

[59] Toptica. FALC 110 mFALC 110 Fast Analog Linewidth Control Manual, 2017.

[60] Serge Haroche and Jean-Michel Raimond. *Exploring the Quantum: Atoms, Cavities, and Photons*. Oxford University Press, 2013. ISBN 9780199680313.

[61] Jonathan P. Home. Effect of servo bumps on sideband transitions, 2019.

[62] Claude Cohen-Tannoudji, Jacques Dupont-Roc, Gilbert Grynberg, and T. A. Brian Kennedy. *Atom–Photon Interactions: Basic Processes and Applications*. WILEY-VCH Verlag GmbH & Co. KGaA, Weinheim, 2004. ISBN 9780471293361.

[63] Keysight Technologies. Spectrum and Signal Analyzer Measurements and Noise, 2017. URL `https://literature.cdn.keysight.com/litweb/pdf/5966-4008E.pdf`.

[64] Martin M. Fejer, Dieter H. Jundt, Robert L. Byer, and G. A. Magel. Quasi-Phase-Matched Second Harmonic Generation: Tuning and Tolerances. *IEEE Journal of Quantum Electronics*, 28(11):2631–2654, 1992. ISSN 15581713. doi: 10.1109/3.161322.

[65] G. D. Boyd and D. A. Kleinman. Parametric interaction of focused Gaussian light beams. *Journal of Applied Physics*, 39(8):3597–3639, 1968. ISSN 00218979. doi: 10.1063/1.1656831.

[66] M Schwarz, O O Versolato, A Windberger, F R Brunner, T Ballance, S N Eberle, J Ullrich, P O Schmidt, A K Hansen, A D Gingell, M Drewsen, and J. R.Crespo López-Urrutia. Cryogenic linear Paul trap for cold highly charged ion experiments, 2012. ISSN 00346748.

[67] Yasuzi Suzaki and Atsushi Tachibana. Measurement of the μm sized radius of Gaussian laser beam using the scanning knife-edge. *Applied Optics*, 14(12):2809, 1975. ISSN 0003-6935. doi: 10.1364/ao.14.002809.

[68] R.G. Batchko, G.D. Miller, A. Alexandrovski, M.M. Fejer, and R.L. Byer. Limitations of high-power visible wavelength periodically poled lithium niobate devices due to green-induced infrared absorption and thermal lensing. In *Technical Digest. Summaries of Papers Presented at the Conference on Lasers and Electro-Optics. Conference Edition. 1998 Technical Digest Series, Vol.6 (IEEE Cat. No.98CH36178)*, pages 75–76. IEEE, 1998. doi: 10.1109/cleo.1998.675885.

[69] S Chaitanya Kumar, G K Samanta, and M Ebrahim-Zadeh. High-power, single-frequency, continuous-wave second-harmonic-generation of ytterbium fiber laser in PPKTP and MgO:sPPLT. *Optics Express*, 17(16):1561–1563, 2009.

[70] J J Snyder, R K Raj, D Bloch, and M Ducloy. High-sensitivity nonlinear spectroscopy using a frequency-offset pump. *Optics Letters*, 5(4):163, 4 1980. ISSN 0146-9592. doi: 10.1364/OL.5.000163.

[71] K. K. Mehta, A. M. Eltony, C. D. Bruzewicz, I. L. Chuang, R. J. Ram, J. M. Sage, and J. Chiaverini. Ion traps fabricated in a CMOS foundry. *Applied Physics Letters*, 105(4): 044103, 7 2014. ISSN 00036951. doi: 10.1063/1.4892061.

[72] Karan K. Mehta, Colin D. Bruzewicz, Robert Mcconnell, Rajeev J. Ram, Jeremy M. Sage, and John Chiaverini. Integrated optical addressing of an ion qubit. *Nature Nanotechnology*, 11(12):1066–1070, 12 2016. ISSN 17483395. doi: 10.1038/nnano.2016.139.